UNIVERSITÀ DEGLI STUDI
DI GENOVA

ISTITUTO ITALIANO
DI TECNOLOGIA

Local image correlation methods for the characterization of subcellular structure and dynamics by confocal and super-resolution microscopy

Candidate: ***Scipioni Lorenzo***

Advisors: ***Lanzanò Luca, Diaspro Alberto***

Abstract

This thesis work aspires to present a new concept for the application of correlation techniques to the study of the cellular environment. By exploiting local analysis in combination to a fast fit-free technique (the phasor approach) we provide an exhaustive high-resolution analysis of structural and dynamic properties while maintaining a reasonable computation time. The dissertation will be articulated as follows:

In **CHAPTER 1** we aim to provide the reader with a description of the techniques that will be exploited during the rest of the dissertation together with the open questions and problematics that our techniques will try to answer to.

In **CHAPTER 2** we present the local analysis concept and its application to a correlation technique capable of measuring size and concentration (ICS). We will show how we coupled ICS to the phasor approach to create a technique (PLICS) for the assessment of size heterogeneity. PLICS will be demonstrated with simulations as well as with cellular samples and will be applied to the study of endocytic vesicles uptake and to the characterization of other organelles.

In **CHAPTER 3** the concept is extended to two-colors samples for the determination of local inter-structure distance (PLICCS). We will present a pattern analysis method we developed that exploits this information in order to evaluate the relative distribution of the structures imaged in the two channels, comparing it to a random distribution. This method will be validated with simulations and applied to the study of replication-transcription collisions. Successively, we will show that PLICCS can be converted to a localization algorithm for single particle tracking that will be used for tracking membrane receptors in living neurons.

CHAPTER 4 will describe the extension of our local analysis to RICS, a correlation technique capable of measuring the diffusion coefficient of a fluorescent probe. The resulting algorithm (L-RICS) provides high resolution diffusion maps that will be used to characterize the diffusion of a fluorescent probe (GFP) within the nucleus and nucleolus of living cells. We will show that the algorithm can be implemented also in non-linear scanning systems.

CHAPTER 5 will conclude the dissertation by introducing advanced correlation methods for the analysis of non-Brownian diffusion and their coupling to super-resolution techniques. In particular, we will present a super-resolution correlation technique (SPLIT) recently developed capable of analyzing the cellular environment and a microcamera-based approach (Airyscan comprehensive correlation analysis) we developed for the parallel implementation, in super-resolution, of several complementary correlation techniques.

CHAPTER 1 Introduction

Investigation of the structure and mobility of sub-cellular structures is complicated by the heterogeneity of their spatial and dynamic properties. For instance, the size of structures within the cell can range from as small as a fraction of nanometers for a single base pair up to tens of microns of the entire cell (1), while the timescale of cellular processes can span from the micro-seconds up to several weeks (2), as shown in ***Figure 1 A***.

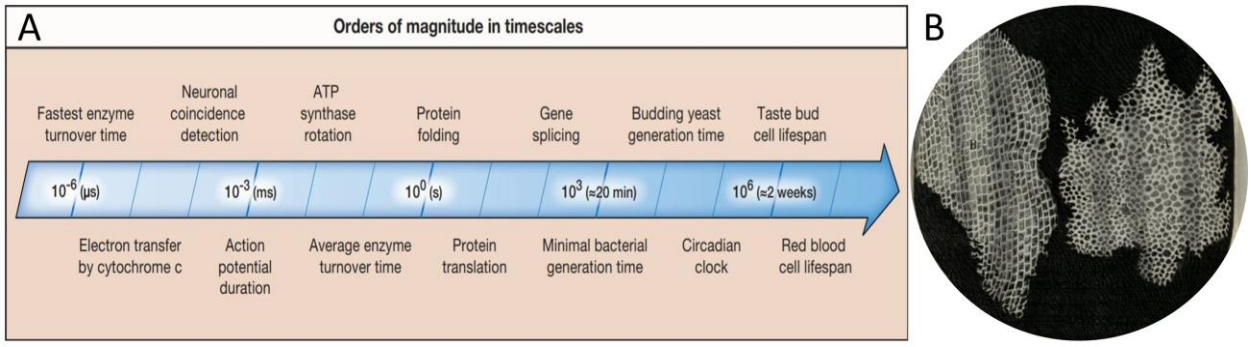

Figure 1: (A) Typical timescale of several cellular processes, reproduced from (2), and drawing of magnified cork slice (B) from Micrographia (Robert Hooke, 1665)

Microscopy has been the first technique that allowed for the direct visualization of the cell itself and ultimately lead to its definition by the term “cell”, introduced for the first time by Robert Hooke in 1665 in its book “Micrographia” (***Figure 1 B***) and it’s always been of invaluable help in the determination of cellular structures and properties.

Historically, optical microscopy has been mainly limited to transmission microscopy until the development of the first fluorescence microscopes in the early 1900s. Fluorescence emission has been exploited since then to develop a series of structure-specific markers in order to visualize only the structures of interest against a dark background, allowing for high-contrast and high-specificity images of subcellular organelles and proteins.

Fluorescence is the process by which of a molecule can absorb light at a certain wavelength and successively emits light at a longer wavelength, passing through a series of non-stable energy states. Once the photon is absorbed, many processes can

occur before the (potential) emission and, in order to more clearly visualize the extension of these processes, the *Jablonski diagram*, shown in ***Figure 2*** reproduced from (3), is often exploited.

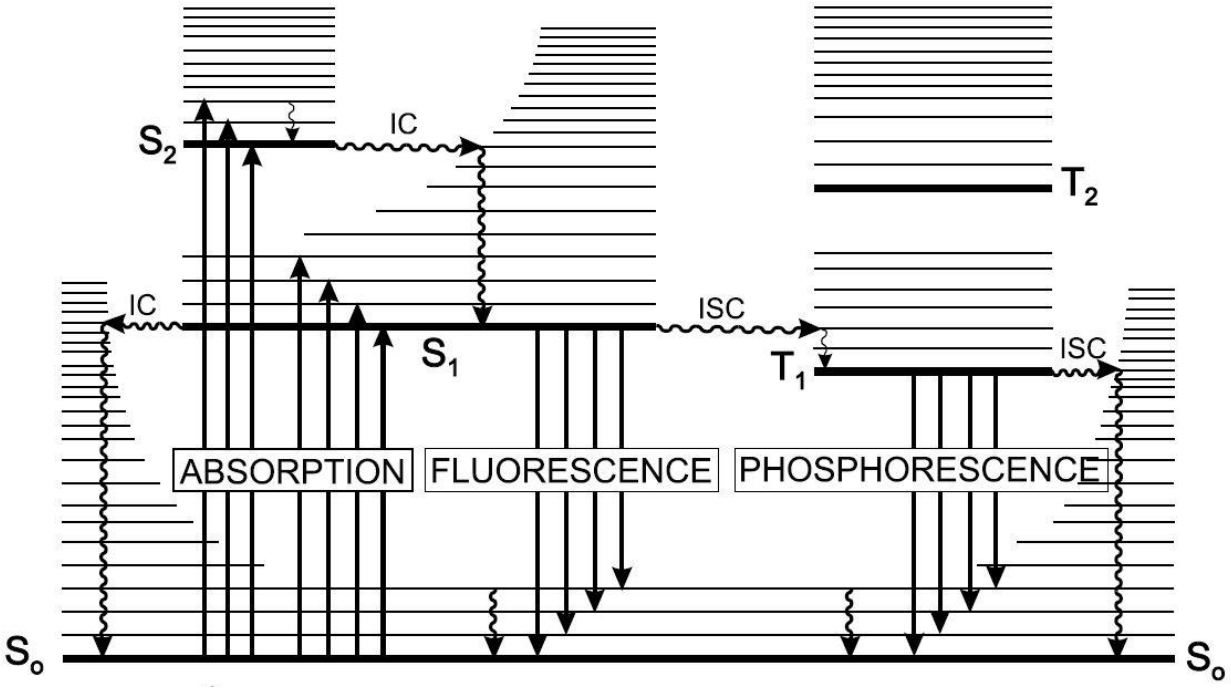

Figure 2: Jablonski diagram showing several possible transitions: Absorption, fluorescence, phosphorescence, internal conversion (IC) and inter-system crossing (ISC)

On the y-axis of the diagram is represented the energy of the state, once a photon is absorbed (absorption) the system experiences an energy jump to a higher-energy state (upward arrows) typically from the singlet ground state ($\boldsymbol{S_0}$) to a singlet excited state ($\boldsymbol{S_1}$ or $\boldsymbol{S_2}$). The length of the arrows is equal to the energy of the absorbed photon, inversely proportional to its wavelength. In the diagram, the bold lines represent *electronic states*, which correspond to different electronic charge distribution states of the molecule, each of which has a series of other lines corresponding to several *vibrational states*, relative to the same electronic state. It's worth mentioning that the transitions between vibrational states are typically non-radiative processes (meaning they don't result in the emission of a photon) as opposed to the transition between electronic states, which is also slower ($t_{vibrational}$~$10^{-12} - 10^{-10}\ s$, $t_{electronic}$~$10^{-10} - 10^{-7}\ s$). This is also the reason why the fluorescence emission usually occurs at a longer wavelength: let's

assume the system is in the vibrational ground state of $\boldsymbol{S_0}$ and can transition to any excited vibrational state of, for instance, $\boldsymbol{S_1}$, then it will lose energy in vibrational relaxations until it reaches the ground state of $\boldsymbol{S_1}$, where it will fluoresce to any vibrational state of $\boldsymbol{S_0}$, experiencing a smaller energy jump and therefore emitting a photon with lower energy and longer wavelength. The difference between the most probable emission wavelength and the most probable absorption wavelength is known as *Stokes shift.*

Other processes worth mentioning are internal conversion (non-radiative transition between electronic singlet levels), inter-system crossing (non-radiative transition between an electronic singlet level and an electronic triplet level) and the triplet relaxation $\boldsymbol{T_1 \rightarrow S_0}$, which is a radiative transition with characteristic time typically longer than the fluorescence ($t_{\boldsymbol{T_1 \rightarrow S_0}} \sim 10^{-6} - 10^{0}\ s$). From this description, only two processes result in the emission of photons: *Fluorescence* (electronic relaxation of singlet states) and *phosphorescence* (electronic relaxation of triplet states).

Every transition has a certain probability of occurring which is higher the more the wave-functions of the two levels are similar, resulting in a series of absorption probability peaks (corresponding to the wavelength of the photons that allow a transition to an excited state) and emission peaks (corresponding to the wavelength of the possible emission wavelengths) that, ultimately, are the absorption and emission spectra, respectively. When dealing with fluorophores for biological applications, we usually encounter continuous spectra instead of peaked ones, this is due to the fact the these fluorophores are characterized and used at room temperature, so the peaks are broader and appear as a continuous distribution.

The probability of a process to occur can be quantitated by its rate constant:

k_r^S: rate constant for the $\boldsymbol{S_1 \rightarrow S_0}$ radiative relaxation (fluorescence emission)

k_{IC}^S: rate constant for the $\boldsymbol{S_1 \rightarrow S_0}$ internal conversion (non-radiative)

k_{ISC}: rate constant for inter-system crossing (non-radiative)

since both intersystem crossing and internal conversion are non-radiative processes, we can consider a single rate constant $k_{nr}^S = k_{ISC} + k_{IC}^S$ for the non-radiative relaxation

from the singlet excited state $\boldsymbol{S_1}$. Once excited, a molecule can de-excite through several pathways, and the rate of de-excitation is described by the following equation:

$$-\frac{d[A^*]}{dt} = \left(k_r^S + k_{nr}^S\right)[A^*] \qquad \textit{Eq. 1}$$

where $[A^*]$ indicates the concentration of molecules in the excited state. Let $[A^*]_0$ be the concentration of molecules in the excited state at the time 0, integrating the equation leads to $[A^*] = [A^*]_0 e^{-\frac{t}{\tau_S}}$ where

$$\tau_S = \frac{1}{k_r^S + k_{nr}^S} \qquad \textit{Eq. 2}$$

is the *lifetime* of the excited state $\boldsymbol{S_1}$. Since some molecules are de-excited with radiative processes and others with non-radiative ones, it's useful to define the *fluorescence quantum yield*:

$$\Phi_F = \frac{k_r^S}{k_r^S + k_{nr}^S} = k_r^S \tau_S \qquad \textit{Eq. 3}$$

which represents the fraction of excited molecules returning to the ground state $\boldsymbol{S_0}$ with the emission of fluorescence photons.

Although the specificity of fluorescence labeling can be very high, allowing for the visualization of structures impossible to visualize by transmission microscopy, there are other factors that can degrade the image quality and therefore hinder the visualization of certain structures. For instance, since the fluorescence signal comes from all the fluorophores contained in the cell or tissue to be imaged, but only one plane is in focus, the light coming from out-of-focus planes adds up and creates a blurred background, inferring the quality of the microscopy image. Confocal microscopy was developed for overcoming this limitation and provide an optical sectioning effect in the sample.

Confocal microscopy consists in illuminating the sample in a single point with a laser beam and using a pinhole in the detection path in order to reject the out-of-focus light

(***Figure 3 A***). Then the beam is scanned throughout the area of the specimen and reconstructed in order to obtain the final image.

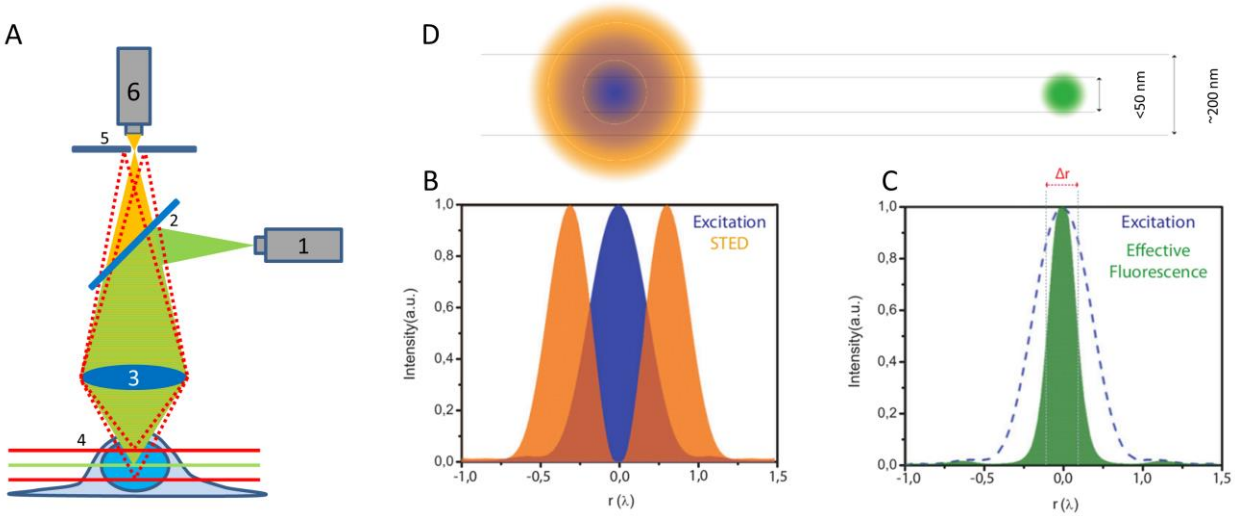

Figure 3: (A) Schematic representation of a confocal microscope. Green light coming from the laser (1) goes to a dichroic mirror (2) which reflects it through the objective lens (3) to the specimen (4), the fluorescence light (orange) goes back following the same path but this time passes through the dichroic and goes to the detector (6) passing through the pinhole (5). Note the light coming from the in-focus plane (4, green) goes right through the pinhole, while the light coming from out-of-focus planes (4, red lines and red dotted paths) is blocked. Graph (B) illustrating the overlap of the intensity of the STED donut shaped spot ISTED (r) (orange) and excitation spot (blue) in one dimension. (C) Graph illustrating the decrease in the width of the effective fluorescence probability h(r) (green) as a result of STED. Δr is the FWHM of the effective fluorescence probability. Overlapping a doughnut-shaped STED spot (D) with diffraction limited excitation spot will result in a confinement of the area in which fluorophores are able to fluoresce. B,C and D are reproduced from svi.nl/STEDMicroscopy

The minimum extension of the illumination spot can be calculated and it is due to diffraction effects that do not allow the light to be packed more tightly than the so called *diffraction limit*, quantified by Abbe in 1875:

$$\boldsymbol{d = \frac{\lambda}{2 \cdot NA} = \frac{\lambda}{2 \cdot n \sin \theta}} \qquad \textbf{Eq. 4}$$

Here, d is the minimum distance at which two structures can be for being resolved, λ is the wavelength of the light used for the measurement and NA is the *numerical aperture*, equal to the refractive index of the immersion medium (n) times the sinus of the semi-

angle of aperture (θ), namely half of the angle at which the light coming from the sample is collected by the objective.

The spatial distribution of light in the diffraction-limited spot is usually parameterized as a 3D Gaussian function with x-y full width at half maximum (FWHM) equal to the Abbe resolution limit while the FWHM along z is usually set to 3 times the extension in x-y. The diffraction-limited spot of illumination is referred to as Point Spread Function (PSF) of the microscope, and the resulting microscopy image is the result of the convolution of the actual fluorophore distribution (the "real" image) with the PSF.

Typically, a high NA objective can have a numerical aperture around 1.5 and therefore, together with a 488 nm light source, results in a resolution of ~160 nm, which means that two structures closer than this distance cannot be resolved and will appear as a single structure. Since many cellular structures have a spatial extension below this spatial range, several methods, called *super-resolution methods*, were recently developed for overcoming the diffraction barrier and were granted a Nobel Prize in Chemistry in 2014. Super-resolution techniques are many and diverse, but can be roughly divided in three principal categories: single molecule localization microscopy (SMLM), structured illumination techniques and RESOLFT (REversible Saturable Optical Linear Fluorescence Transitions) like techniques. In the following, we will limit to the description of the STED (STimulated Emission Depletion) approach, a super-resolution technique based on the stimulated emission effect (4-7) which is part of the RESOLFT techniques family. Briefly, stimulated emission is an effect occurring when a system in the excited state (e.g. the vibrational ground state of $\boldsymbol{S_1}$ in ***Figure 2***) interacts with a photon with energy corresponding to the energy jump to a lower energy level (e.g. any of the vibrational states $\boldsymbol{S_0}$); in that case, there is a certain probability that the system de-excites to the energy level corresponding to the energy jump and emits two photons of equal energy.

This effect is exploited in the STED technique by superimposing to the excitation laser a doughnut-shaped depletion laser beam at a longer wavelength (***Figure 3 B***), the fluorophores lying closer to the depletion doughnut have a higher probability of undergoing stimulated emission than fluorescence emission so, since the stimulated

emission photon have the same wavelength of the depletion beam, which is filtered in detection, the ultimate effect is a decrease of the spatial extension of the PSF, resulting in super-resolution (***Figure 3 C,D***). Ultimately, the resolution limit achieved by STED is quantified as

$$d_{STED} = \frac{\lambda}{2 \cdot NA} \frac{1}{\sqrt{1+\frac{I}{I_{sat}}}} \qquad \textit{Eq. 5}$$

where I is the intensity of the stimulated emission laser and I_{sat} is the *saturation intensity*, or the intensity at which the resolution is improved by a factor $\sqrt{2}$. The value of the saturation intensity depends on the wavelength of the stimulated emission laser and on the fluorescent probe photo-physics, underlining the importance of fluorescent probes in super-resolution microscopy.

Structural imaging is important, but it gives information about a single moment in time, while it can be of interest investigating the dynamics of a certain processes, for instance the diffusion of a certain protein in the cellular environment. Since diffusing proteins move continuously, imaging will result in a diffuse signal that may not be informative about the actual diffusion of the protein and consequently a whole series of techniques has been developed in order to assess protein diffusion, for instance Fluorescence Recovery After Photobleaching or FRAP (8-10) and Fluorescence Correlation Spectroscopy or FCS. In the following we will introduce only the FCS approach as a tool for the investigation of the dynamics of fluorescent or fluorescently-labeled species (11-16), for instance proteins in the cellular environment. The experimental setup for FCS is the same as in confocal microscopy (***Figure 3 A***) but the beam is not scanned and the fluorescence intensity as a function of time $F(t)$ is recorded for a fixed position. The fluctuations in the fluorescence signal are due to the fluorescent species diffusing in and out the PSF (***Figure 4 A***) of the microscope and, by computing the auto-correlation function (ACF, ***Figure 4 C***) of the signal, we can obtain a curve the width of which it is linked to the average residence time of the species inside the illumination volume.

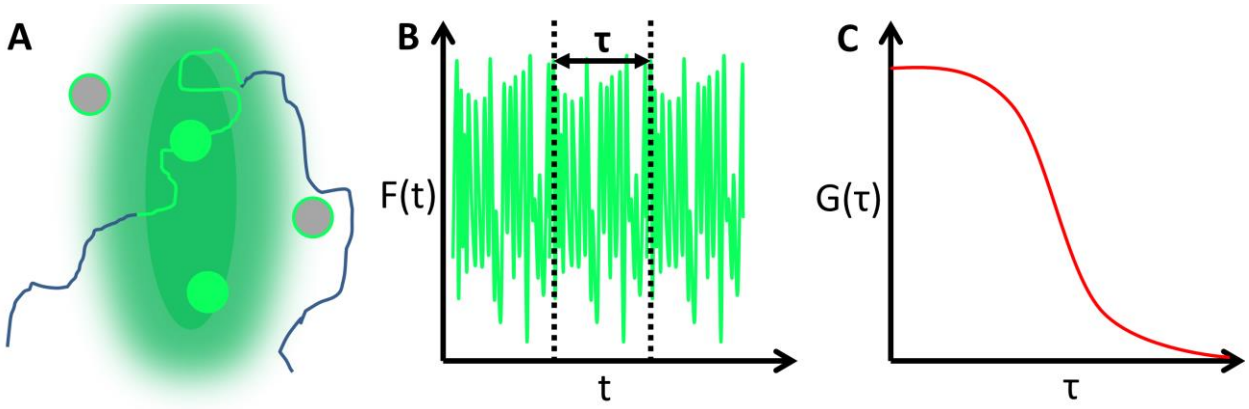

Figure 4: FCS setup, molecules are diffusing in and out of the illumination spot (A), giving a fluctuating signal $\boldsymbol{F(t)}$ as a function of time (B). The signal is auto-correlated to obtain the ACF $G(\tau)$ (C)

ACF is computed as

$$\boldsymbol{G(\tau) = \frac{\langle \delta F(t) \cdot \delta F(t+\tau) \rangle}{\langle F(t) \rangle^2} = \frac{\langle F(t) \cdot F(t+\tau) \rangle}{\langle F(t) \rangle^2} - 1} \qquad \textbf{Eq. 6}$$

where $\delta F(t) = F(t) - \langle F(t) \rangle$, where brackets denote temporal averaging. $G(\tau)$ can be fitted to several theoretical models describing different diffusion behavior. For the sake of simplicity, in the following we will only consider free (Brownian) diffusion, described by

$$\boldsymbol{G(\tau) = \frac{\gamma}{N}\left(1 + \frac{\tau}{\tau_D}\right)^{-1}\left(1 + \frac{\tau}{K^2\tau_D}\right)^{-1/2} + G_\infty} \qquad \textbf{Eq. 7}$$

where $K = \frac{z_0}{w_0}$ is the ratio between the longitudinal (z_0) and the axial (w_0) extension of the PSF, N is the average number of molecules, γ is a shape factor related to the intensity distribution of the detection volume (e.g. $\gamma = 0.3535$ for a Gaussian PSF) and G_∞ is the limiting factor for $\tau \to \infty$ (usually equal to 0). The *diffusion time* or *correlation time* τ_D can be linked to the diffusion coefficient D by

$$\boldsymbol{\tau_D = \frac{w_0^2}{4D}} \qquad \textbf{Eq. 8}$$

It's worth mentioning that $G(0) = \frac{\gamma}{N}$ if $G_\infty = 0$, therefore the height of the ACF is inversely proportional to the average number of particles in the illumination volume. This is due to the fact that

$$\boldsymbol{G(0) = \frac{\langle \delta F(t) \rangle^2}{\langle F(t) \rangle^2} = \frac{\langle (F(t) - \langle F(t) \rangle)^2 \rangle}{\langle F(t) \rangle^2}} \qquad \textbf{Eq. 9}$$

where the numerator is the variance of the signal which, assuming a Poissonian distribution, is proportional to the average number of molecules, while the average intensity squared at the denominator is proportional to the average number of molecules squared, resulting in

$$\boldsymbol{G(0) = \frac{\langle (F(t) - \langle F(t) \rangle)^2 \rangle}{\langle F(t) \rangle^2} = \frac{\propto N}{\propto N^2} = \propto \frac{1}{N}} \qquad \textbf{Eq. 10}$$

Ultimately, knowing the spatial extension of the illumination volume, it is possible to obtain an absolute measure of concentration of the fluorescent species. In conclusion, FCS is a powerful tool, for the determination and quantitation of the diffusion modality and the concentration of a fluorescent species diffusing in a medium.

CHAPTER 2 Phasor analysis of Local Image Correlation Spectroscopy (PLICS): Assessment of spatial heterogeneity

2.1 Image Correlation Spectroscopy (ICS)

Introduction

Image correlation spectroscopy (ICS) is the spatial analogue of FCS which has been developed relatively recently (17) for the characterization of fluorophore distribution and molecular aggregation in microscopy images. ICS is widely accepted as a highly versatile method for analyzing biological macromolecule organization with applications ranging from clustering of membrane receptors (18, 19) to the counting of dendritic spines (20), to the characterization of collagen fibers (21, 22) or even cells in epithelial layers (23). Every ICS-based analysis starts with the calculation of the autocorrelation function (ACF) of the image $I(x,y)$, defined as

$$G(\xi,\eta) = < I(x,y)I(x+\xi,y+\eta) > \qquad \textit{Eq. 11}$$

Where the brackets indicate that average is carried out over the entire image. The basic principles of ICS are largely similar to those of FCS with the notable difference that while for FCS the analysis is performed on intensity fluctuations in time, ICS involves the analysis of intensity fluctuations in space (18). In both cases fluctuations are characterized through a normalized autocorrelation function which contains average information about the typical width and relative magnitude of the fluctuations. The width of the spatial autocorrelation function is a parameter that can be used to measure the size of fluorescent elements whereas its amplitude can be used to quantify their concentration. To this aim, a normalized autocorrelation function is usually defined as:

$$G(\xi,\eta) = \frac{<\delta I(x,y)\delta I(x+\xi,y+\eta)>}{<I(x,y)>^2} = \frac{<I(x,y)I(x+\xi,y+\eta)>}{<I(x,y)>^2} - 1 \qquad \textit{Eq. 12}$$

By definition, the correlation function is obtained by average over many fluctuations and thus can be a robust and precise characterization method, even when calculated on very noisy dataset; on the other hand, if some kind of heterogeneity is present in the system, it could be hidden by the averaging process.

The analysis of the ICS autocorrelation function generally goes through a fitting procedure with a Gaussian function:

$$g(\xi,\eta) = g(0,0) \cdot e^{-\frac{\xi^2+\eta^2}{2\sigma^2}} + g_\infty \qquad \textit{Eq. 13}$$

with $g(0,0)$, σ^2 and g_∞ as fitting parameters. As with FCS, $g(0,0)$ is inversely proportional to the number of structures in the volume, while the variance $\sigma^2 = \sigma^2_{particle} + \sigma^2_{PSF}$ comes from the combined contributions of the size of the particle and the instrument PSF. The parameter g_∞ takes into account a not complete decay of the ACF or spurious long-range spatial correlations (e.g. background contribution). If the labeled structures have a sub-resolution size (e.g. small proteins) and can aggregate in sub-resolution clusters, $g(0,0)$ is inversely proportional to the average number of clusters $< n >_c$, from which we can define a cluster density (CD)

$$CD = \frac{<n>_c}{\pi\sigma^2} \qquad \textit{Eq. 14}$$

It's worth mentioning that ICS could, in principle, retrieve also the average number of proteins per cluster, in case no quenching of the fluorophores is present, since fluorophore aggregation within the PSF does not contribute to the variance) but the intensity scales with the number of fluorophores. This parameter is called degree of aggregation (DA) and is defined as

$$DA = \frac{<I(x,y)>}{CD} = c\frac{<n>_m}{<n>_c} \qquad \textit{Eq. 15}$$

where $< n >_m$ denotes the number of monomers and c is a scaling factor which depends on several experimental parameters (molar extinction coefficient and quantum yield of the probe and intensity and wavelength of the laser, for instance) and can be

calibrated by imaging a sample with only monomers with the same experimental parameters.

ICS-based Techniques

A generalization of ICS can be obtained by considering the spatiotemporal correlation function of a signal I_a with a signal I_b:

$$G(\xi,\eta,\tau) = \frac{<\delta I_a(x,y,t)\delta I_b(x+\xi,y+\eta,t+\tau)>}{<I_a(x,y,t)>_t <I_b(x,y,t+\tau)>_{t+\tau}} \qquad \textit{Eq. 16}$$

Where $\delta I(x,y,t)$ denotes fluorescence fluctuations defined as $\delta I(x,y,t) = I(x,y,t) - < I(x,y,t) >_t$. As an example, if $a = b$ and we neglect the time information we obtain the ICS equation described before (***Eq. 12***); exploiting this general formulation, a plethora of other techniques has been developed that measure several biophysical properties and can benefit from a local approach.

- **kICS:** k-space Image Correlation Spectroscopy, consists in time-correlating the Fourier transform of the images in the time series, it's used to obtain information about the dynamics of the probe in the case of blinking probes or photobleaching.
- **TICS:** Temporal Image Correlation Spectroscopy, exploits only temporal correlation in order to obtain number density, dynamics and immobile fraction of diffusing species.
- **STICS:** Spatiotemporal Image Correlation Spectroscopy, exploits both spatial and temporal correlation in order to evaluate direction and magnitude of molecular flow.
- **RICS:** Raster scanning Image Correlation Spectroscopy, relies on the fast scanning speed of confocal microscope in order to obtain information about fast diffusion dynamics, will be discussed more in detail in **CHAPTER 3.**

ICS-based techniques are continuously being developed and improved over the years and, together with technological advances, allow for very precise and reliable measurements of numerous biophysical properties.

Heterogeneity in ICS and local analysis

In many cases, it can be of interest to isolate the different species forming a heterogeneous system and characterize them separately. In general, if the image can be approximated by a superposition of several independent contributions (i.e. there is no correlation between the species):

$$\boldsymbol{I(x,y) = \sum I_k(x,y)} \qquad \textit{Eq. 17}$$

then its correlation function $\hat{G}(\xi,\eta)$ can be described as a combination of the correlation functions $\hat{G}_k(\xi,\eta)$ corresponding to the single species:

$$\boldsymbol{\widehat{G}(\xi,\eta) = \frac{\sum <I_k(x,y)>^2 \left[1+\widehat{G}_k(\xi,\eta)\right]}{<\sum I_k(x,y)>^2} - 1} \qquad \textit{Eq. 18}$$

However, it can be a difficult task to recover, from the total correlation function $\hat{G}(\xi,\eta)$, the relative concentration of each component species and the shapes of the correlation functions $\hat{G}_k(\xi,\eta)$ of each component. In fact, the correlation function of a heterogeneous system must be fit to a model including multiple components, requiring some assumptions on the nature of the sample, for instance the number of components.

If there is spatial heterogeneity, i.e. different parts of the image contain different species, one can attempt to retrieve the correlation functions of multiple species by calculating the correlation functions in small portions of the image. From now on, we will use the term *local* correlation functions, in opposition to the *global* functions calculated over the whole image. The idea behind local ICS is that we get a better description of the heterogeneity of the system by limiting the averaging process to small spatial intervals. On the other hand, for a given image, we generate a huge number of correlation functions (one per pixel, therefore typically 2^{16} for 256x256 images). We will describe a method to characterize all these functions in a simple way.

2.2 Phasor approach

Phasors

The fast analysis of a large number of spectra is an issue common to many other spatially-resolved spectroscopies. A versatile method of analysis that provides an

unbiased, fit-free quantification of spectral properties at each pixel of an image, is the so called phasor approach, originally developed for the identification of components in Fluorescence Lifetime Imaging Microscopy (FLIM)(24) and extensively applied to FLIM detection of FRET (Förster Resonance Energy Transfer) (25-29). The phasor analysis has been extended to spectral fingerprinting (30-32), fluorescence correlation spectroscopy(33) and super-resolution microscopy(34).

The phasor approach consists in transforming a function f(x), sampled over L points, into a complex space where it will be described by two Cartesian coordinates, g and s, defined as:

$$\begin{cases} \boldsymbol{g} = \dfrac{\int_0^L \boldsymbol{f(x)}\, \boldsymbol{cos}\left(\frac{2\pi x}{L}\right) \boldsymbol{dx}}{\int_0^L \boldsymbol{f(x)dx}} \\ \boldsymbol{s} = \dfrac{\int_0^L \boldsymbol{f(x)}\, \boldsymbol{sin}\left(\frac{2\pi x}{L}\right) \boldsymbol{dx}}{\int_0^L \boldsymbol{f(x)dx}} \end{cases} \qquad \textbf{\textit{Eq. 19}}$$

The coordinates (*g*,*s*) can be plotted in a 2D histogram, called the phasor plot. The first implementation of the phasor approach to microscopy is to FLIM; briefly, FLIM in the time domain acquires pixel by pixel the lifetime curve (described as an exponential decay) of the fluorophore recorded in that particular position. The curve is successively fitted in order to compute the decay constant of the exponential, which is the lifetime of the fluorophore, and map it throughout the entire field of view, hence obtaining a lifetime image. In this particular implementation, the challenge is to analyze a great number of functions (typically 256x256 but up to 2048x2048) in a reasonable amount of time, possibly distinguishing between multi-exponential decays and maintaining spatial information.

If $f(x) = Ae^{-\frac{t}{\tau}}$ the coordinates are simply given by

$$\begin{cases} g = \dfrac{1}{1+(\frac{2\pi\tau}{L})^2} \\ s = \dfrac{\frac{2\pi\tau}{L}}{1+(\frac{2\pi\tau}{L})^2} \end{cases} \qquad \textit{Eq. 20}$$

describing a semicircle in the phasor space. Interesting case is the combination of $k = 1 \ldots n$ exponential decays, in which the coordinates become

$$\begin{cases} g = \sum_k \dfrac{f_k}{1+(\frac{2\pi\tau_k}{L})^2} \\ s = \sum_k \dfrac{f_k \frac{2\pi\tau_k}{L}}{1+(\frac{2\pi\tau_k}{L})^2} \end{cases} \qquad \textit{Eq. 21}$$

where f_k is the intensity weighted fractional contribution of the k^{th} decay, meaning that the phasor of combination of, for instance, two exponential decays lies between the phasor of the two pure species. An interesting application of this property is the background contribution: since the phasor of a constant background is (0,0), every combination of a pure exponential with a constant background will shift the resulting phasor toward the origin, but if we describe the phasor in angular coordinates (M,ϕ), this shift will affect only the modulation, leaving the phase unchanged. An example of phasor combination is shown in ***Figure 5***.

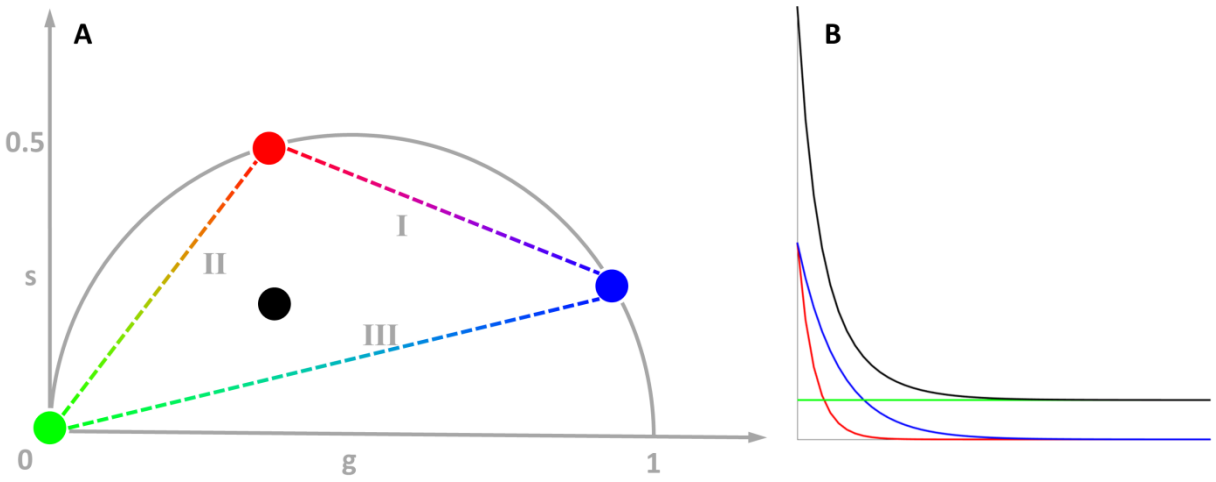

Figure 5: Phasor space (A) representation of different exponential curves shown in (B), a fast decay (red spot, red line), a slower decay (blue spot, blue line) and offset (green dot, green line) and a combination of all these (black spot, black line). Lines denoted with I, II and III show the connection between red and blue, red and green and blue and green, respectively.

Gaussian "fitting" with phasors

The phasor transform per se is a way to perform a frequency analysis on a curve. In the following I'll show how this analysis was used in order to write a fitting algorithm for 1D Gaussian functions. Conventionally, a fitting algorithm goes through a series of optimization processes in order to minimize the difference between an experimental function and a model in order to evaluate the parameters that describe the model. With phasors, we transform both the experimental function and the model function in the phasor space and find the parameters to assign to the model so that the two phasor transforms match.

Using the phasor transform, it's worth noticing that a change of coordinates can result in a dimensionality reduction from four to one parameter. For instance, let's consider a 1D Gaussian model function:

$$g(x) = A \cdot e^{-\frac{(x-c)^2}{2\sigma^2}} + B \qquad \textit{Eq. 22}$$

where A is a scale factor, B is the background, c is the center and σ^2 is the variance. The first step which results in a dimensionality reduction is the computation of the

autocorrelation function; the ACF will be centered in x=0, losing the information about the center c. The resulting function is now in the form

$$\tilde{g}(\xi) = \tilde{A} \cdot e^{-\frac{\xi^2}{4\sigma^2}} + \tilde{B} \qquad \textit{Eq. 23}$$

where the scaling factor and the background are different, as well as the variance which is doubled; note that the coordinate now is ξ which represents the spatial shift. If we apply the phasor transform to $\tilde{g}(\xi)$, due to the normalization factor in ***Eq. 19*** we lose the information on the scaling factor $\tilde{A}$, remaining with only the variance and the background. Since the background is uncorrelated with respect to ξ, its phasor coordinates are (0,0). For the mathematics of the phasors, the combination of every phasor with the background will be on the line connecting the phasor transform of the function without background and (0,0). This means that if we change the coordinates from (g,s),Cartesian, to (M,ϕ),angular, the contribution of the background will affect only the modulus but not the phase. Thus the only dimension left (the variance) can be described by a single parameter, i.e. the phase ϕ.

Finally, by constructing a calibration function $\phi(\sigma^2)$, we can invert it and obtain the variance of a Gaussian from the phase of the transformed function. The calibration function is constructed by simulating Gaussian functions with known parameters and by plotting the phase of their phasor transform as a function of the variance. This procedure is the same whether the Gaussian function we analyze is misplaced, scaled and/or affected by a homogeneous background. The background, for instance, can be evaluated from the modulation, while the scaling factor can be retrieved by analyzing the same function with an additional known background (35). In the following chapters we will show how to obtain also the center of a displaced Gaussian function.

From a computational point of view, all the operations described so far can be implemented with FFT (Fast Fourier Transform) algorithms, resulting in a very high computing speed without the need of iterative procedures.

2.3 Phasor Analysis of Local Image Correlation Spectroscopy (PLICS)

In the following, we will show how we combined local ICS with the phasor approach in order to obtain a fast algorithm for the detection of spatial heterogeneity. We will consider first the case where the particles are well separated, meaning there is maximum one particle per local ROI, and then discuss the application of the method at a higher particle density.

Algorithm

The workflow of the PLICS algorithm is shown schematically in ***Figure 6***. Let us assume we have the image of a heterogeneous sample (i.e. two or more populations of particles with different size), as shown in ***Figure 6 A***.

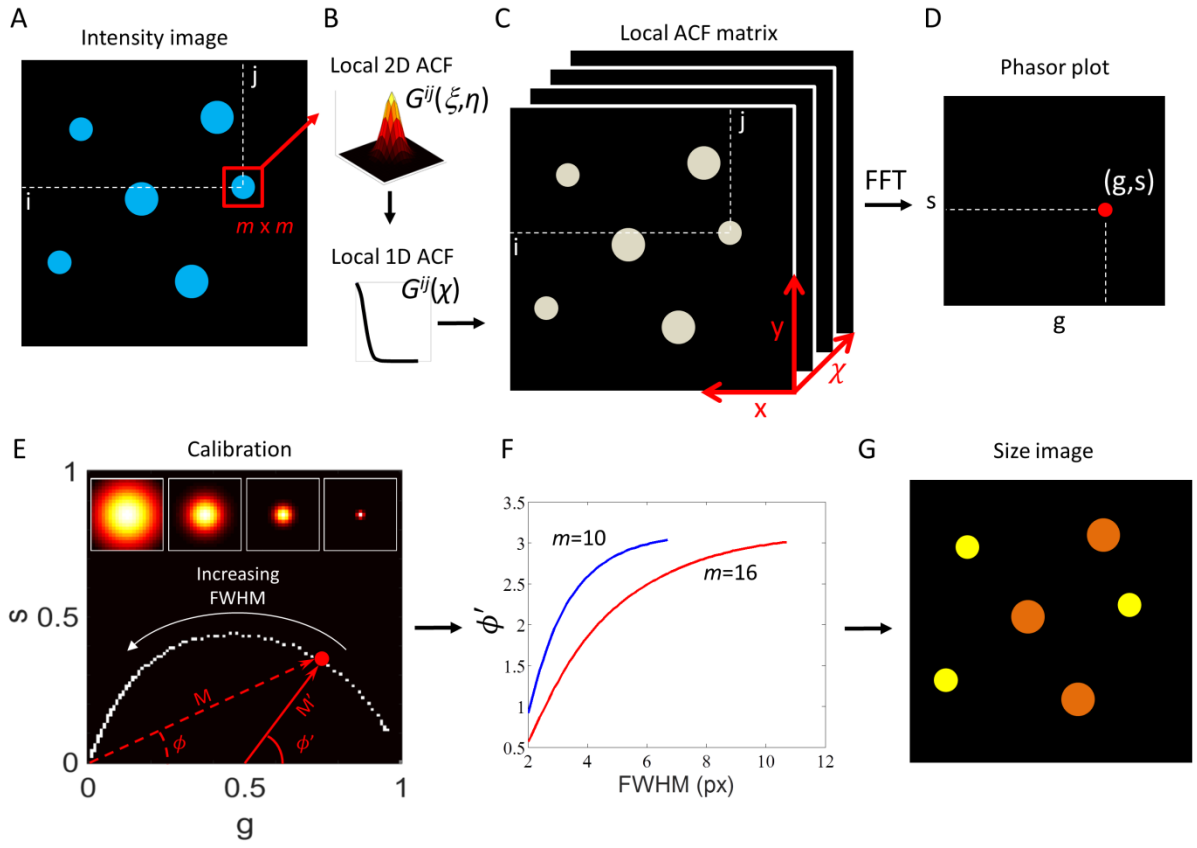

Figure 6: (A-F) Schematic workflow of the PLICS method. A small m×m region around each pixel (i,j) of an intensity image (A) is used to calculate a local 2D spatial correlation function (B, top) and its angular mean (B, bottom), which is stored along the 3rd dimension in the corresponding (i,j) position of the Local ACF Matrix (C). (D) The phasor coordinates (g,s) are obtained by performing a FFT along the 3rd dimension of the Local ACF Matrix in the (i,j) point (C); (E) phasor plot obtained by a collection of calibration structures, whose examples are

shown in the inset, from which mask-specific calibration curves are obtained (F) and used to construct a Size Image (G).

Instead of considering the whole image as in conventional ICS, we use a smaller *m*×*m* mask centered on the pixel (*i*,*j*) and shift it throughout the entire image computing, for each of the *m*×*m* sub-images, its 2D autocorrelation function $G^{ij}(\xi, \eta)$ (local 2D ACF, ***Figure 6 B top***):

$$G^{ij}(\xi,\eta) = < I(x,y)I(x+\xi, y+\eta) >_{ij} \qquad \textit{Eq. 24}$$

When dealing with sparse samples (as it's often the case with microscopy images) the analysis can be limited to pixels above a user-defined intensity threshold; this procedure results in an increase of computing speed.

Each of the local 2D ACFs is computed via a 2D-FFT (Fast Fourier Transform) algorithm. The normalized version of the local 2D ACF $\hat{G}^{ij}(\xi, \eta)$ is calculated by:

$$\hat{G}^{ij}(\xi,\eta) = \frac{<I(x,y)I(x+\xi,y+\eta)>_{(i,j)}}{<I(x,y)>^2_{(i,j)}} - 1 \qquad \textit{Eq. 25}$$

If the local 2D ACFs $G^{ij}(\xi, \eta)$ are circularly symmetric, we convert them into local 1D ACFs $G^{ij}(\chi)$ (***Figure 6 B bottom***). This is done by performing an angular mean on the local 2D ACF function over 60 orientations covering the angle of π radians. In order to increment the sampling of the function for the angular mean, the local 2D ACF is subject to a 5× oversampling (via a Fourier transform interpolation) prior to averaging and then is down-sampled back. If the local 2D ACFs are not symmetric, the 1D analysis can be limited to one or more selected orientations of the 2D ACF. This can be useful in the case of non-spherical organelles (e.g. mitochondria) or when the 2D ACF is expected to be asymmetric(36); the analysis of asymmetric and non-sparse samples will be discussed in **2.5**.

We then construct a 3D matrix (***Figure 6 C***) which stores, in the 3rd dimension, the 1D function $G^{ij}(\chi)$ obtained by analyzing the m×m sub-image centered in the (i,j) pixel. By means of a FFT along the third dimension we obtain, for each pixel of the image, the

two phasor coordinates (g,s). The coordinates (g,s) can be plotted in a 2D histogram, the phasor plot (***Figure 6 D***). The position of the phasor contains unbiased information about the local correlation function $G^{ij}(\chi)$. we can choose the size, m, of the sub-image in such a way that it contains no more than one particle. In this case, the width of the local ACF is directly related to the width of the single particle. A calibration for any given size m x m of the sub-image is performed by generating a series of simulated m x m images of Gaussian spots, centered on the images, using their full width at half-maximum (FWHM) as the reference parameter (***Figure 6 E,F***). To exploit, through a single parameter, the variations in both phase and modulation, we define ϕ' as the phase with respect to the $\mathrm{shifted}$ center of reference of coordinates (1/2,0). The shifted phase, ϕ', is calculated by using the relation: $\tan(\phi') = {}^{s}/_{(g-1/2)}$ (***Figure 6 E,F***). The steepness of the calibration function determines the sensitivity by which a given value of size can be measured, and for values of size $FWHM_{max} > \sim 2/3m$, the sensitivity is poor (***Figure 6 F***). Accordingly, calibration curves were obtained with FWHM values in pixels (px) ranging from 2 to $2/3m$, with steps of 0.1, and interpolating with a hyperbolic tangent function, the parameters of which are stored so that by inversion of the curve, one can obtain the absolute size value. Finally, the value of size is assigned to each pixel, resulting in an image pseudo-colored according to the size of the particles (***Figure 6 G***)

Simulations

In order to test the algorithm and characterize the shape of the local correlation functions, we simulated images in Matlab (The Mathworks). Every image is created by adding a user-defined number of structures (e.g., Gaussian-shaped elements with a certain FWHM), either noise affected or not, in a random position (unless stated otherwise). Poisson noise-affected Gaussian structures were simulated by creating a Gaussian-shaped probability distribution of given FWHM and by randomly adding a number, N, of photons to the image according to this distribution. SNR in this case was quantified as a photon density per element ($SNR = N/FWHM^2$, N being the number of photons per structure).

Effect of a particle at border

When shifting the mask throughout the image, it can happen that a particles are cut by the mask borders; this results in the computation of an ACF from particles which are apparently smaller, therefore yielding an underestimated size as shown in Figure 7. This issue, to which we will refer as “cut effect” can be solved with two approaches:

- *Iterative PLICS,* PLICS analysis can be carried out iteratively by starting with the most intense pixel in the image which, most likely, will correspond to the center of the structure. Once computed, the size is assigned to the pixels surrounding the central one, so that the same size is assigned to pixels within a diameter equal to the FWHM of the structure. This approach results ideal in the case of single structures distributed in the image and will be used throughout the rest of the manuscript.
- *Reassignment,* after applying PLICS in a pixel-wise fashion, the size parameter is reassigned in order to match the size computed in the most intense nearby pixel. This approach, despite being slower than the previous, allows for the freedom of choosing the regions and the extent of reassignment to be applied, resulting ideal for images with inhomogeneous density.

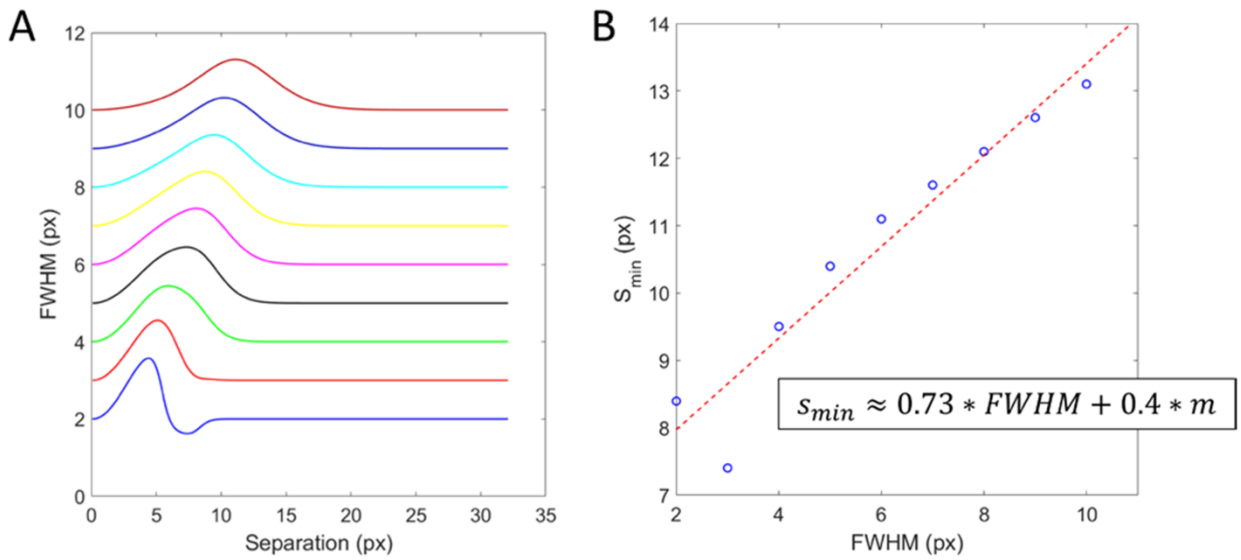

Figure 7: (A) PLICS size as a function of the separation between two particles with FWHM ranging from 2 to 10 px (bottom to top curves), m=16 px. (C) Value of the separation between two particles s_{min} at which the size value deviates by 10% with respect to the correct value, plotted as a function of the FWHM (blue circles). The red dashed line is a linear fit. Shown is an

approximate formula relating s_{min} to FWHM and m, obtained by repeating this analysis for several values of m.

Even if a particle is centered on the mask, the local ACF could be deformed by another particle which is located nearby. From the analysis shown in ***Figure 7*** it is possible to estimate the minimum distance at which two particles must be in order to be considered isolated.

Effect of particle density on the local ACF

The $G^{ij}(\xi, \eta)$ and $\hat{G}^{ij}(\xi, \eta)$ functions are calculated from small *m*×*m* sub-images and, especially when the sub-image contains only one or few particles, the shape of the corresponding $G^{ij}(\chi)$ and $\hat{G}^{ij}(\chi)$ functions are deformed by the presence of particles at the border. For practical purposes, we consider two limiting cases of application of the algorithm:

- *low density limit*, when particles are separated at least by $s_{min.}$ In the low density limit, $G(\chi)$ is employed instead of $\tilde{G}(\chi)$ since $G(\infty) = 0$ while $\tilde{G}(\infty) = -1$ (see ***Figure 8 A***), furthermore, we used a set of angular coordinates (M', ϕ') with the origin shifted in (g,s)=(0.5,0) in order to better distinguish the points close to (0,0), of which we use only the shifted phase parameter ϕ'. With this coordinates, a background removal algorithm (e.g. a median average removal) is required, since ϕ' is not insensitive to background as ϕ.

- *high density limit*, when there are many particles in the sub-image. In this case , $\tilde{G}(\chi)$ is employed instead of $G(\chi)$ since $\tilde{G}(\infty) = 0$ while $G(\infty) = 0$ (see ***Figure 8 A***). In this case, non-shifted angular coordinates (M, ϕ) are used, in particular the phase ϕ is now insensitive to background and will be used for the sizing. For "high density" we consider the range from which the cut effect is negligible, so in the case shown in ***Figure 8 B-C***, the phase value is unchanged after a density of 0.1 particles/pixel^2.

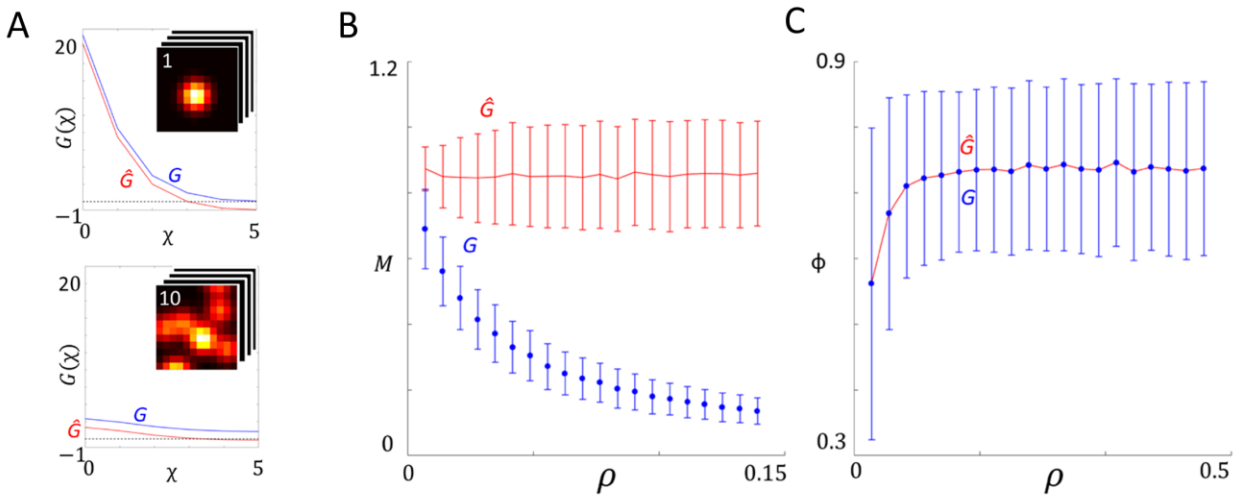

Figure 8: (A) Average local ACF curves for N=1 (top) and N=10 (bottom) particles (FWHM=3px) randomly distributed in a m-by-m area (m=12). The curves of $\hat{G}(\chi)$ (red) and $G(\chi)$ (blue) are obtained from the average of 1000 realizations. Modulation (B) and phase (C) of the local correlation functions $\hat{G}(\chi)$ (red) and $G(\chi)$ (blue) (m=12) for varying particle density ρ (expressed as number of particles per pixel squared). The curves show the mean and standard deviation of 1000 simulations.

PLICS on simulated images

The PLICS workflow described before has been tested on simulated images in order to compare his performances with global ICS analysis. In ***Figure 9*** we compare a polydisperse (***Figure 9 A***) versus a monodisperse (***Figure 9 F***) sample of particles in the low density limit. It's worth recalling that, being a low density sample, we will use the correlation function $G(\chi)$ and not $\tilde{G}(\chi)$

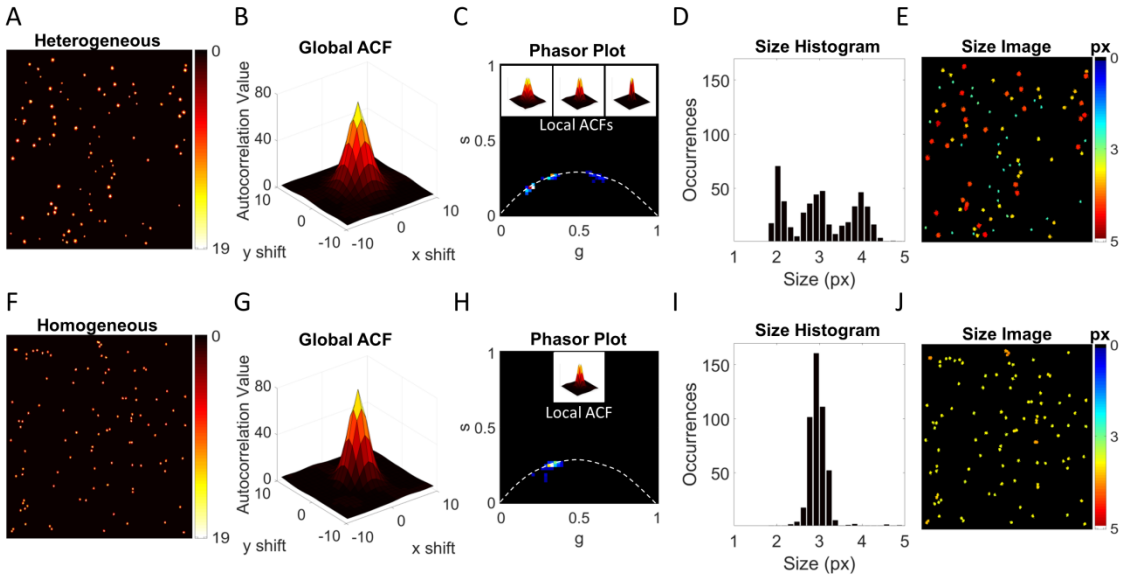

Figure 9: Analysis of polydisperse (A-E) and monodisperse (F-J) randomly distributed Gaussians with SNR=10. The monodisperse sample consists of 100 elements with FWHM=3px, while the polydisperse sample consists of 33 elements with FWHM=2px, 33 with FWHM=3px and 34 with FWHM=4px. (B,G): Global ACFs computed on the intensity images (A,F) respectively. (C,H) Phasor plots of (A,F) compared with m=10 calibration curve (white dashed line), examples of local ACFs are shown in the insets. (D,I) Size histograms obtained from the Size Images (E,J) of (A,F), respectively.

Conventional ICS analysis leads to similar global ACFs (***Figure 9 B,G***) reflecting the average size of particles in the image, as a consequence the recovery of the properties of the single species of the heterogeneous sample from the global ACF can be challenging and generally requires assumptions about the number and/or the brightness of the species. The phasor plot of local ACFs (***Figure 9 C***), instead, provides an immediate and unbiased fingerprint of the heterogeneity of the polydisperse sample, compared to the phasor plot of the monodisperse sample (***Figure 9 H***). In the phasor space (***Figure 9 C,H***), it is possible to discriminate three separate species in the polydisperse sample, whereas only a single species is visible in the monodisperse sample, as expected. In the insets of ***Figure 9 C*** and ***H*** are also reported representative local ACFs corresponding to the single populations: comparing them to the global ACF we can appreciate how much of the single species contribution is hidden in the average. By using the calibration curve it is possible to transform the information encoded in the phasor coordinates into size information, leading to a size histogram (***Figure 9 D,I***) and

a size image (***Figure 9 E,J***). From PLICS analysis we can evaluate the mean size and the standard deviation of each single population and their spatial distribution. Note that, for particles that cannot be considered isolated, the measured size deviates from its correct value (***Figure 9 J***).

A powerful feature of every ICS-based analysis is the measurement of the number of particles in a system, information that, in principle, is lost in the phasor transform. For a system which is heterogeneous in size, it would be of interest to know the number of particles for each separate subspecies. The PLICS approach provides a way to highlight if size heterogeneity is present in the system and to measure, at least in the limit of low density, the characteristic sizes of separate subspecies, which would be otherwise hidden in the average properties of the global ACF (***Figure 10***).

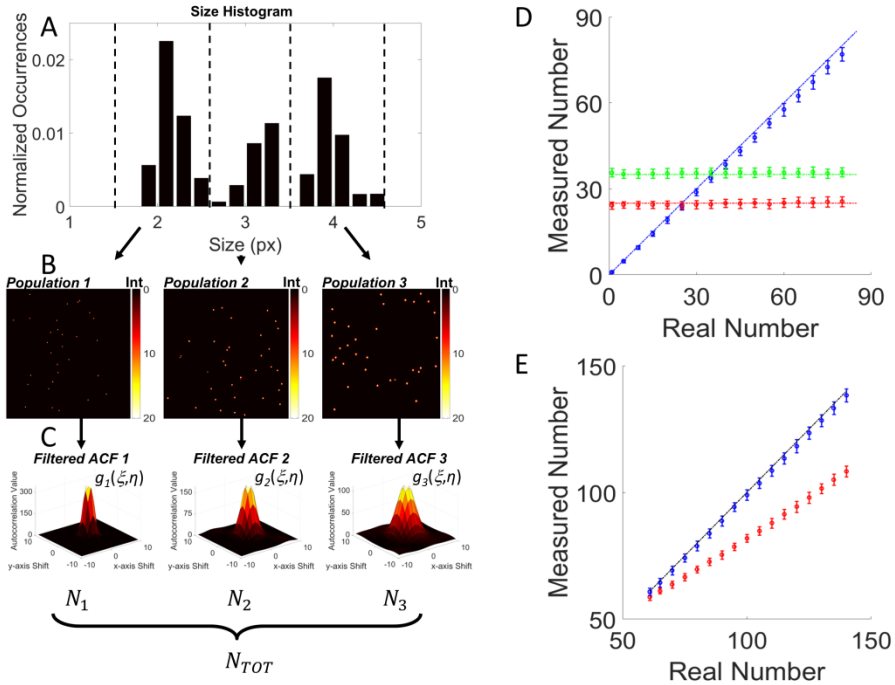

Figure 10: (A) Size histogram of a polydisperse sample of particles, SNR=10, the black dotted lines visually showing the segmentation performed (1.5px<Size$_1$<2.5px, 2.5px<Size$_2$<3.5px, 3.5px<Size$_3$<4.5px) to obtain the segmented images in (B), shown from the smaller (Population 1) to the larger (Population 3). (C) Filtered ACFs corresponding to the segmented populations, from which the number of elements of each population has been retrieved (N_1, N_2, N_3). (D) Retrieved number of a single population (circles) shown as mean value of a set of 100 realization, the error bar being the standard deviation; Population 1,2 and 3 correspond to blue, red and green circles, respectively, and the dash-dotted lines shows the actual number for each population; Populations 2-3 were simulated with constant number (25 and 35, respectively),

while Population 1 number was varied from 1 to 80. (E) Retrieved total number (blue circles) compared with traditional ICS analysis (red circles) of the same samples in (D).

Considering that the size histogram obtained from the PLICS analysis (***Figure 10 A***) can be used to define multiple subspecies and produce a segmentation of the image according to size, with this operation we can obtain three separate images (***Figure 10 B***), each containing only one population of interest. Performing ICS analysis on these images, by using the global correlation function defined in ***Eq. 12***, we calculate the *filtered* global ACFs $\hat{G}_k(\xi,\eta)$ (***Figure 10 C***), the amplitude of which is inversely proportional to the number of elements in each population. Note that here we use the term *filtered* to indicate that the new correlation functions are calculated with the purpose of separating the species of a heterogeneous system (37).

In order to demonstrate that even the number of a small population could be successfully computed by this procedure, we simulated a polydisperse sample with two fixed populations (N_2=25 and N_3=35 elements) and one population with variable number of elements (N_1=1÷80 elements). ***Figure 10 D*** shows the number of elements recovered for each population as a function of N_1, the results of the analysis are consistent with the simulated values with the exception of a small deviation, towards larger values of N_1, due to the fact that we're leaving the low density limit range.

Noteworthy, the total number of elements of the heterogeneous system can be calculated as the sum of the numbers of elements of each subspecies (***Figure 10 C,E***). This analysis provides a better estimation of the total number elements with respect to what can be obtained from a single global ACF, which returns an underestimated number (***Figure 10 E***).

In the limit of high density of particles, the PLICS analysis can be used to visualize the spatial heterogeneity of the correlation functions (***Figure 11***). However, in this case, the differences in the local image correlation functions (***Figure 11 G,K***) should not be interpreted as variations in the size of single particles.

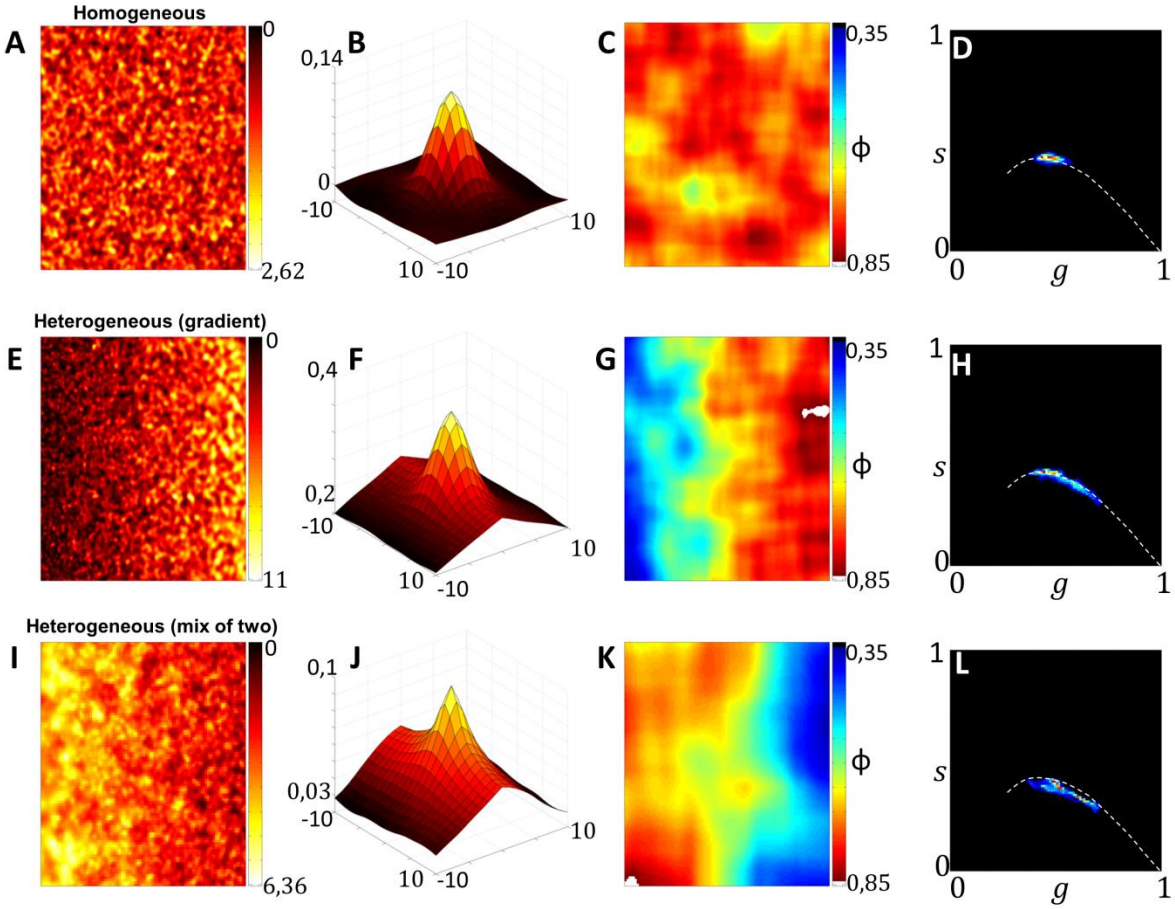

Figure 11: PLICS analysis at high density of monodisperse (A-D) and polydisperse (E-L) particles. The monodisperse sample consists of 10000 particles with FWHM=4px. The polydisperse sample in (E) consists of 10000 elements with FWHM ranging from 2 to 5 px distributed so that their FWHM increases from left to right following a linear gradient. The polydisperse sample in (I) consists of 10'000 elements with FWHM equal to either 2 or 5 px distributed so that the density of structures with FWHM=5px decreases from left to right whereas the density of structures with FWHM=2px increases from left to right. Shown are the intensity images (A,E,I), the global ACFs (B,F,J), the phase images (C,G,K) and the phasor plots (D,H,L). The PLICS analysis is performed with m=16. The dashed white line in the phasor plot is a guide to the eye.

For instance, assume that the FWHM of the particles in the image increases from left to right following a linear gradient (***Figure 11 E***): since each sub-image contains only particles of approximately the same size, the phase map (***Figure 11 G***) indicates that particles of different size are located in different positions of the image. On the other hand, consider now a combination of large and small particles distributed so that the ratio between small and large particles increases from left to right (***Figure 11 I***): since

each sub-image may contain particles of different size, the phase map (***Figure 11 K***) indicates only that the average size changes according to location but provides no hint on the fact that the sample is a combination of two pure species. Nevertheless, a comparison between the phasor plots (***Figure 11 H,L***) shows that the local ACF of the sample which is a mix of two sizes follows a different trajectory with respect to the sample which has a gradient of size, in agreement with the rules of phasors (23). This suggests that a discrimination between the two cases is possible.

2.4 PLICS for the characterization of intracellular vesicles

In the following, we will validate the use the PLICS algorithm for the analysis and characterization of intracellular vesicles. We will show the validity of the method in controlled samples (a mixture of fixed beads in a coverglass) and successively we will compare the outcome of the algorithm with a fitting algorithm before moving to the analysis in living cells.

Sample preparation and experimental setup

Fluorescent Beads

A mixture of 100 nm (diluted 1:10,000 from stock solution) and 500 nm (diluted 1:100 from stock solution) yellow-green fluorescent beads (FluoSpheres carboxylate-modified microspheres, Thermofisher Scientific, Waltham, MA) was deposited on a polylysine-coated coverglass and imaged by a Nikon spinning-disk confocal microscope, based on the combination of a Yokogawa CSU-X1 confocal scanning unit and a Nikon Ti-E inverted microscope. A Nikon Plan Apo λ100x oil objective, NA 1.45, was used for all measurements. The pixel size was set to 110 nm. PLICS analysis was performed with threshold = 1000 and m = 16, these parameters where chosen in order to remove background (e.g autofluorescence contribution) and to maximize the sensitivity of the method in the expected size range (200-1000 nm). The image was segmented into a population with size <450 nm and a population with size >450 nm. Filtered ACFs were computed on the segmented images.

Live cell imaging

HeLa cells were plated on a LabTek eight-well chamber and let grow overnight. Cells were stained with 10 mg/mL pHrodo Green dextran (pHrodo Green dextran, molecular weight 10,000, Thermofisher Scientific) and left incubating for 20 min at 37°C, then washed twice in live-cell imaging solution (LCIS; Thermofisher Scientific) and resuspended in LCIS. For time-resolved measurements, cells were stained with 10 mg/mL pHrodo Green dextran and imaged without any washing step, leaving the fluorophore diluted in the buffer (LCIS). The samples were imaged by the Nikon confocal spinning-disk microscope equipped with a temperature- controlled stage kept at 37°C, using a Nikon Plan Apo λ 100x oil objective, NA 1.45, setting the pixel size to 110 nm or 160 nm. PLICS analysis was performed with threshold = 0.4B, B being the average background level before subtraction, and m = 10. For time-resolved experiments, rectangular regions of interest (ROIs) were selected inside the cell far from the plasma membrane. For each ROI, the number of vesicles of a given size was calculated. For cumulative results (n = 7 cells), the number of vesicles associated to a given population was calculated as the sum of the vesicles counted on each ROI. The error was estimated as equal to the square root of the calculated number, according to Poisson statistics. The dynamics of the number of vesicles, N_k, of population k as a function of time was fitted to the piecewise linear equation:

$$\begin{cases} \mathbf{0} & \boldsymbol{if} \quad \boldsymbol{t \le t_k} \\ \boldsymbol{N_{k,max}\frac{t-t_k}{\Delta t_k}} & \boldsymbol{if} \quad \boldsymbol{t_k < t < t_k + \Delta t_k} \\ \boldsymbol{N_{k,max}} & \boldsymbol{if} \quad \boldsymbol{t \ge t_k + \Delta t_k} \end{cases} \qquad \textit{Eq. 26}$$

where t_k represents the time at which the number of structures for population k is more than zero, then it increases linearly until it reaches a constant value of $N_{k,max}$ after a time delay Δt_k,

PLICS validation on fluorescent beads sample

The previously described PLICS analysis has been validated experimentally on a sample of mixed fluorescent spheres (nominal diameter d_1=100 nm and d_2=500 nm) imaged on a confocal microscope (***Figure 12 A***).

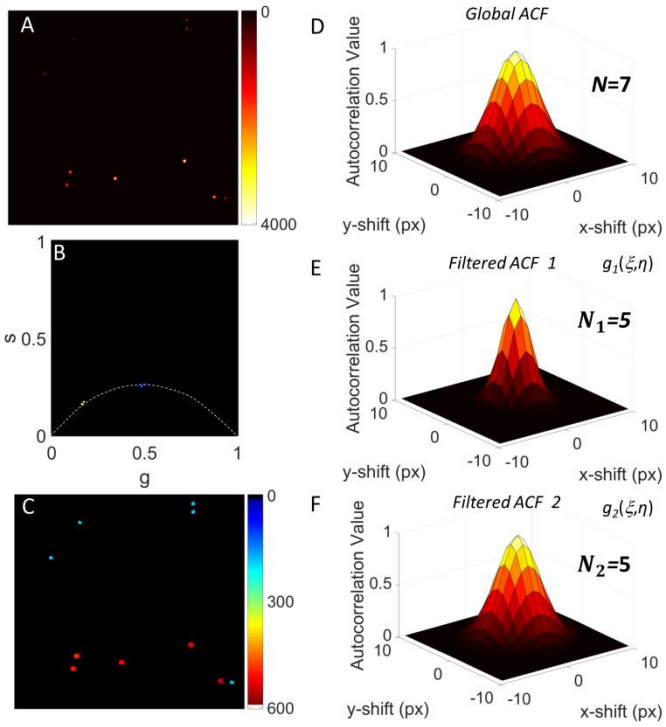

Figure 12 (A-C) Background-corrected image of a mixture of 100 nm and 500 nm fluorescent beads (A), associated PLICS phasor plot (B) and size image (C). (D) Global ACF $\hat{G}(\xi,\eta)$ of the background-corrected image. (E,F) Normalized filtered global ACFs $\hat{G}_1(\xi,\eta)$ and $\hat{G}_2(\xi,\eta)$ obtained after segmentation of the image with PLICS in Population 1 (size<450 nm) and Population 2 (Size>450 nm).

The PLICS analysis shows that two well separated populations are visible in the phasor plot (***Figure 12 B***) and in the size image (***Figure 12 C***). The absolute values of size here should be interpreted as the size of the particles convolved with the Point Spread Function (PSF) of the confocal microscope.

The segmentation of the image into two species yields two filtered ACFs (***Figure 12 E,F***) from which the correct number of beads, sorted by size, is recovered (N_1=5, N_2=5). In contrast, the total number obtained from the global ACF (***Figure 12 D***) is an underestimated value (N=7). It's worth to noting that, since the 100-nm beads are dimmer than the 500 nm beads, their contribution to the global ACF (***Figure 12 D***) is

significantly small compared to that of the brighter 500 nm particles; as a matter of fact, we can hardly note any difference between the global ACF and the filtered ACF associated to the larger beads (***Figure 12 D*** and ***F***, respectively).

PLICS validation on endocytic vesicles in living HeLa cells

We then validated our method on confocal images of live HeLa cells stained with pHrodo Green dextran, a pH-sensitive probe which selectively stains the intracellular vesicles formed following endocytosis of the dye (36). The phasor plot of the local ACFs shows a broad distribution along the reference trajectory (***Figure 13 C,D***).

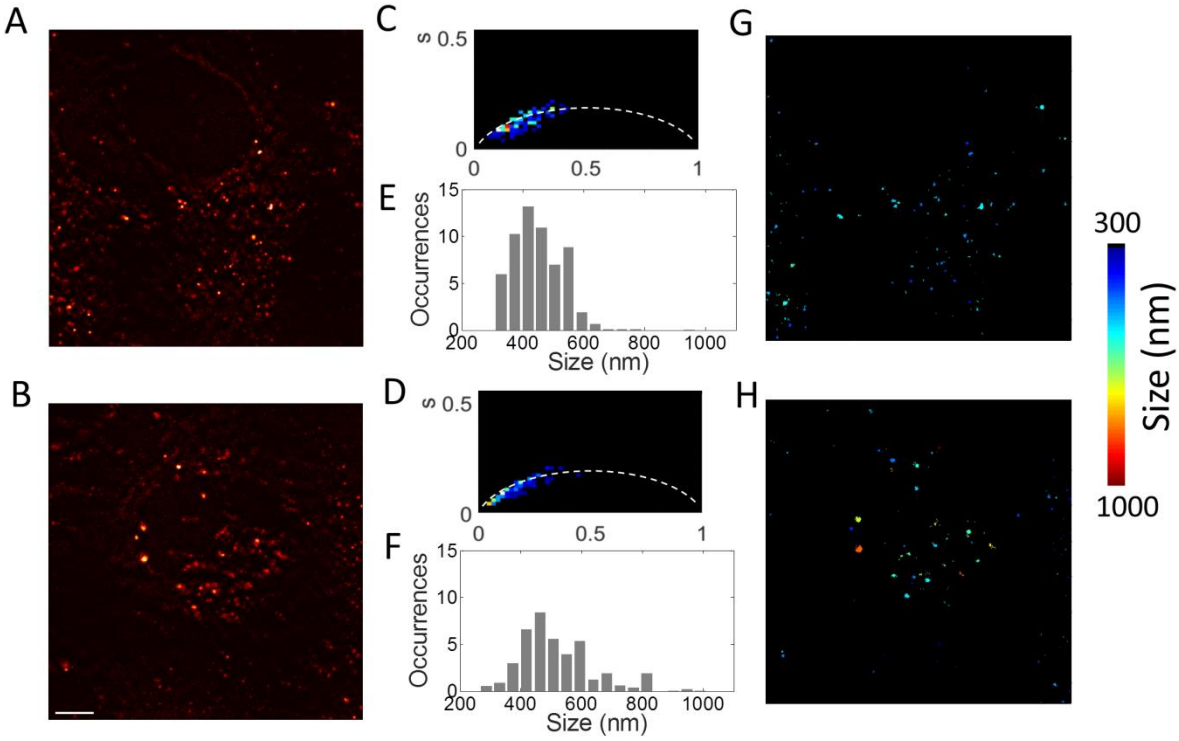

Figure 13: PLICS analysis of intracellular vesicles in confluent HeLa cells stained with pHrodo Green Dextran. Shown are the raw intensity images(A,B), the corresponding PLICS phasor plots (C,D), the size histograms (E,F) and the size images (G,H). Scale bar 5μm.

It's worth noting that, if background were not subtracted from the image, the experimental phasors would not lie along the reference trajectory. Indeed, addition of a spatially uncorrelated background causes a decrease in the modulation M of the phasor. The phasor plot can be used to investigate the size distribution associated to

different areas of the specimen (***Figure 13 C,D***). For instance, for the two areas shown in ***Figure 13 A*** and ***B***, one can tell from the phasor plots that in the second areas there are some larger vesicles compared to the first one.

Converting the phasor coordinates to absolute size, one can map the size of the vesicles in the images (***Figure 13 G,H***) and build the associated histograms (***Figure 13 E,F***). The mean values of size obtained from PLICS are $FWHM_{PLICS}$=459 nm and 514 nm (computed as the average size of all the structures) for the two regions respectively, whereas the corresponding values of size estimated from conventional ICS analysis are $FWHM_{ICS}$=357 nm and 439 nm respectively. Most of the vesicles in ***Figure 13 A*** have an apparent size between 350 nm and 550 nm whereas in ***Figure 13 B*** the distribution is broader and a significant fraction of vesicles has size greater than 550 nm. This difference can be due to heterogeneity in behavior from cell to cell or, more simply, to the fact that we are limiting the analysis to single optical sections and we cannot exclude that vesicles of different size might be located on different focal planes.

We checked that PLICS provides absolute values of size comparable with what can be achieved by performing a local 2D Gaussian fit of the images of the vesicles, as shown in ***Figure 14***.

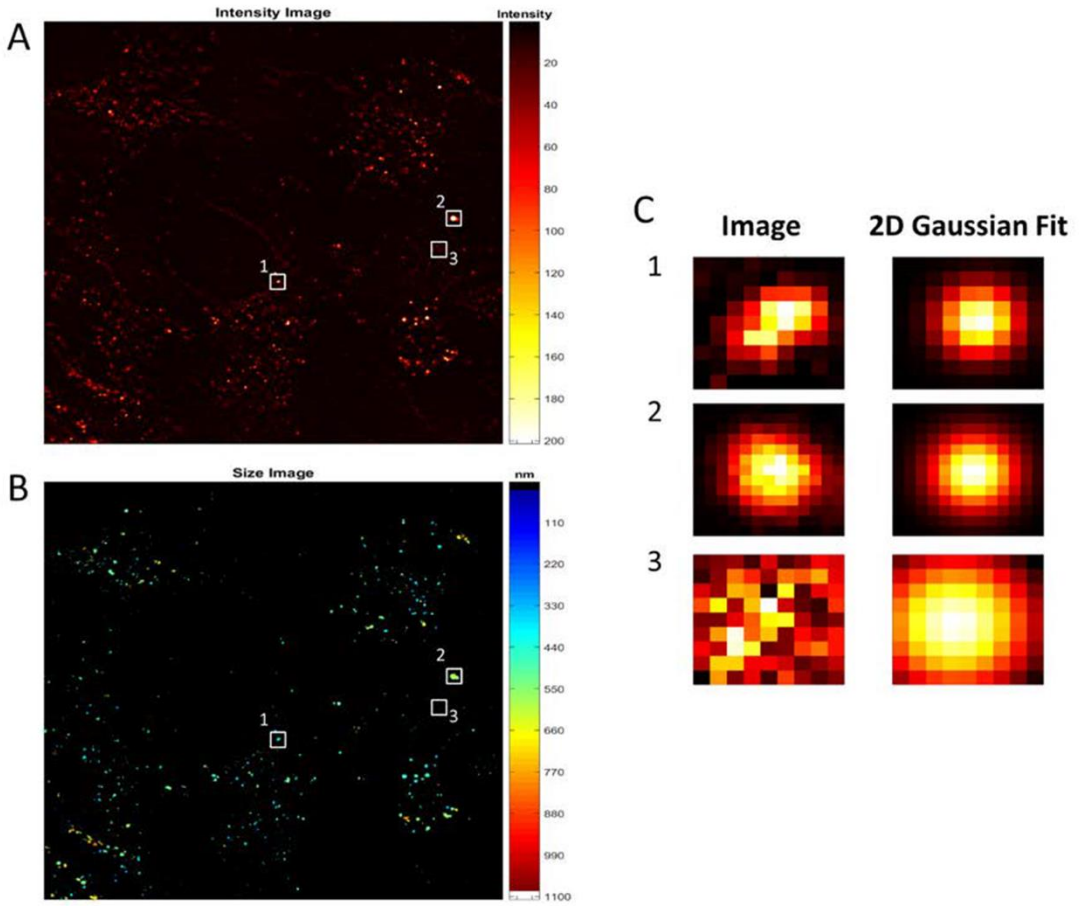

Figure 14: Comparison between the value of size obtained from PLICS and the value of size obtained from a fitting with a 2D Gaussian function. Three ROIs are chosen as example, highlighted in the intensity (A) and size image (B). A magnification is shown (C, left column) alongside with a 2D Gaussian fitting (C, right column). The size of the structures obtained by PLICS was 405 nm (ROI 1), 622 nm (ROI 2) and 964 nm (ROI 3), respectively whereas the 2D Gaussian fitting yields 405 nm (ROI 1), 618 nm (ROI 2) and 992 nm (ROI 3), respectively. The signal-to-background ratio of the three structures is 2.45, 4.86 and 0.36, respectively.

Endocytic vesicles maturation analysis

We finally monitored the size distribution of the vesicles as a function of the time elapsed from incubation with the dye (***Figure 15 A,B***).

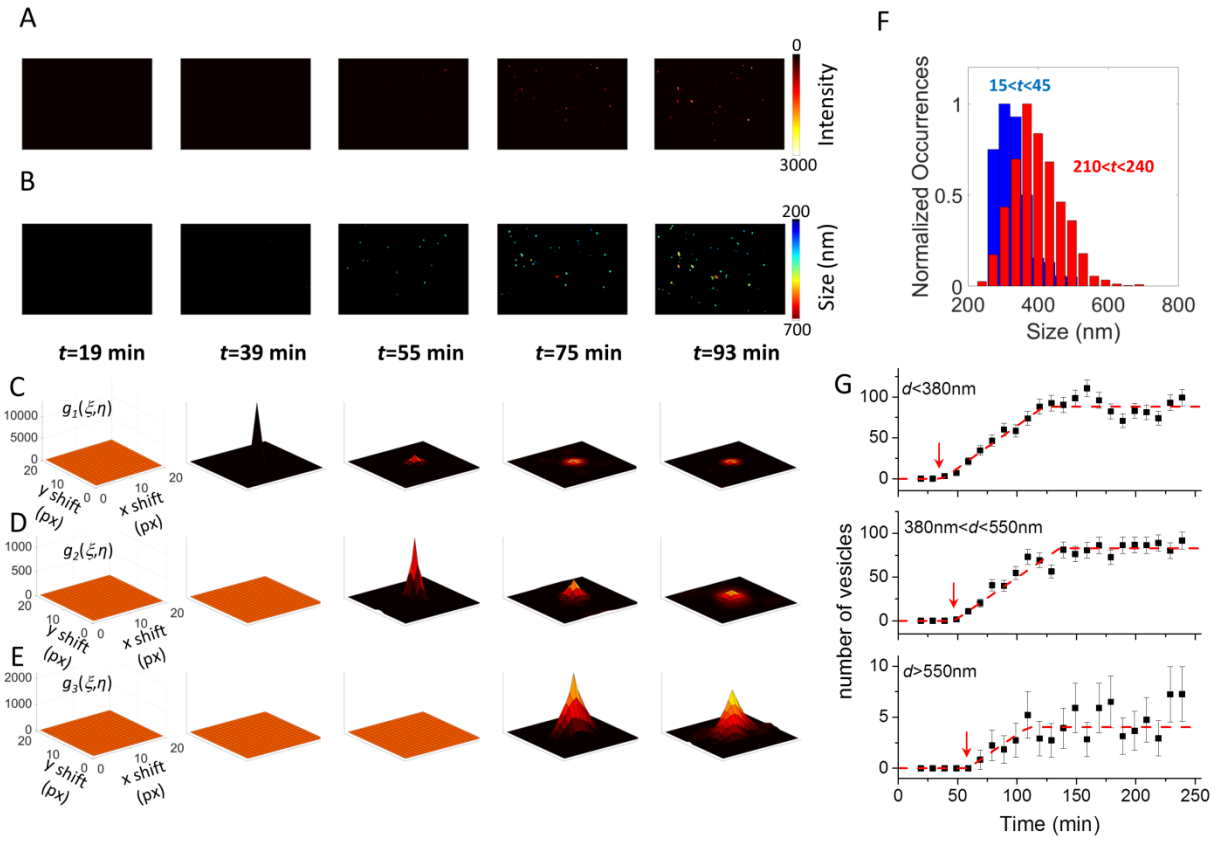

Figure 15 (A,B) Intensity and size images from a time sequence capturing the endocytosis process in a HeLa cell, corresponding to minutes 19,39,55,75 and 93 from incubation with the dye pHrodo-Green Dextran. (C,D,E) The filtered global ACFs associated to smaller (d_1<380nm), medium (380<d_2<550nm) and larger (d_3>550nm) vesicles and calculated for the same time frames. (F) Size histograms calculated for all the cells (n=7) and for the temporal interval 15min<t<45min (blue) and 210min<t<240min (red). (G) Average time course (n=7) of the number of small, medium and large vesicles. Each set of data has been fitted to a piecewise linear function to determine the time t_k at which the vesicles of kth population start to appear (t_1=38min, t_2=47min, t_3=59min; Δt_1=85min, Δt_2=89min, Δt_3=50min).

We started observing the cells 15 min after loading the extracellular medium with the dye and followed the time course of the internalization for as long as 4h. Intracellular vesicles start appearing at an incubation time of about half an hour and their number increases with time (***Figure 15 A***). A comparison of the normalized size-distribution at early (15<t<45min) versus late incubation times (210<t<240 min) shows that there is an increase in the average size of the vesicles (***Figure 15 F***). We then defined three

populations of vesicles (small, medium, large) based on their size (d_1<380 nm, 380<d_2<550 nm and 550<d_3<1100nm respectively) and counted the number of vesicles for each population from the filtered global ACFs as a function of time (***Figure 15 C-E***). Decreasing values of $\hat{g}_1(0,0)$, $\hat{g}_2(0,0)$ and $\hat{g}_3(0,0)$ indicate an increasing number of vesicles for each population as a function of time (***Figure 15 C-E***). On average (n=7 cells), the medium vesicles (d_2) appear with a 9 min delay with respect to the small vesicles (d_1), whereas the large vesicles (d_3) appear with a 12 minutes delay after the medium vesicles (d_2) (***Figure 15 G***). After appearance of the vesicles, their number grows until it reaches a constant value (***Figure 15 G***).

In the conditions of this experiment, since free dye is always available in the extracellular medium, the equilibrium is reached when the amount of dye internalized is equal to the amount of dye which is degraded or expelled from the intracellular vesicles. The dye will fluoresce only inside vesicles with acidic pH. The delay in the appearance of a vesicle of given size can be ascribed to the time it takes the dye to accumulate up to a detectable concentration inside that vesicle.

Even if our classification of the vesicles is based only on size and the three populations do not necessarily correspond to functionally different elements of the endosomal compartment, it's worth noting that our observations are in keeping with morphological changes associated to the endosome maturation program(1, 37, 38). Indeed, according to previous studies, primary endocytic vesicles fuse to early endosomes in about 10 minutes(38), whereas cargos typically show up in late endosomes 5–15 minutes later than in early endosomes (1). The time scale of these transitions is consistent with the time delays that we observed between the appearance of small, medium and large vesicles. Moreover, it is generally assumed that primary endocytic vesicles have smaller size (<200nm) with respect to early and late endosomes (size in the range 200 to 1000 nm) and that endosomes grow in size during maturation(38). However, further studies with more specific markers are required to assign a functional role to each type of vesicle.

2.5 PLICS: Other applications

In the following we will present several other applications for the PLICS algorithm. PLICS is being used on a project in collaboration with Francesco Cardarelli, CNR institute for Nanoscience at NEST (NEST, CNR-NANO, PISA) for the size characterization and mapping of insulin granules undergoing different treatments. PLICS is used in this context as a method for the size determination and evolution over time of the granules and the analysis of their spatial distribution in the cell.
Another application of interest is the extension of PLICS to non-sparse samples, like non-spherical cellular organelles.

PLICS can be extended to the analysis of non-spherical objects by replacing the angular average of the local ACF with an angle-wise analysis. For every pixel or structure we will therefore obtain a collection of N angles with their respective size, from which we can compute the orientation and eccentricity of the structure of interest; this simple- modification allows for the analysis of more complicated and continuous structures like chromatin and microtubules (***Figure 16***).

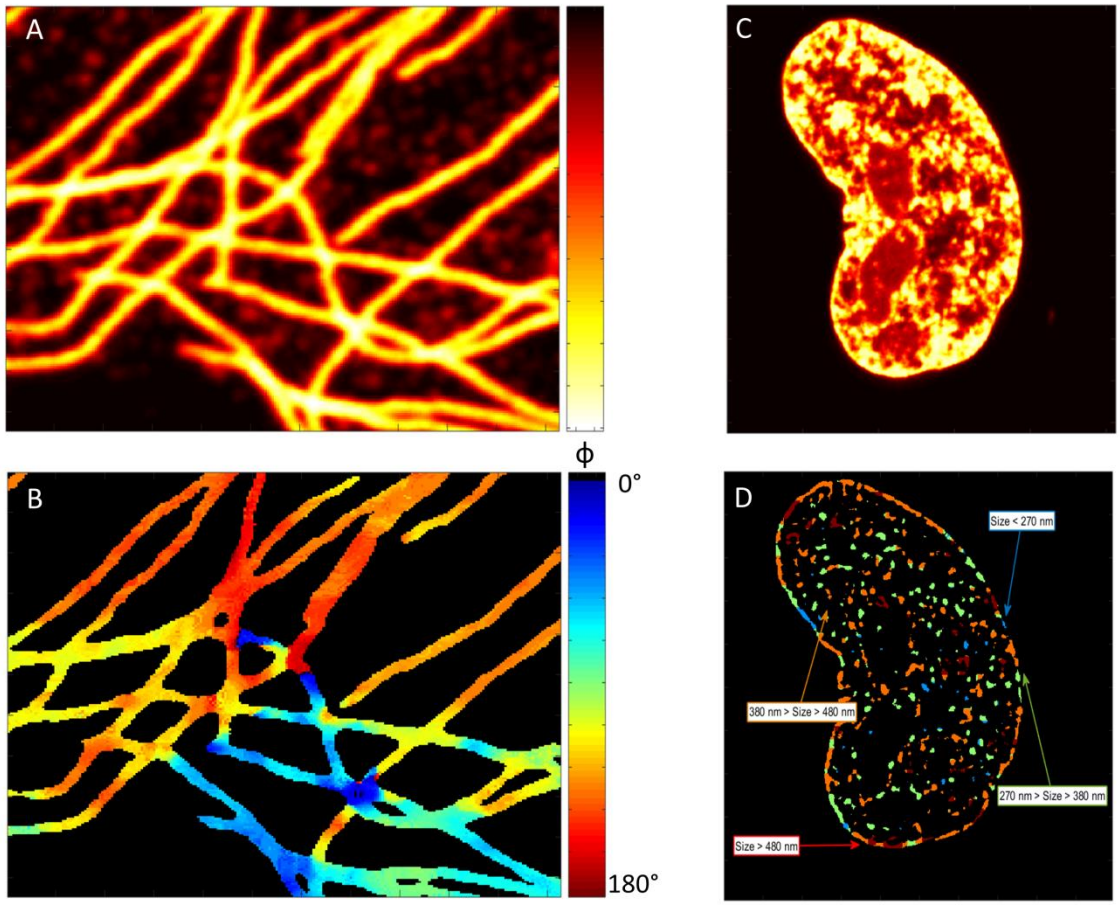

Figure 16: Confocal image of microtubules (A) and orientation image (B) obtain by asymmetric PLICS. Chromatin (C) stained with Hoechst and chromatin fiber size map (D, minimum profile). The size image in (D) was segmented in four regions: size<270nm (blue), 270nm>size>380nm (green), 380nm>size>480nm (orange) and size>480nm (red).

We define as local orientation the angle at which the highest value of size is measured (s_{max}) and we compute the eccentricity as:

$$e = \sqrt{1 - \frac{s_{min}^2}{s_{max}^2}} \qquad \textit{Eq. 27}$$

where s_{min} is the size measured at the angle which is perpendicular to the local orientation angle. This analysis can be applied to the study of mitochondrial shape: in ***Figure 17*** we can see an example of thickness and eccentricity analysis on mitochondria in a living HeLa cell.

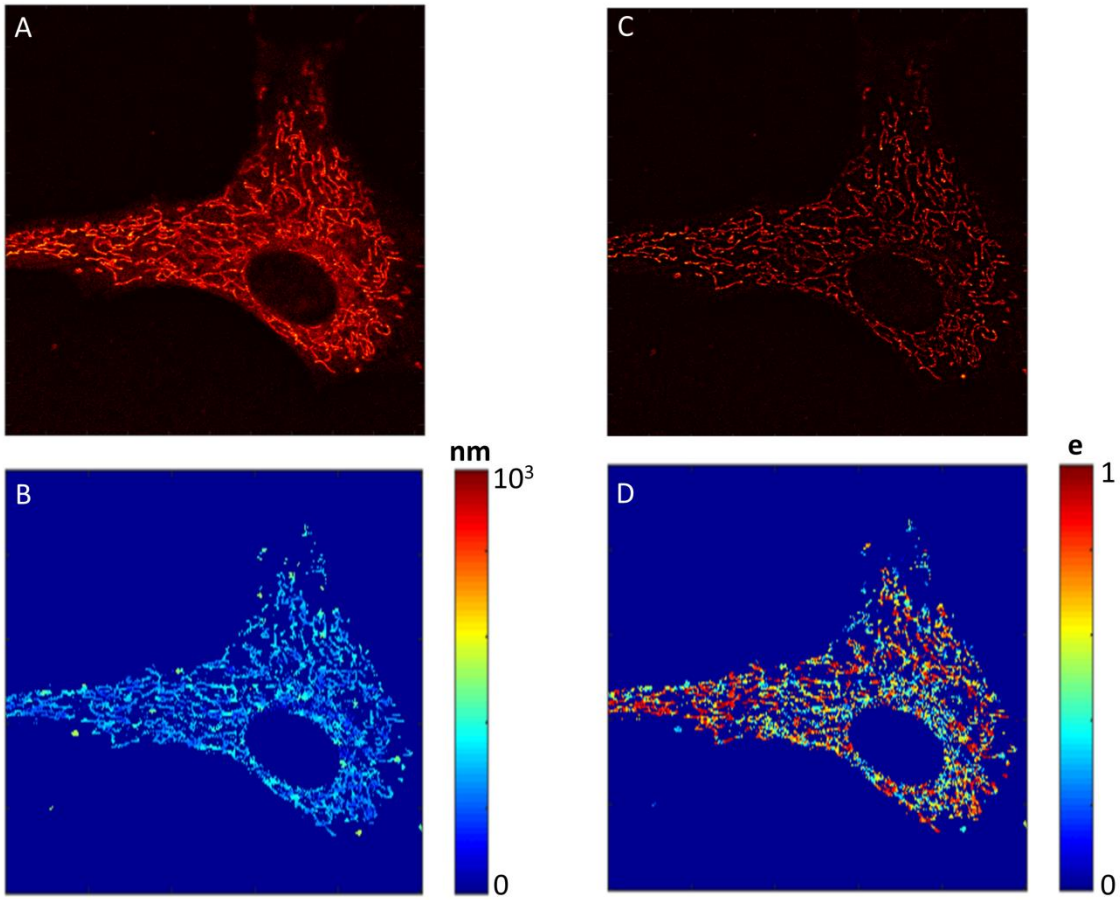

Figure 17: Original (A) and background corrected (C) image of mitochondria in a living HeLa cell stained with MitoTracker Green. Thickness (B) and eccentricity (D) maps of the same cells, analyzed with a mask m=32.

CHAPTER 3 Phasor analysis of Local Image Cross-Correlation Spectroscopy (PLICCS): inter-structure distance analysis

3.1 Local image cross-correlation spectroscopy

Image cross-correlation spectroscopy

Image cross-correlation spectroscopy (ICCS) has been introduced in the early 2000's as a two-colors extension of ICS (38-40). Instead of computing the ACF of a single image, it relies on the computation of a spatial cross-correlation function (CCF) between two different images, for instance showing two differently labeled species. The analytical form of the CCF is:

$$g_{12}(\xi,\eta) = \frac{<\delta I_1(x,y)\delta I_2(x+\xi,y+\eta)>}{<I_1(x,y)><I_2(x,y)>} \qquad \textit{Eq. 28}$$

where $I_1(x,y)$ and $I_2(x,y)$ refer to the images to be cross-correlated. In the following we will refer to them as "channel 1" and "channel 2", respectively. One of the first applications of ICCS was the quantification of colocalized species, and it was compared to the Pearson's and Manders' correlation coefficients (41); in that case, Wiseman and co-workers were able to define the number of interacting particles, namely the number of colocalizing strucutres, as:

$$< N >_{12} = \frac{G_{12}(0,0)}{G_{11}(0,0)G_{22}(0,0)} \cdot \frac{A_2}{A_1} \qquad \textit{Eq. 29}$$

where $A_1 = \pi w_1^2$ and $A_2 = \pi w_2^2$ are the areas of the focal spot of the first and second channel and $G_{11}(0,0)$ and $G_{22}(0,0)$ are calculated from the ACFs of the first and second channel, respectively. The number of colocalizing species can be normalized to the total number of species either in the first or in the second channel, in order to obtain two colocalization coefficients: $M_{1,ICCS}$ and $M_{2,ICCS}$. Cross-correlation can also be used in order to evaluate the distance between two structures, for instance

a moving structure in different frames of the same video sequence or two distinct structures in two different channels. Let's consider two Gaussian-shaped structures:

$$\begin{cases} \boldsymbol{G_1(\vec{r}) = A_1 \cdot e^{-\frac{(\vec{r}-\vec{c}_1)^2}{2\sigma_1^2}}} \\ \boldsymbol{G_2(\vec{r}) = A_2 \cdot e^{-\frac{(\vec{r}-\vec{c}_2)^2}{2\sigma_2^2}}} \end{cases} \qquad \textit{Eq. 30}$$

centered in $\vec{c}_1$ and $\vec{c}_2$ with a variance of σ_1^2 and σ_2^2, respectively. Their cross-correlation function $g_{12}(\vec{\rho}) = G_1(\vec{r}) \otimes G_2(\vec{r})$ will still be a Gaussian but centered in $\overrightarrow{\delta r} = \vec{c}_1 - \vec{c}_2$ and with a variance of $\sigma_{12}^2 = \sigma_1^2 + \sigma_2^2$:

$$\boldsymbol{g_{12}(\vec{\rho}) = g_{12}(0) \cdot e^{-\frac{(\vec{\rho}-\overrightarrow{\delta\rho})^2}{2\sigma_{12}^2}}} \qquad \textit{Eq. 31}$$

Here, $\overrightarrow{\delta\rho} = \overrightarrow{\delta r}$ is the distance between the centers of the two structures.

If the cross-correlation is between two frames of the same video sequence, $\overrightarrow{\delta r}$ represents the distance traveled by the particle during the acquisition time, while if the cross-correlation is between two different channel, $\overrightarrow{\delta r}$ would represent the spatial separation between the two structures.

Algorithm

The algorithm described in ***CHAPTER 2*** for PLICS has been adapted for retrieving the local distances between the structures in one channel with respect to the structures in the other. The workflow of the algorithm is shown schematically in ***Figure 18*** for a two-colors image of distributed Gaussian-shaped structures (***Figure 18 A)***.

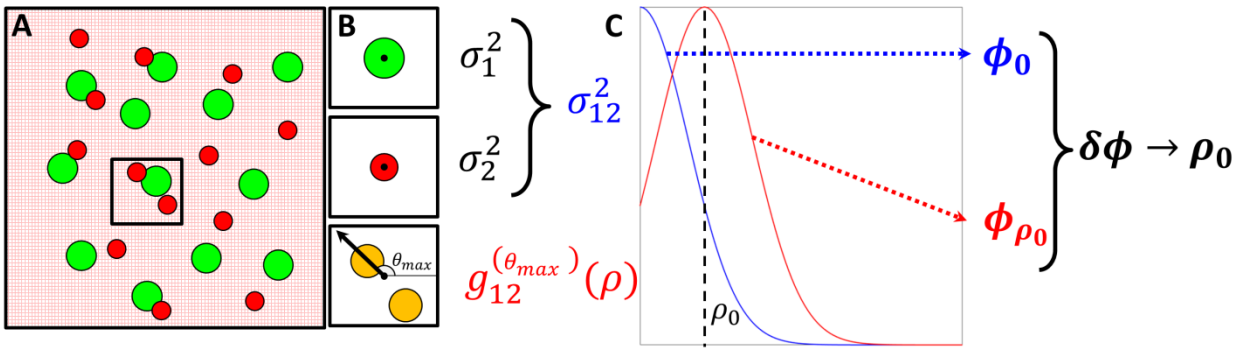

Figure 18: Schematic workflow of the PLICCS algorithm: Schematic image of green and red structures (A) from which $g_{11}(\vec{\rho})$ (B, top) and $g_{22}(\vec{\rho})$ (B, middle) are computed in order to obtain σ_{12}^2 by PLICS. From the same region $g_{12}(\vec{\rho})$ (B, bottom) is computed, and only the profile from (0,0) passing through the maximum is considered ($g_{12}^{(\theta_{max})}(\rho)$, black arrow), the procedure is iterated until all spots are computed (twice in this example). σ_{12}^2 is used to compute the phase $\boldsymbol{\phi_0}$ of the zero-shifted Gaussian profile (blue curve in C), while the $g_{12}^{(\theta_{max})}(\rho)$ (red curve in C) will have a different phase $\boldsymbol{\phi_{\rho_0}}$ due to the shift from zero. The phase difference $\delta\phi$ between the two is then scaled with the appropriate calibration function in order to obtain ρ_0 (the distance of the maximum of the CCF from the center), which corresponds to the inter-structure distance.

The algorithm first analyzes every single channel with PLICS in order to obtain the local size of the structures (σ_1^2 and σ_2^2, ***Figure 18 B, top*** and ***middle***) and then computes the local cross-correlation function (CCF) between the two channels (***Figure 18 B, bottom***). The values σ_1^2 and σ_2^2 are used to calculate the expected size of the cross-correlation spot, $\sigma_{12}^2 = \sigma_1^2 + \sigma_2^2$. According to ***Eq. 31***, any local cross-correlation spot is expected to have a size of σ_{12}^2 and to be centered in $\overrightarrow{\delta\rho}$ i.e., in polar coordinates, at a distance $\delta\rho$ along the orientation θ_{max}. The angle θ_{max} is determined by finding the position of the maximum of the CCF. In order to find $\delta\rho$, the algorithm considers only the radial profile along the direction θ_{max} (as shown in ***Figure 18 B bottom***, black arrow) and calculates, via FFT, a phase value $\boldsymbol{\phi_{\rho_0}}$. This value is compared with the phase value $\boldsymbol{\phi_0}$ associated to the zero-centered cross-correlation spot of size σ_{12}^2 (***Figure 18 C,*** blue curve). From the difference in phase between the zero-centered and the shifted profile, $\boldsymbol{\phi_0} - \boldsymbol{\phi_{\rho_0}}$, it is possible to obtain the distance $\delta\rho$

from the two structures. This is done by scaling the retrieved difference with an appropriate calibration curve, obtained by simulations, like in the PLICS algorithm.

If there is more than one spot per channel in the same ROI, it is possible to iterate the procedure in order to obtain the distance from all the structures. For instance, in our application, the typical number of spots per ROI in each of the two channels varies between 0 and 2 and we use ICS in the single channels ROIs in order to evaluate the number of iterations to be carried out. For instance, for the ROI selected in the schematic ***Figure 18 A***, the local ACFs in the two channels (***Figure 18 B, top*** and ***middle***) are analyzed by ICS in order to determine that there are two red particles and one green particle. Successively, the local CCF (***Figure 18 B, bottom***) is analyzed with a number of iterations equal to 2.

In summary, the PLICCS algorithm returns, for every image of size MxN, one stack of images MxNxP per channel, where P is the maximum number of iterations performed in the local ROIs, containing the distance maps. The distance maps shown in the following will be MxN images, where the distance displayed is the minimum non-zero distance computed, corresponding to the distance from the closest structure in the other channel. The algorithm returns also the size maps obtained by PLICS for the two channels, it's worth noting that the choice of the mask for PLICS is independent from the choice of the mask for the cross-correlation.

Relative Distance Distribution (RDD) analysis

With PLICCS is possible to obtain the local value of distance between the structures in the two channels. Using this information we can characterize their relative spatial distribution, for instance we can determine if the structures are randomly distributed one with respect to the other or if there's any systematic deviation from a random distribution. In this respect, we developed a method which is a more straightforward variation of the so-called G function (42). Here we will present the concept, its validation and the determination of a confidence interval. ***Figure 19 A*** shows a schematic example of randomly distributed structures in the red and green channel.

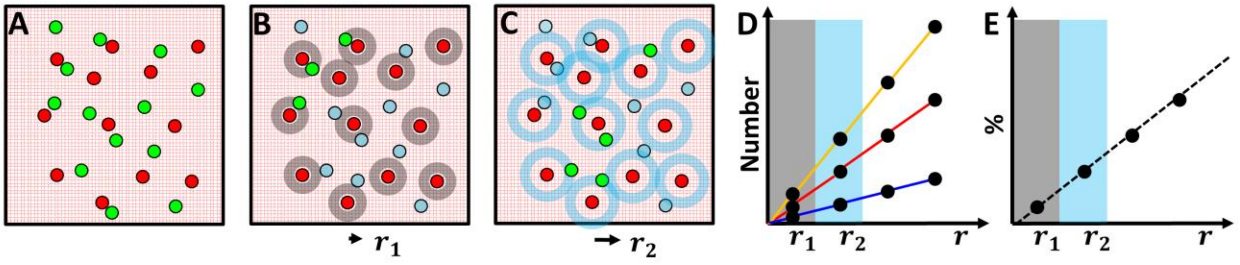

Figure 19: Schematic representation of RDD analysis. (A) A two channels image is analyzed by PLICCS. (B,C) RDD curves are computed by counting only the green structures located at a certain distance from the red structures and progressively increasing the distance. For instance, figure B shows the structures used for the computation at distance $\boldsymbol{r_1}$ (green) while figure C shows the structures used for the computation at distance $\boldsymbol{r_2}$ (green). Non-normalized RDD curves (D) relative to a different total number of structures (total number increasing from the blue curve to the orange one) and normalized RDD curve (E, black dashed line).

Using the red dots as center, we select only the green structures we can find at a distance r=$\mathrm{r}_1 \pm \delta r$ (***Figure 19 B***, green dots) by using the PLICCS distance maps (for the green channel, in this example) for filtering, ultimately obtaining a filtered image with only the green structures that are at the defined distance from the structures in the red channel, and we count them with ICS in order to obtain the number of structures L_1 found at a distance r_1. The thickness of the ring ($2\delta r$) is chosen so that there is always at least one structure in the filtered global image. The procedure is then iterated at increasing distances (e.g. r=$\mathrm{r}_2 \pm \delta r$, ***Figure 19 C***, green dots) up to a cutoff value r_n. The $L_{1,\dots,n}$ values are normalized so that $\sum_{i=1}^{n} \widetilde{L_i} = 100$, (where $\widetilde{L_i}$ denotes the normalized number found at a distance r_i) and we finally obtain the RDD curve (***Figure 19 E***), defined as $\tilde{\boldsymbol{L}}(\boldsymbol{r})$, for the green channel. Without the normalization step, the RDD curves would have different slopes according to the total number of green structures, N_{tot}, although their shape would remain unchanged (***Figure 19 D***). In the following we will refer to the normalized RDD curves simply as RDD curves. Note that $\sum_{i=1}^{n} L_i = L_{tot} \geq N_{tot}$, since a structure can be counted more than once, L_i should be interpreted as a "link" or segment linking each particle with a particle of the other color and L_{tot} is the number of links considered in the analysis.

In the case of randomly distributed structures, the RDD increases linearly with the distance, because a ring of larger radius can contain a larger number of structures

(***Figure 19 B,C,D***, gray and blue shades). In principle, we could compute the RDD for both the channels and they would lead to the same result, so in the following we will only refer to the RDD computed for the green channel, as explained in ***Figure 20***.

Assuming there is some degree of organization in the sample (e.g. green dots are systematically closer or farther away from the red ones), the distribution deviates from the linear case (***Figure 20 B,C***).

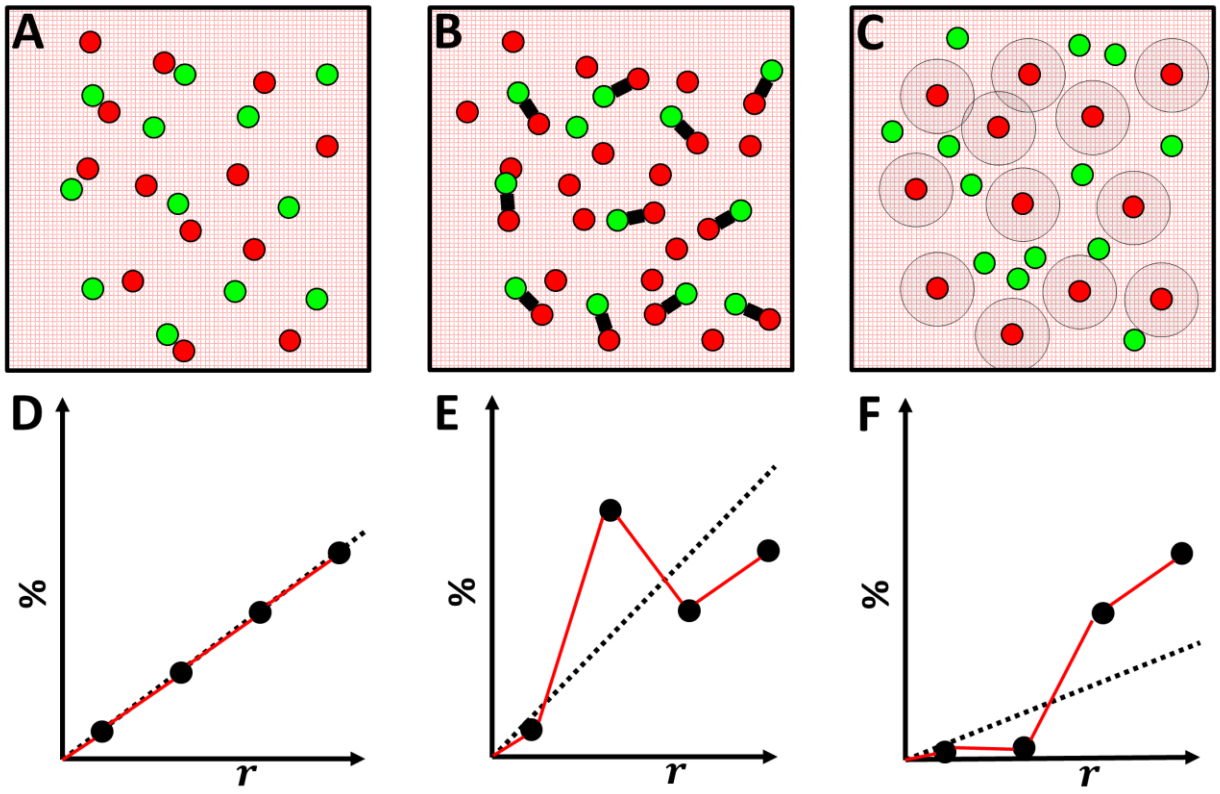

Figure 20: Schematic representation of different relative distributions: random (A), random and dimers (B, dimerization shown as black links) and excluded (C, excluded area shown as gray circles). The corresponding normalized RDDs (red lines in D,E and F, respectively) are compared with the RDD relative to a random distribution (black dashed line)

For instance, if the green dots can dimerize with the red ones at a well-defined distance, the RDD will increase at the dimerization distance and then drop at longer distances (***Figure 20 B,E***). Another configuration is represented by a repulsive case in which a green dots cannot be located closer than a certain distance from a red one, causing the RDD to drop at distances shorter than the cutoff distance and then rising again above the random distribution (***Figure 20 C,F***).

This RDD analysis relies on the relative distance distribution and its deviation from the random case so, for a correct interpretation of results, it's crucial to define a confidence interval stating if the deviation is significant or not. In analogy to other methods, for instance (42), that use a 95% confidence envelope derived from a series of simulations, we will exploit Poissonian statistics in order to define, a priori, a confidence interval based on the actual sample. Let us assume we are sampling the RDD in N intervals located at a distance $r_{1,\dots,N}$, the random reference curve will increase linearly, so it can be described by $\widetilde{L_i} = \frac{r_i}{\sum_{i=1}^{N} r_i} \cdot 100$. Let us also assume that the total number of links is L_{tot}, so that the corresponding number of structures per interval if they were randomly distributed is equal to $N_i = \frac{\widetilde{L_i}}{100} \cdot L_{tot}$, and the standard deviation associated to that bin, assuming a Poisson distribution, is $\sqrt{N_i}$. Considering the normalization and considering twice the standard deviation in order to guarantee a confidence of 95%, we calculate the error associated with the ith interval as $\frac{2\sqrt{N_i}}{L_{tot}} \cdot 100$.

As a validation of the proposed approach, we simulated and analyzed 50 random datasets, from which we calculated the individual RDDs and compared the average RDD with the theoretical random RDD (***Figure 21 A***, blue and black lines, respectively) and twice the standard deviation with the theoretical 95% confidence interval (***Figure 21***

A, error bars and blue area, respectively).

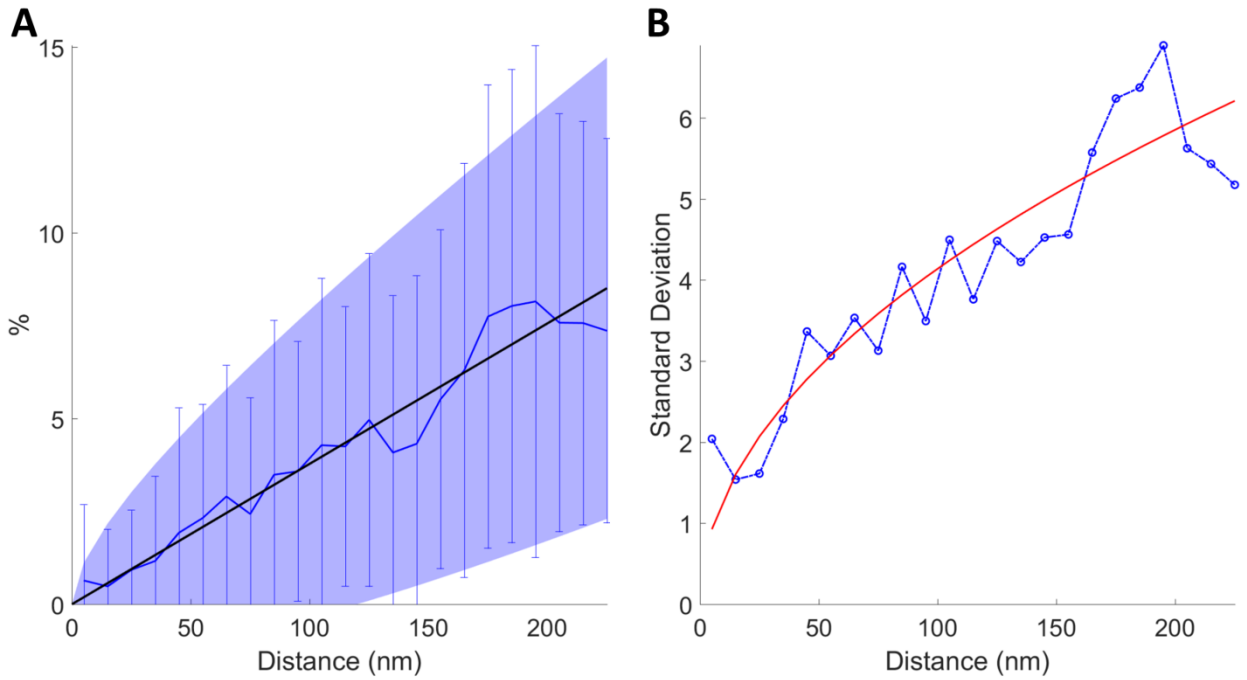

Figure 21: Average RDD curve (A, blue line) calculated over 50 simulations or randomly distributed structures compared with theoretical random curve (A, black line). The error bars represent twice the standard deviation of the mean curve, while the blue area shows the theoretical 95% confidence interval. Comparison of experimental (B, blue line) and theoretical (B, red line) standard deviation as a function of distance.

We can appreciate that the calculated distribution and error match with the expected values, in particular, the trend of the error is clear in the plot in ***Figure 21 B***, which shows the comparison of the calculated standard deviation as a function of distance (blue curve) with the theoretical one (red line).

3.2 PLICCS for the characterization of nuclear foci

Here we show application of this analysis method to the study of the distribution of replication and transcription foci, which represent the locations in the cell nucleus where, at a given moment, DNA is being replicated and transcribed, respectively. It has been shown (43) that the machinery related to the two processes can collide, resulting in undesired mutations and replication errors which can be related to cancer formation and progression. Occurrence of transcription-replication collisions can be observed by next-generation sequencing techniques (44). In order to observe these collisions in

intact, single cell nuclei, foci can be stained using two modified nucleic acids, 5-Ethynyl-2´-deoxyuridine (EdU) and 5-Bromouridine (BrU), which are incorporated in nascent DNA and RNA, respectively, and can be immuno-labeled for visualization. The results shown here are part of a bigger project aimed at studying the effect of oncogene activation on replication-transcription collisions in a cellular model of cancer. My specific role in this project was to develop an algorithm for the analysis of the spatial distribution of foci from dual-color super-resolved images. For this study we used MCF10A cells.

Simulations

Several simulations were ran in order to explore different modalities of structural organization that could be found in the real sample. Some examples of simulations are shown in ***Figure 22***, in which we consider a random distribution (A), a large (B) and a small (C) excluded volume and two dimers samples with long (D) and short (E) dimerization distance. The same types of distribution were simulated in 3D. In our super-resolved STED microscope the improvement of spatial resolution is achieved only in the x-y plane but not in the z-axis. For this reason we simulated images of the 3D distributions obtained with an optical sectioning of 520 nm.

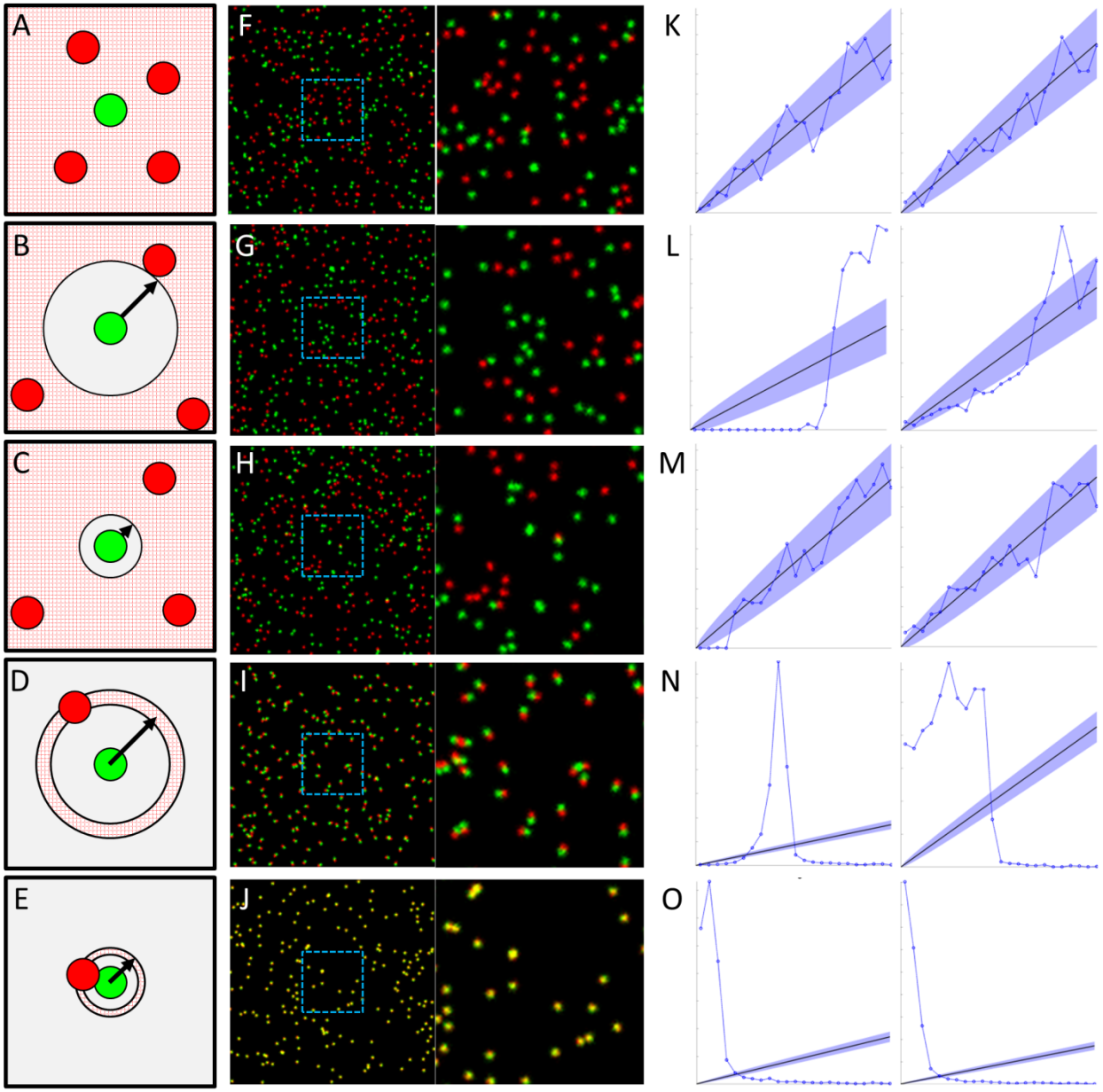

Figure 22: Schematic representation of simulated samples: randomly distributed (A), repulsive (B, r=160 nm and C, r=40 nm) and dimers (D, d=100 nm and E, d=20 nm) along with examples of simulated images (F-J, left) and magnification of the highlighted region (F-J, right). RDD curves corresponding to 25 simulations in the 2D (K-O, left) and 3D case (K-O, right). The structures are simulated with SNR=30

The same structural organization is shown in the 2D (***Figure 22 K-O, left***) and in the 3D (***Figure 22 K-O, right***) case. Although expected, it is important to notice that the random distribution is the same in the 2D and 3D case (***Figure 22 K***), therefore the reference curve is independent on the sectioning capability of the microscope. On the

contrary, if we consider other modalities of structural organization (***Figure 22 L-O***), the differences can be important. For instance, in the case of exclusion with r=160 nm (***Figure 22 L***), the deviation from the random case is striking in the 2D case while in the 3D case the curve barely leaves the confidence interval; as a matter of fact, if we decrease the exclusion radius to r=40 nm (***Figure 22 M***), the deviation in 2D is already difficult to appreciate, while in 3D the RDD is indistinguishable from the random case.

Results: RDD of NanoRulers

The method has been first tested on controlled samples, namely two samples of nanorulers purchased from GATTAquant (http://www.gattaquant.com/). These nanorulers exploit DNA origami technology in order to construct structures labeled with the chosen fluorophores and placed at a well-defined distance. The nanorulers used in our experiments were designed to have a fixed distance (d=20 nm or d=100 nm) between two structures labeled with different fluorophores. They were specifically designed so that the green structure was labeled with Chromeo-488 and the red structure was labeled with Atto-532. These are the same fluorophores that will be used for the two-color analysis of the biological samples. Representative two colors STED images of nanorulers are shown in (***Figure 23***).

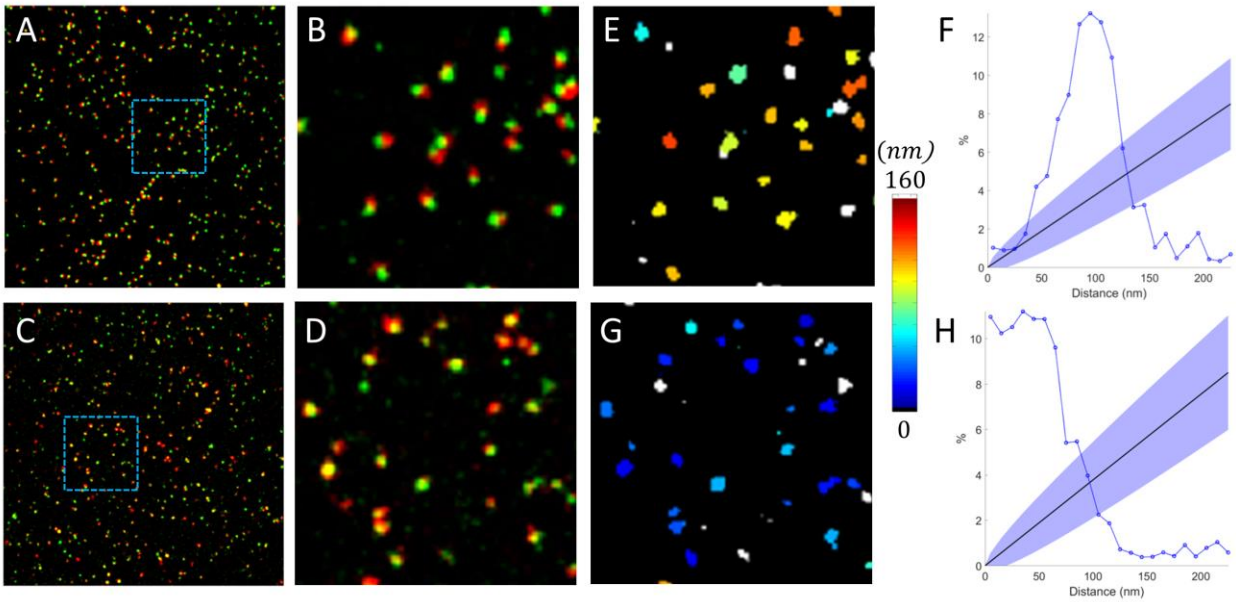

Figure 23: Nanorulers images (A-B, $d_1 = 20$ nm and C-D, $d_2 = 100$ nm) and corresponding distance maps (E and G, respectively) for the green channel, together with relative distance distributions (F and H, respectively). The fitting of the RDDs yields $d_1 = 30 \pm 42$ nm (F) and $d_2 = 96 \pm 26$ nm (H)

The RDDs resulting from the analysis of nanorulers images were fitted with a linear function plus a Gaussian, from which the center and standard deviation of the Gaussian component are considered as average value and error. The fitting of the RDDs for the two NanoRulers samples yields $d_1 = 96 \pm 26$ nm (***Figure 23 F***) and $d_2 = 30 \pm 42$ nm (***Figure 23 H***). The deviation from a random distribution is significant and the recovered peak-distance values are in keeping with the expected ones. Being a local approach, PLICCS allows for the construction of distance maps (***Figure 23 E,G***) that can give information about the spatial distribution of the structures; for instance, it is possible to visually separate the structures that do not have any structure of the other color within the local mask (white structures) from the others (colored structures). PLICS analysis on the NanoRulers sample returns a resolution for the STED acquisition of 72 ± 27 nm for the green channel and 96 ± 30 nm for the red one.

Results: RDD of nuclear foci

As biological samples, we first considered two different stains: EdU vs PCNA (***Figure 24 A-B***, green and red, respectively) and histone H3K9met vs BrU (***Figure 24 C-D***, green and red, respectively).

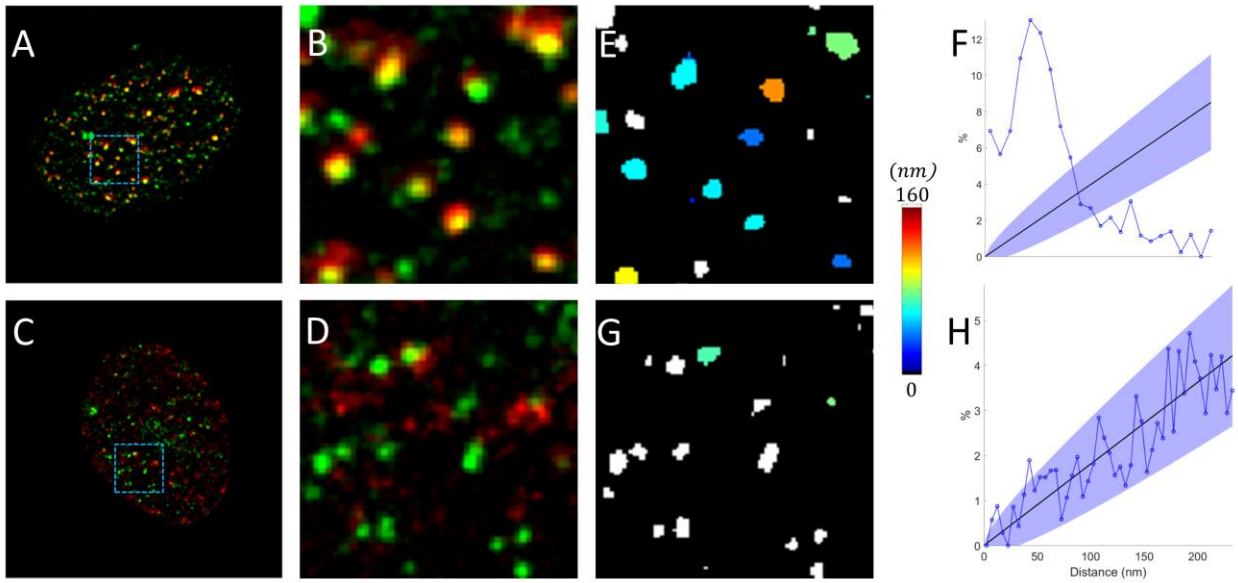

Figure 24: Example of images of EdU-PCNA (A,B) and H3K9met-BrU (C,D) samples together with corresponding distance maps for the green channel (E and G, respectively) and RDDs (F and H, respectively).

As mentioned before, EdU is incorporated in replicating DNA while PCNA is a protein involved in the replication machinery, therefore the two processes are expected to be spatially close to each other. By analyzing the RDD of the sample (***Figure 24 F***) we can clearly see a deviation from the random RDD, and we can extract a characteristic distance for the two processes of $d_{\mathrm{EdU/PCNA}} = 47 \pm 29$ nm. On the contrary, in the H3K9met-BrU sample, this particular histone tri-methylation is present in highly condensed chromatin (heterochromatin), while BrU is known to be incorporated in transcribed RNA, therefore the two processes are not functionally linked to one another and, consequently, the RDD does not significantly deviate from the confidence interval (***Figure 24 H***). This behavior can be due to two distinct reasons: the two processes can occupy random positions in the cell with respect to one another or this can be a case of excluded volume configuration in which the volume cannot be quantified due to either low statistics, 3D contribution, short exclusion distance or a combination of these factors.

Finally, we consider the EdU vs BrU sample in order to calculate the RDD of the two processes and evaluate if the RDD analysis could be used as a technique to quantify

the impact of the transcription-replication collisions. An example of the analysis is shown in ***Figure 25***, in which we can see a typical EdU vs BrU labeling (***Figure 25 A-B***) and the cumulative RDD (***Figure 25 C***).

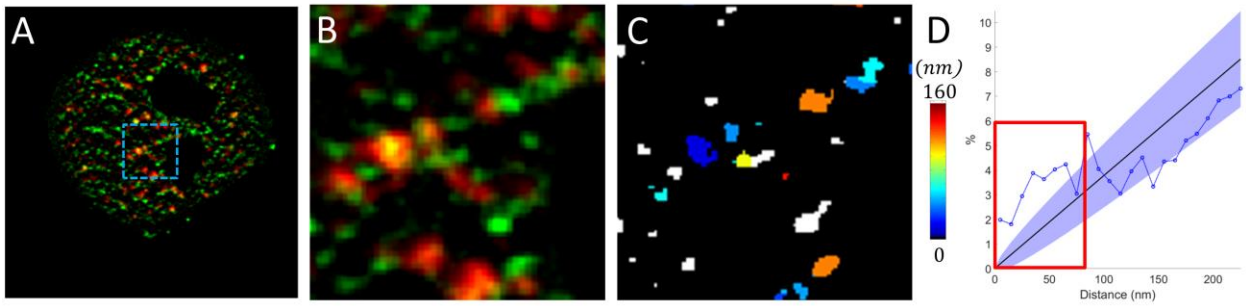

Figure 25: Example of image of EdU-BrU (A-B) sample together with corresponding distance map (C) and relative distance distributions (D). The red rectangle in D highlights the region of deviation from the confidence interval.

From the highlighted region in ***Figure 25 C*** it's easy to see a consistent deviation from the random distribution at short distances, meaning that the two processes are more likely to happen within 100 nm with respect to a random distribution. This behavior could be explained by the fact that both processes involve de-condensed strains of DNA.

3.3 PLICCS: Single particle tracking

PLICCS for single particle tracking

With few modifications, PLICCS can be used as a localization algorithm for single molecule localization microscopy (SMLM) or single particle tracking (SPT). As a matter of fact, if we cross-correlate an image of the structure we want to localize with an image (e.g. a simulated one) of a structure in a known position, PLICCS will localize the unknown structure with subpixel precision. This implementation gives the x-y localization of the structure and completes the number of parameters that can be retrieved when fitting a Gaussian structure with phasors, as we started showing in the paragraph ***Gaussian "fitting" with phasors***. In the following we will show how we characterized the performances of this method for x-y localization as opposed to other localization algorithms and, later on, we will show how we evaluated the z-position in a novel fast volumetric imaging system.

Comparison with LMS Gaussian fitting and centroid localization

We compared PLICCS localization algorithm with least mean squares (LMS) Gaussian fitting, centroid localization and cross-correlation and, in order to evaluate its performances, we considered the following parameters: bias, precision, speed and SNR stability.

Bias: Bias is defined as $B(\hat{x}) = \langle x \rangle - \hat{x}$, where $\langle x \rangle$ is the mean position as averaged over several realizations and $\hat{x}$ is the real simulated position. Bias is used as a function of the real position in order to evaluate if the system has a systematic shift toward certain values when localizing with sub-pixel precision, as reported for instance with centroid localization (45).

Speed: Speed is defined as the average execution time of the localization function.

SNR: Signal to noise ratio is defined as: $\frac{N_{signal} - \langle N_{background} \rangle}{\sqrt{N_{signal}}}$, where N_{signal} is the number of photons used to sample the structures, and $\langle N_{background} \rangle$ is the average photon count of the background. In the following, $\langle N_{background} \rangle$ is fixed to 10 and only N_{signal} is used to tune the signal to noise ratio.

Precision: Precision is defined as the standard deviation of a set of localizations of structure with the same position but with different noise realizations and it defines localization accuracy. The theoretical limit for the localization precision is given by

$$\boldsymbol{\sigma^2_{theo}} = \frac{\boldsymbol{\sigma^2_{Gauss}} + \boldsymbol{a^2/_{12}}}{\boldsymbol{N_{signal}}} \cdot \left(\frac{\mathbf{16}}{\mathbf{9}} + \frac{\boldsymbol{8\pi\left(\sigma^2_{Gauss} + a^2/_{12}\right)\langle N_{background}\rangle^2}}{\boldsymbol{N_{signal} \cdot a^2}} \right) \quad \textbf{Eq. 32}$$

where σ^2_{Gauss} is the variance of the Gaussian structure to be localized and a is the pixel size (46).

LMS fitting has been implemented by exploiting the Matlab function *fminsearch*, where the Gaussian model has a variance equal to the simulated one while height, background and x-y position are free parameters. Centroid localization has been

implemented as an intensity-weighted center of mass, namely $x = \frac{\sum_{i=1}^{X}\sum_{j=1}^{Y}(i-x_0)\cdot I_{ij}}{\sum_{i=1}^{X}\sum_{j=1}^{Y} I_{ij}}$, for the x localization, where X and Y are the x and y dimensions of the mask, respectively, x_0 is the center of the mask and I_{ij} is the intensity at the pixel (i,j). Cross-correlation localization has been implemented by cross-correlating an image of a simulated centered Gaussian and the image to be localized; we applied a spline interpolation for oversampling the images 20 times and achieving sub-pixel localization; the position of the maximum of the cross-correlation function ultimately defines the structure position.

Figure 26 shows the characterization of the localization algorithm, note that PLICCS localization has no bias and constant precision in sub-pixel localization, unlike the centroid, which shows a position-dependent bias, and the cross-correlation, which shows a positive constant bias dependent on the oversampling factor used (data not shown).

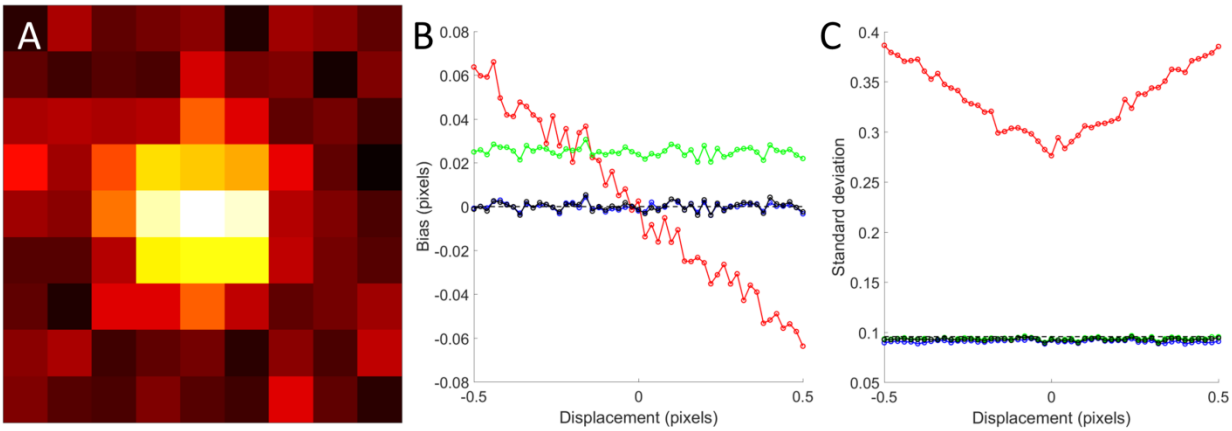

Figure 26: Example of simulated particle with SNR=22 (A), Bias (B) and precision (C) as a function of subpixel displacement for PLICCS (blue), centroid (red), cross-correlation (green) and LMS fitting (black). Black dotted lines represent bias=0 (B) and the theoretical limit for the localization precision (C). Points are calculated as an average of 5000 realizations.

Furthermore, the localization precision for PLICCS is equal to LMS localization, which in turn matches the theoretical limit. We also tested speed and noise stability as a function of the signal to noise ratio (***Figure 27***), showing that the execution time for PLICCS is the same regardless the noise level, not being an iterative approach, and the standard deviation as function of the SNR shows localization precision level matches the

theoretical limit, once again, over three orders of magnitude, it also performs better than cross-correlation for SNR<10.

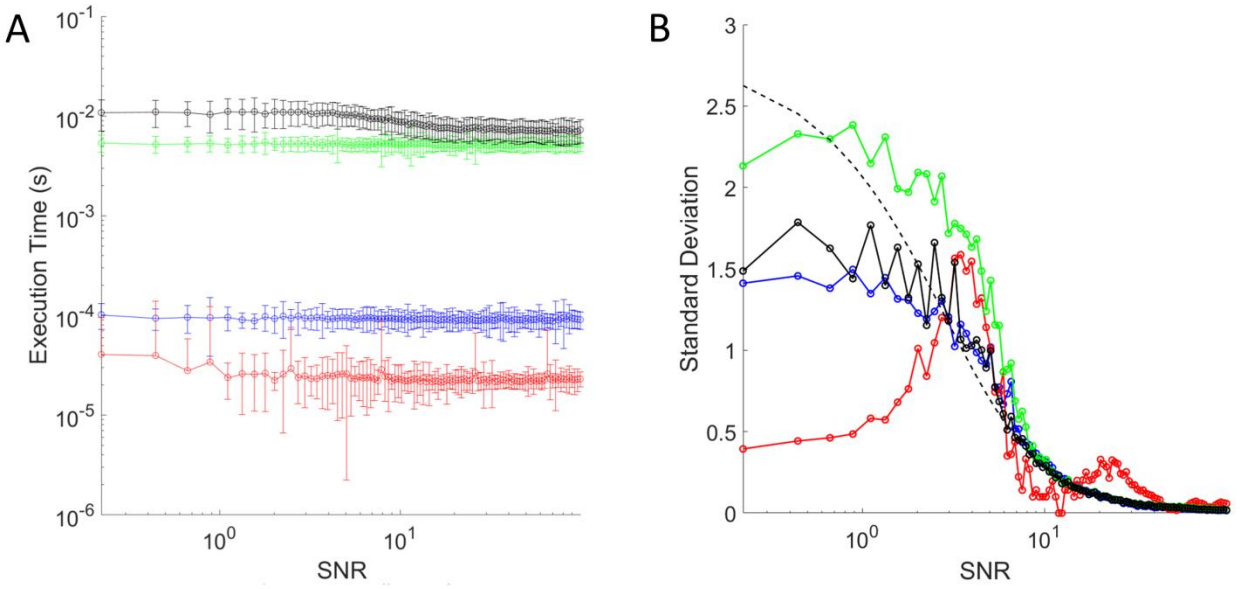

Figure 27: Execution time (A) and precision (B) as a function of the signal to noise ratio for PLICCS (blue), centroid (red), cross-correlation (green) and LMS fitting (black), black dotted line represents the theoretical limit for the localization precision. Points are calculated as an average of 100 realizations.

Average execution times per iterations (computed from ***Figure 27 A***) are $t_{PLICCS} = 88.4\ \mu s$, $t_{centroid} = 23.9\ \mu s$, $t_{cross-correlation} = 5200.6\ \mu s$ and $t_{LMS} = 8480.1\ \mu s$, therefore our approach allows for 10^4 localizations per second, two orders of magnitude faster than cross-correlation and LMS fitting with matching performances.

Characterization of a fast volumetric imaging system

A novel optical configuration recently developed enables single particle tracking with nanometric precision over a tunable axial range above 10 µm. The system is based on the simultaneous acquisition of two wide-field images of the specimen while electrically tunable lens (ETL) allows the position of the focal image plane to be changed across a large axial range within the exposure time of the camera detector. In practical terms, the ETL allows the acquisition of an image comparable to a sum of in-f.ocus planes over the scanned volume. This effect is usually referred to as extended depth of field or EDOF (47). Thus, the first acquired image in the current approach is formed after passing

through the optical axis of the ETL and, because of the EDOF effect, particles appear as bright spots across a long axial range (***Figure 28 A***). The second image uses a light pathway that is decentered with respect to the ETL optical axis, resulting in the same bright spot laterally shifted with respect to the first one for a parallax effect. Such a shift linearly depends on the z position of the particle and can be described by a parameter $C = \frac{p}{z - z_0}$, where p is the displacement in pixels, z is the absolute axial position and z_0 is the reference axial position. The localization in z is consequently possible by measuring the lateral distance between the spots of the two images; a schematic description of the principle is shown in ***Figure 28***

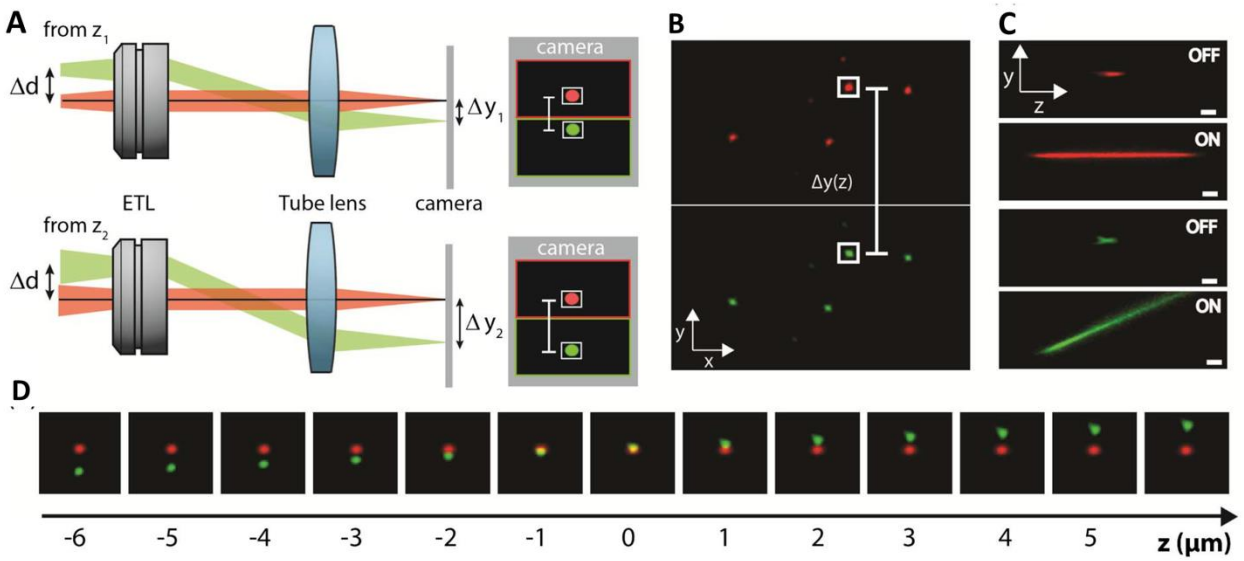

Figure 28: Schematic of the working principle of the tracking approach. (A) Red beams show the effect of the tunable lens in a standard on-axis image formation system. For an infinity corrected system, the focal length of an ETL placed in the conjugate plane of the detection objective can be varied to compensate for any degree of divergence for rays coming from focal planes at different z positions (bottom). This enables the formation of focused images at the camera sensor for particles located at different z positions, preventing the loss of out-of-focus tracking precision. By inserting an off-axis displacement of the ETL relative to the optical axis, the same holds (green beam). However, in this case, there is an additional steering effect that depends on the value of the ETL focal length needed to bring the image into focus. This produces an encoding of the axial position into a lateral shift. (B) Snapshot of a sample of fluorescent beads acquired with the tracking system. The false colors correspond to the aligned (red) and decentered (green) channels. (C) Experimental PSF for each channel with the ETL off (standard acquisition system) and ETL on. Scale bar is 2 µm. (D) Lateral shift induced in the green channel for a single bead as a function of the axial position. Note that the red channel does not move. Adapted from (48)

Ultimately, the optical system returns an image divided in two halves, the upper half hosts the non-shifted image while the lower one hosts the shifted image, exhaustive description of the experimental setup and technique can be found in (48). The algorithm goes through the following operations: at first, the image is divided in two separate images of the shifted and the non-shifted structures, then an image processing step is performed in order to enhance the two images, including a moving median removal for background correction and a Gaussian smoothing. Once the images are separated and processed, their cross-correlation function is computed and the two images are shifted of a number of pixel equal to the distance of the maximum of the cross-correlation function from the center. Note that this registration step aligns the structures correctly in the direction orthogonal to the direction of the shift, while in the direction of the shift they cannot be perfectly aligned due to the depth-dependent shift; this mismatch is not an issue since we don't need the absolute z-position for the dynamics but the relative change in position. At this point, structures are select by thresholding and the localization procedure goes through a x-y localization in the non-shifted channel as described previously, while the z localization is performed through PLICCS. Trajectories are defined as 3D localizations as a function of time and are constructed by defining a searching radius starting from the previous localization and assigning the closest localization of the next frame to the trajectory.

The system allows for the tuning of the localization precision in z by decreasing the effective depth range; in ***Figure 29*** are displayed two cases, a short range/high precision (red curves) as opposed to a long range/low precision case.

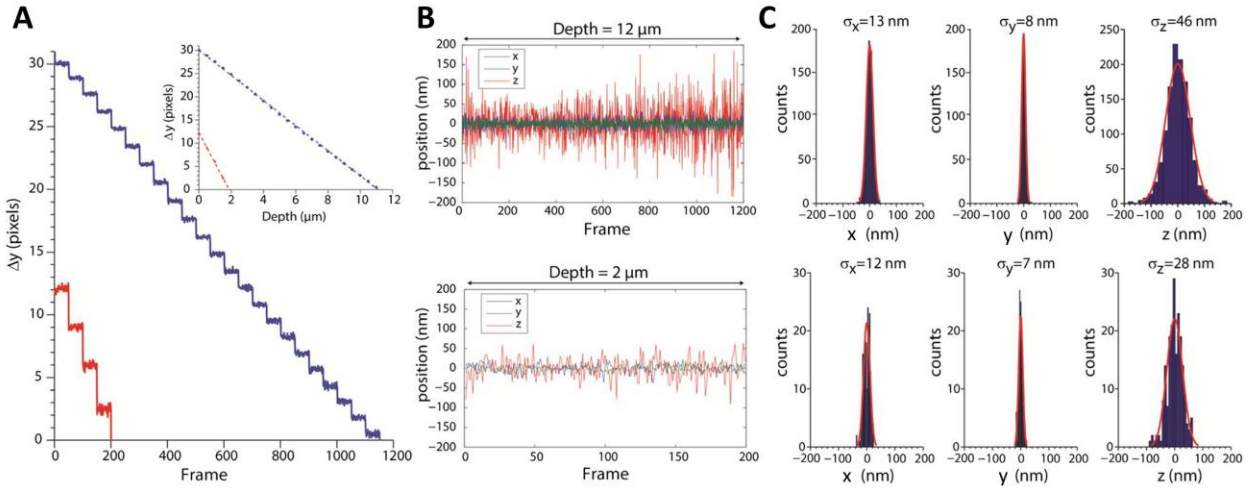

Figure 29: Characterization of the localization precision of the 3D tracking technique. (A) Lateral separation between the two channels (Δy), in pixels, for a 500 nm bead attached to a glass coverslip and translated in steps of 0.5 μm every 50 acquisitions. The experiment was repeated for two different settings: a value of C corresponding to 2.7 px/μm (blue line) for a total axial range of 12 μm and to 5.1 px/μm (red line) for an axial range of 2 μm. The inset shows the linear dependence of Δy as a function of the axial position for each case. (A) Plot of the x–y–z position of the tracked bead in (A) along the entire axial range for the two studied configurations. The values have been calculated relative to the average position in each axial plane. (C) Localization precision along the three directions of space extracted from (B). Adapted from (48)

The system can be tuned by simply changing the displacement of the two optical paths, going from a 12 μm range with 46 nm of precision to a 2 μm with 28 nm of precision, the conditions of acquisition are described in (48). The curves in ***Figure 29*** are constructed by localizing fluorescent beads adhering to a coverglass and then changing their z position in a controlled fashion through the microscope interface, in the graph are plotted the displacement as a function of the frame number, every step corresponds to a change in z of one micron.

MSD of beads and neuron receptors

For testing the system, we imaged a 500 nm fluorescent bead diffusing in solution and we tracked it in 3D as shown in ***Figure 30 A***, then we calculated the MSD (Mean Square Displacement) curve in order to compute its diffusion coefficient (49).

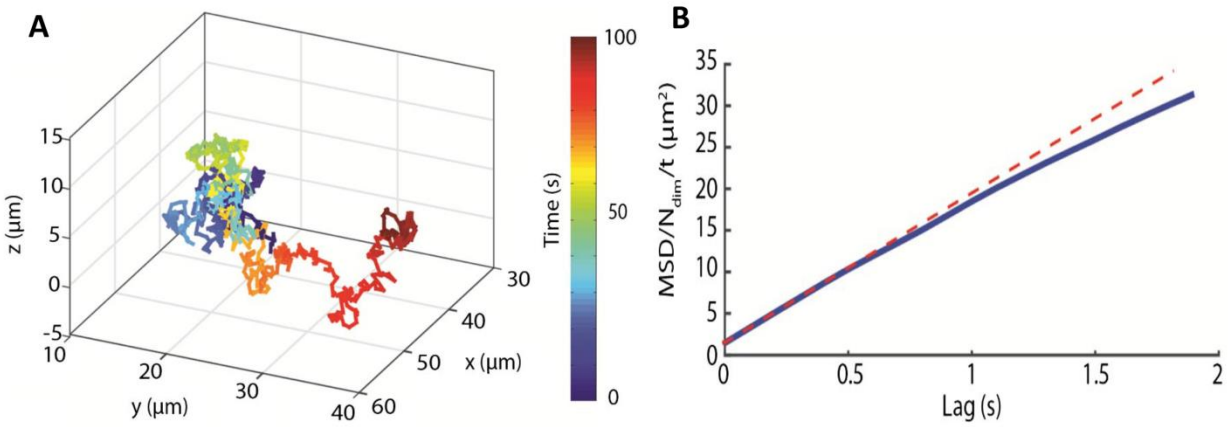

Figure 30: Measurement of the 3D free-diffusion coefficient of microspheres in water. (A) 3D trajectory of single fluorescent bead (500 nm size) tracked in water at room temperature. The 3D position of the fluorescent particle was measured every 0.1 s for 100 s. (B) Representative MSD plot (blue line) and fitting of the initial slope (red dashed line) for the freely diffusing particle shown in (A). Adapted from (48)

Assuming ΔT is the temporal step between two localization (the frame time), $MSD(\Delta t)$ is defined as the average of the square distance traveled by the particle from each point of trajectory in the time $\Delta T, 2\Delta T, \dots, n\Delta T$; according to the laws of diffusion, $MSD(\Delta t) = 2n_{dim}D\Delta t$, where n_{dim} is the dimensionality of the system (e.g. 2 for 2D diffusion), D is the diffusion coefficient and Δt is the lag time, therefore for free diffusion the $MSD(\Delta t)$ curve is linear and its slope is proportional to the diffusion coefficient. In the case of diffusing beads, a simple linear fitting can be used to calculate the diffusion coefficient (D) of the bead, which results in $D = 0.90 \pm 0.16$ μm^2/s; this value agrees well with that previously reported for beads of the same size in an aqueous media ($D = 0.875$ μm^2/s), confirming the validity of our technique (50).

Ultimately, we tested how the algorithm performs in a real sample by tracking a GABAA receptor, immunolabeled with a quantum dot, in a living neuron. An example of trajectory of one receptor is shown in two representations in ***Figure 31***.

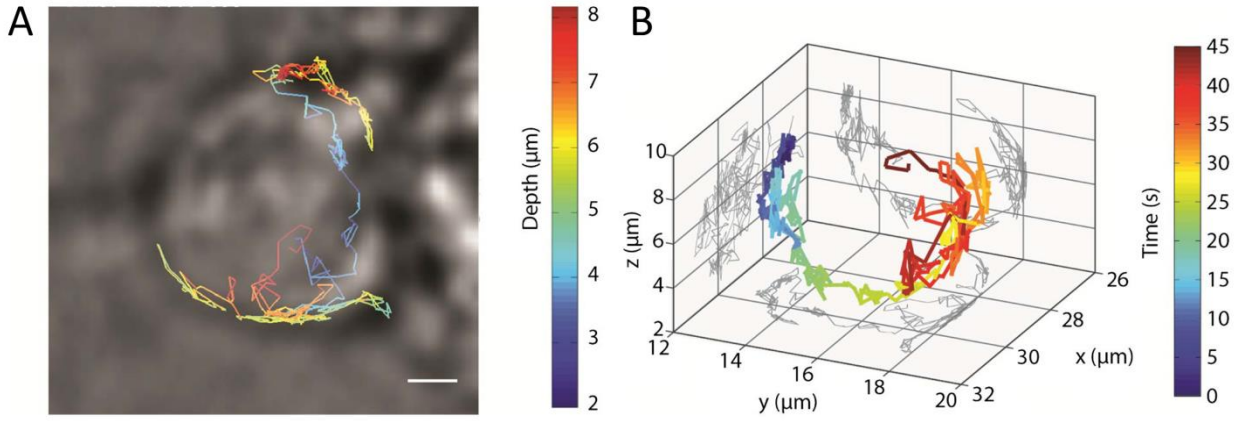

Figure 31: Diffusion of GABAA receptors in the membrane of living neurons.(A) Representative time-color-coded trajectory of an individual α1-containing GABAA receptor diffusing on a soma of a cultured hippocampal neuron. The trajectory tracking the QD fluorescence has been superimposed on the neuronal soma image acquired with transmitted light microscopy. Scale bar is 2 µm. (B) Same receptor trajectory shown in (A) rendered in three dimensions and shown on a time-coded scale. In ~45 seconds the receptor explores a considerable portion of the somatic region spanning ~4–6 microns in both the x–y and z axes. Adapted from (48)

CHAPTER 4 Local Raster Image Correlation Spectroscopy (L-RICS): High resolution intra-nuclear diffusion maps

Raster Image Correlation Spectroscopy (RICS) is a powerful method for measuring molecular diffusion in live cells directly from images acquired on a laser scanning microscope. However, RICS only provides single average diffusion coefficients from regions with a minimum lateral size of few micrometers, which means that its spatial resolution is mainly limited to the cellular level. Here we introduce the local RICS (L-RICS), an easy-to-use tool that generates high resolution maps of diffusion coefficients from images acquired on a laser scanning microscope.

4.1 Local RICS

Raster Image Correlation Spectroscopy

Raster Image Correlation Spectroscopy (RICS) is a technique derived from ICS, used for extracting the diffusion coefficient of a molecule from the spatial ACF of raster-scan images (***Figure 32***) by exploiting the fast scanning speed of confocal laser scanning microscopes (CLSM).

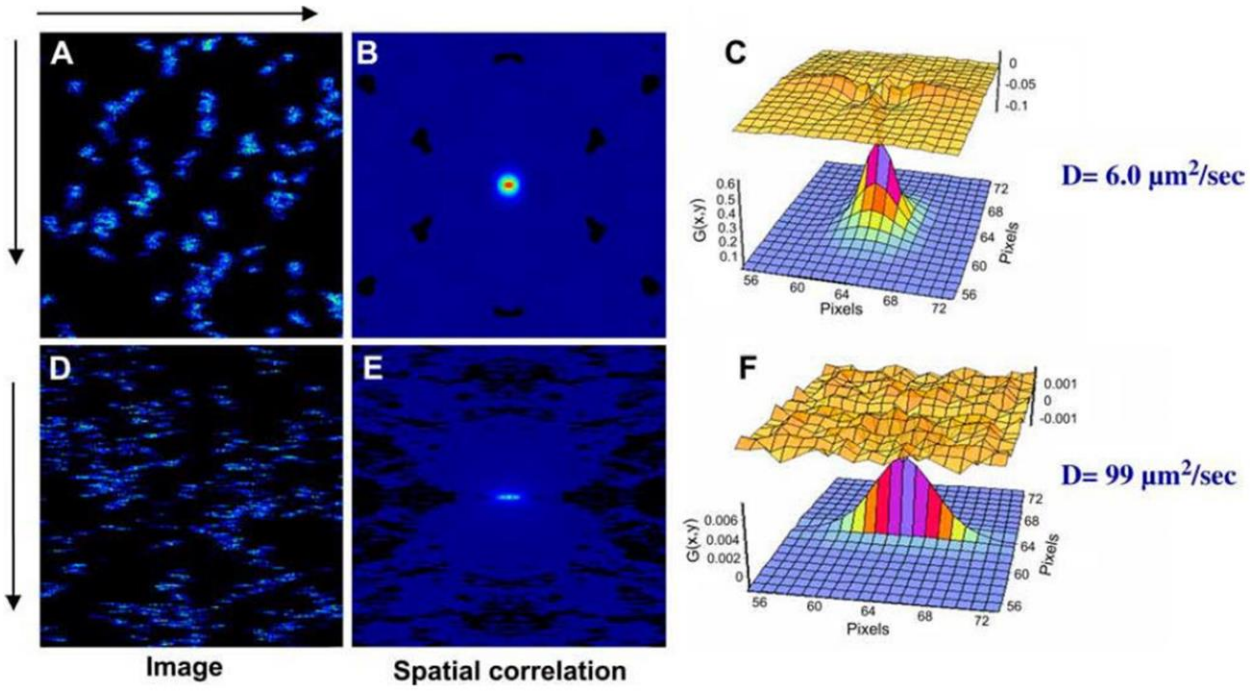

Figure 32: Simulated images of freely diffusing 10-nm beads (A) and EGFP (D) in a plane. The fast EGFP moving molecules appear as a streak in the image (D). B and E are the two-dimensional special correlation functions of the images A and D, respectively. C and F are the fit of the autocorrelation functions B and E. Image parameters: frame 256x256, 16 µs pixel dwell time, and 0.050 µm pixel size. Reproduced from (51)

Once the image is acquired (***Figure 32 A,D***), its ACF is computed (***Figure 32 B,E***) and it is fitted to a theoretical model in order to compute the diffusion coefficient of the probe.

RICS analysis consists in computing the spatial ACF of an image or a series of images acquired in a raster-scan mode:

$$G(\xi,\eta) = \frac{1}{N_{frames}} \sum_{k=1}^{N_{frames}} \left(\frac{\langle I_k(x,y) \cdot I_k(x+\xi, y+\eta) \rangle}{\langle I_k(x,y) \rangle^2} - 1 \right) \quad \textit{Eq. 33}$$

Since the raster-scan image contains spatial and temporal information, related to the diffusion of the probe and the microscope scanning speed, the spatial correlation of the image also contains spatial and temporal information.

The RICS ACF shape depends on two contributions:

$$G(\xi,\eta) = S(\xi,\eta) \cdot G_{diffusion}(\xi,\eta) \qquad \textit{Eq. 34}$$

Where is the spatial component of the correlation function related to the laser scanning and is defined as:

$$S(\xi,\eta) = exp\left(-\frac{\left(\frac{|\xi|\delta x}{w_0}\right)^2+\left(\frac{|\eta|\delta y}{w_0}\right)^2}{1+\frac{4D(\tau_p|\xi|+\tau_l|\eta|)}{w_0^2}}\right) \qquad \textit{Eq. 35}$$

where δx and δy are the pixel sizes along the x and y scanning directions, respectively, $\tau_p$is the pixel dwell time in x, τ_l is the interline time in y, w_0 is the waist of the point spread function of the microscope.

The second term is the temporal part related to the diffusion:

$$G_{diffusion}(\xi,\eta) = \frac{\gamma}{N}\left(1+\frac{4D(\tau_p|\xi|+\tau_l|\eta|)}{w_0^2}\right)^{-1} \cdot \left(1+\frac{4D(\tau_p|\xi|+\tau_l|\eta|)}{w_z^2}\right)^{-1/2} \qquad \textit{Eq. 36}$$

where γ is the shape factor due to the distribution of the illumination in the focal volume (for a 3D Gaussian illumination γ=0.35) and w_z is the waist along the z direction. Let's consider only one spatial dimension (for instance the x-axis), the theoretical formula for the RICS ACF is now written as:

$$G(\xi) = S(\xi) \cdot G_{diffusion}(\xi) \qquad \textit{Eq. 37}$$

where

$$S(\xi) = exp\left(-\frac{\left(\frac{|\xi|\delta x}{w_0}\right)^2}{1+\frac{4D(\tau|\xi|)}{w_0^2}}\right) \qquad \textit{Eq. 38}$$

and

$$G_{diffusion}(\xi) = \frac{\gamma}{N}\left(1 + \frac{4D(\tau|\xi|)}{w_0^2}\right)^{-1} \cdot \left(1 + \frac{4D(\tau|\xi|)}{w_z^2}\right)^{-1/2} \quad \textit{Eq. 39}$$

where now τ is the pixel dwell time along that direction.

We now apply the substitution with the *sampling constants*:

$$\begin{cases} K_s = \dfrac{\delta x}{w_0} \\ K_t = \dfrac{4D\tau}{w_0^2} \end{cases} \quad \textit{Eq. 40}$$

Here K_s represents the spatial sampling of the point spread function (PSF) and K_t represents the temporal sampling, namely the ratio between the pixel dwell time and the diffusion time of the diffusing probe. As a matter of fact, since the diffusion time τ_D is defined as $\tau_D = \frac{w_0^2}{4D}$, it results $K_t = \frac{\tau}{\tau_D}$. Now, the 1D ACF with both contributions can be written as:

$$G(\xi) = \frac{\gamma}{N} exp\left(-\frac{(|\xi|K_s)^2}{1+K_t}\right) \cdot (1 + K_t)^{-1} \cdot \left(1 + \frac{w_0^2}{w_z^2} K_t\right)^{-1/2} \quad \textit{Eq. 41}$$

By doing this, we have made every contribution relative to the acquisition parameters and the probe diffusion implicit in the sampling constants. It's worth noticing that, since w_z/w_0 is a constant that depends on the PSF of the microscope (typically w_z/w_0~3 for a confocal PSF), the shape of $G(\xi)$ depends only on the sampling constants K_s and K_t.

Algorithm and simulations

The algorithm described in ***CHAPTER 2*** has been adapted for retrieving the local diffusion coefficient from RICS datasets and is implemented in a pixel-wise fashion. For every pixel (*i*,*j*), we define a local ACF $G^{ij}_m(\xi,\eta)$:

$$G_m^{ij}(\xi,\eta) = \frac{1}{N}\sum_{k=1}^{N}\left(\frac{\frac{1}{m^2}\sum_x^m\sum_y^m I_k^{ij}(x,y) I_k^{ij}(x+\xi,y+\eta)}{\left(\frac{1}{m^2}\sum_x^m\sum_y^m I_k^{ij}(x,y)\right)^2} - 1\right) \quad \textit{Eq. 42}$$

Where N is the total number of frames and $I^{ij}_k(x,y)$ indicates a sub-image of size $m \times m$ centered on pixel (i,j), hereafter referred to as "L-RICS mask" or simply "mask". This local ACF can be very different from the global ACF calculated on the entire image (***Figure 33 A,B***) and cannot be described by the theoretical expression in ***Eq. 41***.

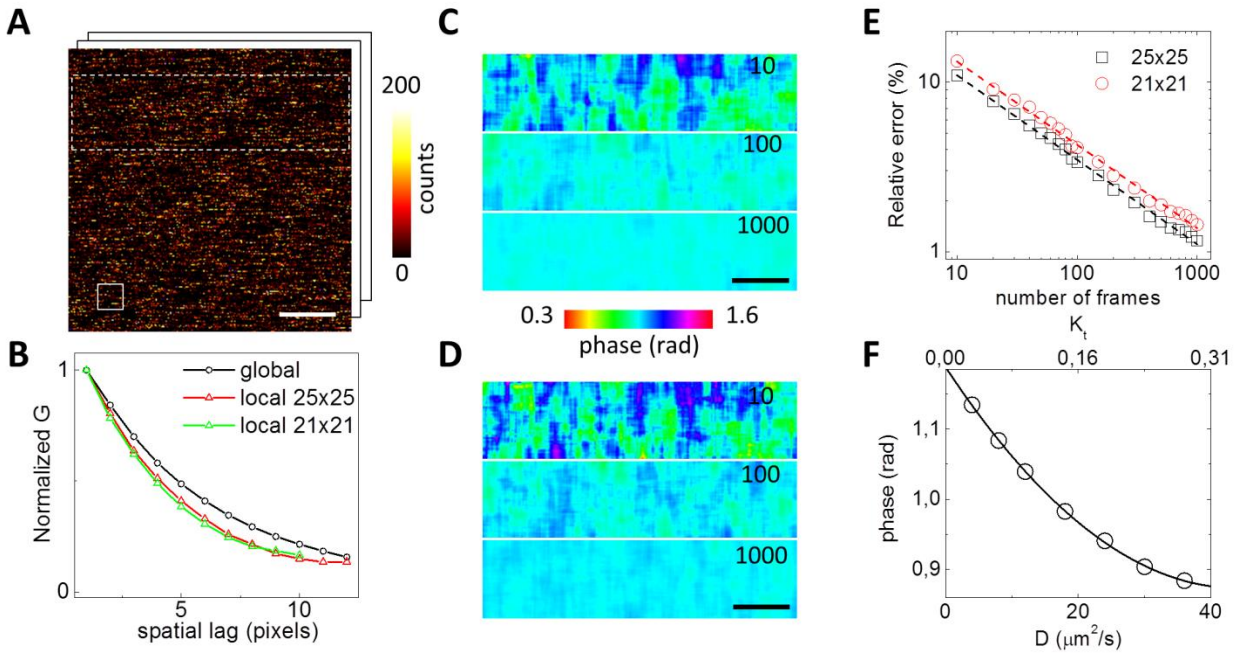

Figure 33: Phasor analysis of local RICS. (A) Example of one frame of a simulation with D=24 $\mu m^2\ s^{-1}$ and a molecular brightness of 24 kHz. The solid box shows the size of the 21×21 pixels mask. The white dashed box shows the region in which the analysis is performed. (B) Spatial ACF of the dataset shown in (A) computed on the whole image area (black circles) and on local masks of size 25×25 pixels (red) and 21×21 pixels (green) respectively. Phase maps obtained from analysis with L-RICS masks 25×25 pixels (C) and 21×21 pixels (D), respectively. The numbers indicate the number of frames used for the analysis. (E) Relative phase error (defined as the standard deviation shown as a percentage of the mean value) as a function of the number of frames for a 25×25 pixels mask (black squares) and a 21×21 pixels mask (red circles). The dashed lines are power-law fits to the data with exponent α=-0.50±0.01 and α=-0.49±0.01 respectively. (F) Calibration curve for the 25×25 pixels mask and for K_s=1/8 as a function of D and K_t. Scale bar is 1 μm

This deformation effect, due to the fact that fluctuations are sampled in a very short interval (33, 51, 52), results in a change in the shape of each local ACF which depends also on the size of the mask. In order to analyze the local ACFs from all the pixels, we

consider the 1D local ACF $G^{ij}_m(\xi)$ and use the phasor approach to calculate $g(i,j)$ and $s(i,j)$:

$$\begin{cases} g(i,j) = \dfrac{\int_0^L G_m^{ij}(\xi)\, cos\left(\frac{2\pi\xi}{L}\right) d\xi}{\int_0^L G_m^{ij}(\xi) d\xi} \\ s(i,j) = \dfrac{\int_0^L G_m^{ij}(\xi)\, sin\left(\frac{2\pi\xi}{L}\right) d\xi}{\int_0^L G_m^{ij}(\xi) d\xi} \end{cases} \qquad \textbf{Eq. 43}$$

and calculate the phase parameter $\phi(i,j)$, which encodes offset-independent information about the shape of the local ACFs (52). Here, L represents the number of points in which the function $G^{ij}_m(\xi)$ is sampled, for instance for an odd-sized mask of size m, $L=(m+1)/2$. As a result, for a given RICS dataset, we get a phase map that contains spatial information on the diffusion properties (***Figure 33 C,D***). Smaller phase values correspond to local ACFs which decay more rapidly to zero (faster diffusion), whereas larger phase values correspond to local ACFs which decay less rapidly to zero (slower diffusion).

The noise of this phase map depends on the size of the mask and on the number of frames used for averaging (***Figure 33 C-E***). As expected, the error on the phase parameter follows the same general trend derived for FCS (53, 54), i.e. $\sigma_\phi \propto 1/\sqrt{t_{acq}} \propto 1/\sqrt{N}$, where t_{acq} is the time needed to acquire N frames. For a given number of averaged frames, the error on the phase is larger for a smaller size of the mask (***Figure 33 C-E***). We calculated from simulations the number of frames required to reach a given precision in the determination of the phase. For instance, for the 21×21 pixels mask, at the conditions of the simulation (brightness~24kHz), we can see that the error on the phase decreases from ~15% to ~4% by increasing the number of frames from 10 to 100. These numbers can be used to estimate the expected error in the phase for a given experiment, provided that the brightness and the acquisition parameters set for the simulation match those of the actual experiment.

Finally, in order to convert the phase map into a map of diffusion coefficients, we built a series of calibration functions, based on simulated data, for different values of K_s, K_t and

m. Indeed, for a given value of K_s and for a given value of *m*, we obtain a well-defined relationship between the phase ϕ and K_t (***Figure 33 F***). Provided that the dwell time is known, this relationship can be used directly to convert a value of phase ϕ into a value of diffusion coefficient *D* (***Figure 33 F***).

Spatial heterogeneity

As a controlled example of data with heterogeneous diffusion properties, we simulated a RICS acquisition on a sample consisting of three regions characterized by different diffusion coefficients (D_1=12, D_2=18 and D_3=24 μm^2 s^{-1}, respectively, ***Figure 34 A,B***).

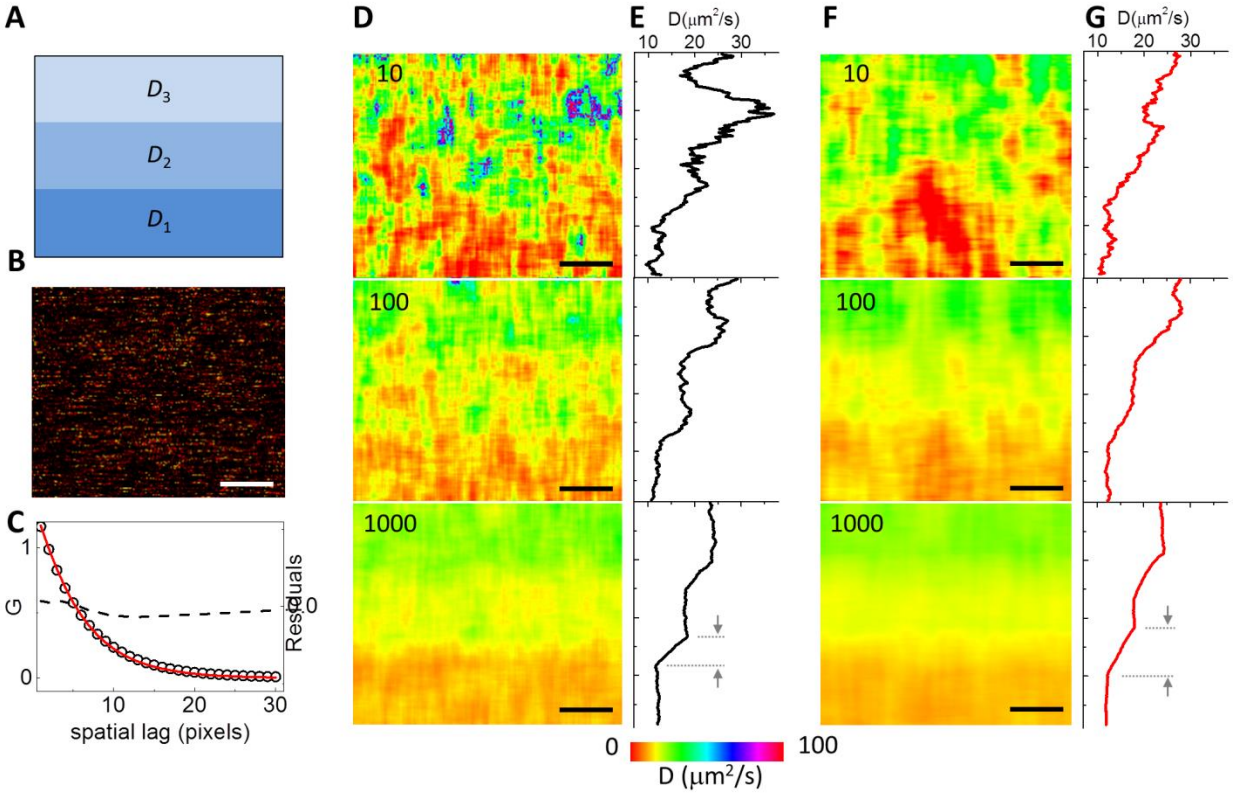

Figure 34: Simulations of heterogeneous diffusion zones. a Scheme of the diffusion coefficient distribution of the simulated dataset. The values of diffusion coefficient within each zone are D_1=12, D_2=18 and D_3=24 μm^{2}s^{-1} respectively. b Single intensity frame after time average removal. c X-axis ACF computed from the dataset (black circles) along with single component fitting (solid red line) and residuals (black dashed line). d L-RICS diffusion maps computed with a 25×25 pixels mask and averaging over a different number of frames. e Line profiles obtained averaging each map along the x-axis. f L-RICS diffusion maps computed with a 41×41 pixels mask and averaging over a different number of frames. g Line profiles obtained averaging each map along the x-axis. The numbers indicate the number of frames used for the analysis. Scale bar is 1 μm.

We computed the spatial ACF of the entire dataset and we tried to fit the resulting function with a single component formula (***Figure 34 C***) along the *x*-axis. We notice that the fitting yields a satisfactory result already with a single component model (D=16.8 $\mu m^2\ s^{-1}$ ***Figure 34 C***) meaning that, without a priori knowledge of the sample, it is difficult to separate the three diffusion components. Moreover, the global ACF does not convey any information about their spatial distribution. Instead, when we apply L-RICS to the same dataset (***Figure 34 D-G***) we are able to characterize the heterogeneity of the system. Provided the statistics are robust enough, we are able to discriminate between these diffusion behaviors and we can speculate on their spatial distribution.

The spatial resolution of the diffusion map is given by the size of the mask. Comparing ***Figure 34 D*** (25×25 pixels mask) and ***Figure 34 E*** (41×41 pixels mask) we can observe that in the first case we obtain a higher spatial resolution (25×δx=500nm) but we need to average over a larger number of frames, while in the second case the spatial resolution is lower (41×δx=820nm) but we need considerably fewer images to reduce the noise in the diffusion map. The difference in spatial resolution can be appreciated by looking at the average *y*-axis profile at the edges of the diffusion zones (***Figure 34 E,G***). Notably, given that the method is entirely computational, the analysis of a given dataset can be tuned, by changing the size of the mask, in such a way to reduce the noise of the map or to increase its spatial resolution.

Sample preparation and experimental setup

Samples

For the measurement of a dye in solution, a goat anti-mouse antibody coupled with Alexa 488 (Life Technologies) was diluted to a concentration of 20 µg/ml in PBS. A stable HeLa cell line expressing the protein AcGFP1 (ClonTech) was used for all the experiments (55). The day before the experiment, freshly split cells were plated on LabTek or Ibidi 8-well chamber (glass bottom, thickness 170±5 µm) and let them grow overnight.Transfection with EBFP2-Fibrillarin-7 (gift from Michael Davidson, Addgene plasmid # 55241) was performed with Lipofectamine 2000 (Thermofisher Scientific) following manufacturer instructions.

The brightness of AcGFP1 at different laser powers was measured using an aqueous solution of purified AcGFP1 (Clontech), prepared by diluting the protein in PBS (phosphate-buffered saline 1×, Thermo Fisher Scientific) at a final concentration of ~100 nM. The brightness of AcGFP1 was calculated from single point FCS measurements as $B=\langle I\rangle/\langle N_{mol}\rangle$, where $\langle I\rangle$ is the average intensity and $\langle N_{mol}\rangle$ is the average number of particles in the confocal volume.

Microscopes and experiments

The samples were imaged by a custom confocal microscope or by a Leica SP5 STED confocal microscope, both equipped with Leica 1.40 NA 100x objectives (HCX PL APO 100x 1.40/0.70 Oil, Leica Microsystems).

The custom microscope was obtained as a modification of a previous setup(5). Briefly, the excitation at 485nm was provided by a picosecond (< 100 ps) pulsed (80MHz) laser diode (LDH-D-C-485 Sepia, PicoQuant). Excitation at 405nm was provided by a CW laser diode (Cube 405, Coherent). The two beams were combined using two dichroic mirrors, then deflected by two galvanometric scanning mirrors (6215HM40B, CTI-Cambridge) and directed toward the objective by the same set of scan and tube lenses as the ones used in a commercial scanning microscope (Leica TCS SP5, Leica Microsystems). The fluorescence light was collected by the same objective lens, de-scanned, passed through the dichroic mirrors, then separated in two channels (525/50 nm and 445/45) before being focused (focal length 60 mm, AC254-060-AML,Thorlabs) into fiber pigtailed single-photon avalanche diodes (PDM Series, Micro Photon Devices). All imaging operations were automated and managed by the software Imspector (Max Planck Innovation). For single-point FCS, photons were detected by a TCSPC (Time Correlated Single Photon Counting) card (SPC-830, Becker & Hickl), synchronized with the reference signal provided by the pulsed diode laser. The power of the laser beam was always measured before entering the objective. Due to losses in the objective lens, the power at the sample is actually lower by 15%.

For FCS measurements, 10 datasets with 30 s acquisition time were acquired at a laser power of 9 µW. The raw data were processed for afterpulse removal using a custom fluorescence lifetime correlation spectroscopy (FLCS) algorithm (56).

A priori error determination and resolution

In order to test the algorithm on real microscopy data, we performed a RICS acquisition on a solution of an Alexa488-labeled antibody (***Figure 35***).

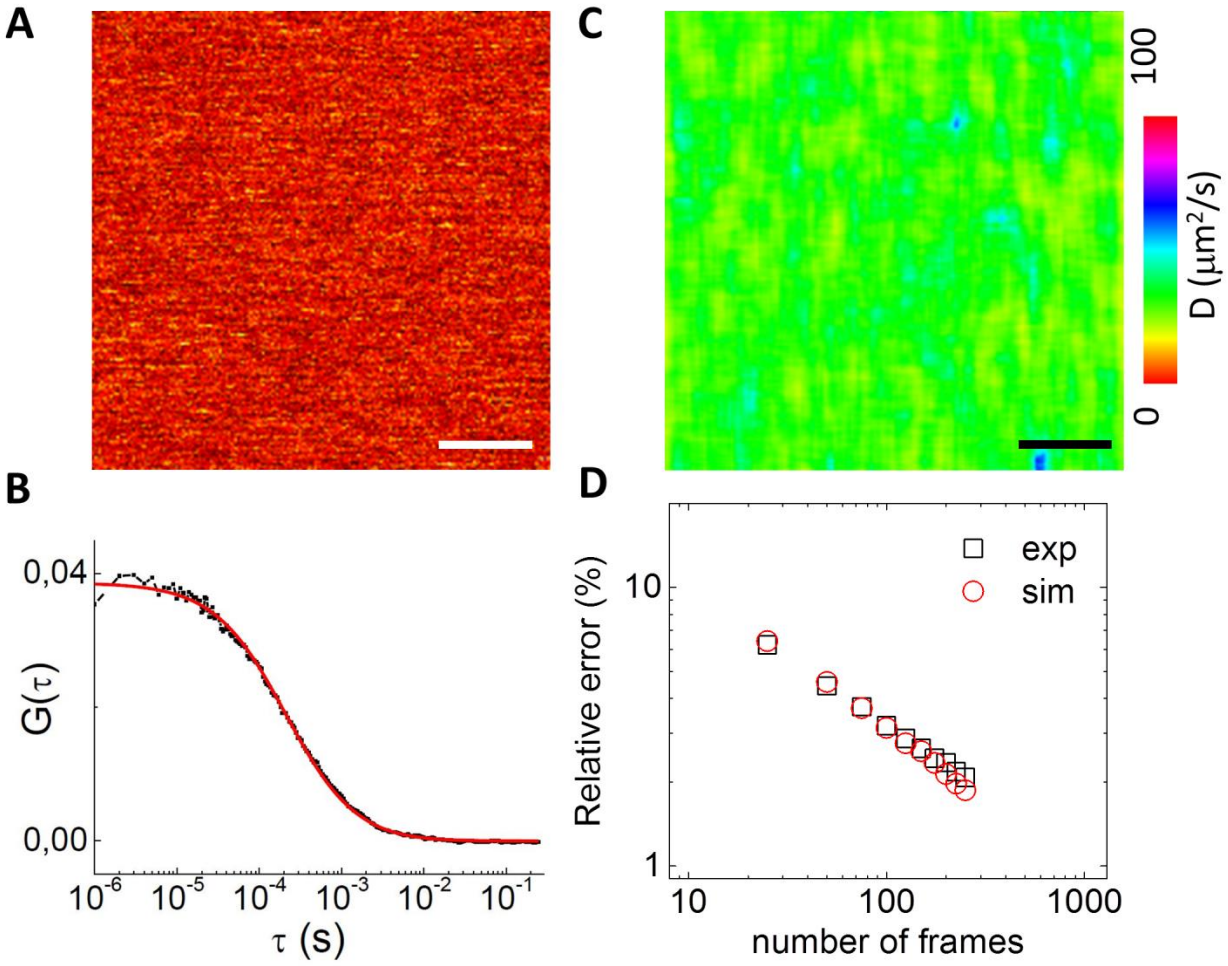

Figure 35: L-RICS of a dye in solution. (A) Example of one frame of acquisition of an Alexa488-labeled antibody in solution. (B) Example of a single-point FCS autocorrelation curve (black) and its fit (red). (V) Diffusion map computed with 250 frames. Comparison (D) of simulated (red circles) and experimental (black squares) values of relative error as a function of the number of frames used for averaging. Scale bar is 1 μm.

We set the laser power to 7.2 μW entering the objective in such a way to get an apparent brightness value around 24 kHz. The sample diffusion coefficient was measured by single-point FCS (***Figure 35 B***), yielding a value D_{FCS}=30.6 ± 1.6 μm^2 s^{-1} (*n*=10). The same value was obtained by global RICS analysis (data not shown) D_{RICS}=30.3 ± 1.1 μm^2 s^{-1} (*n*=10, 250 frames). An example of L-RICS diffusion maps

obtained with 250 frames is shown in ***Figure 35 C***. The average value of *D* obtained from this analysis is $D_{\text{L-RICS}}$=30.8 ± 2.7 μm^2 s^{-1} (n=1, *m*=25, 250 frames) in keeping with both the result from single-point FCS and the standard RICS analysis on the same dataset. For the conditions of this experiment a map with low noise can be obtained with *m*=25 pixels (corresponding to a spatial resolution of 25×δx=500nm) and *N*=250 frames.

This experimental dataset was compared with a simulated dataset with D_{sim}=30 μm^2 s^{-1} with the same brightness and acquisition parameters and their relative phase error was plotted as a function of the number of frames (***Figure 35 D***), showing that both the trend and the values for the experiment match with the ones expected from the simulations, therefore validating the use of simulations as a calibration method and for estimating the error in the measurements.

4.2 L-RICS: Intranuclear diffusion

Results: Intranuclear dynamics heterogeneity

We then applied the L-RICS method to obtain diffusion maps of GFP within the nuclei of HeLa cells (***Figure 36***). As a benchmark for the method, we tried to distinguish the different diffusion properties of GFP in the nucleoplasm and the nucleolus.

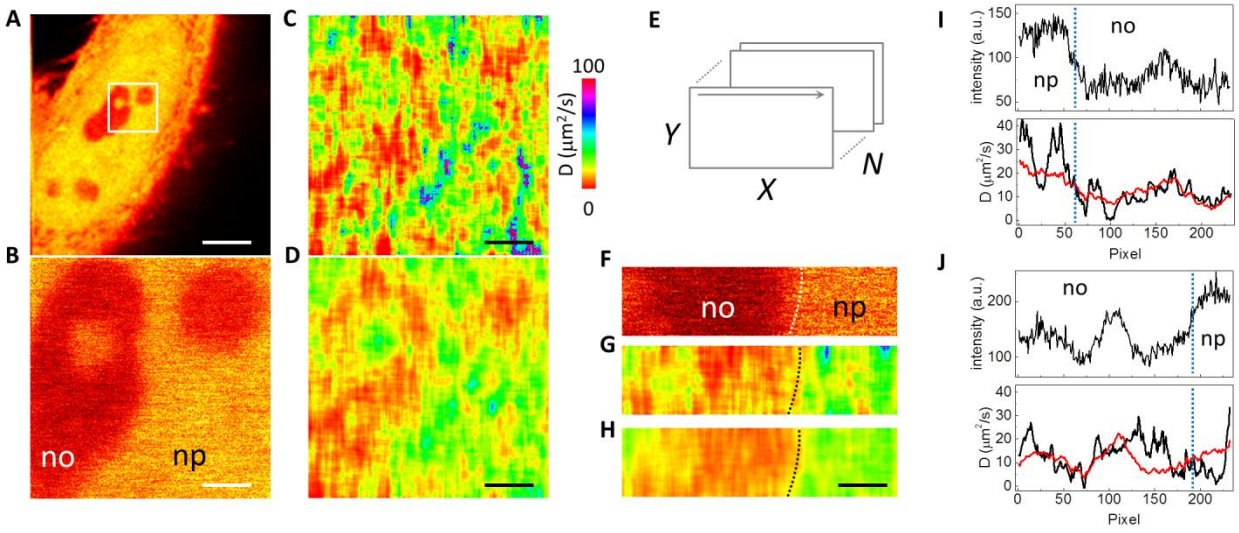

Figure 36: Diffusion maps of GFP in the nucleus. (A) Example of a HeLa cell expressing untagged GFP. (B) Enlarged region showing the 256×256 pixels area in which L-RICS was performed. Visible are portions of the nucleolus (no) and the nucleoplasm (np). (C,D) Diffusion maps computed with 25 (C) and 100 frames (D), corresponding to acquisition times of 1.37 and

5.46 min, respectively. (E) Schematic of the acquisition stack with dimensions X×Y×N. (F) Example of one frame of a L-RICS dataset of dimension 64×256 pixels. (G,H) Diffusion maps obtained from (F) and computed with 100 (G) and 400 (H) frames, corresponding to 1.37 min and 5.46 min total acquisition time, respectively. (I,J) Examples of line maps at the nucleolus/nucleoplasm interface. Shown are the intensity profile (I,J, top) and corresponding diffusion profiles (I,J, bottom). The diffusion profiles have been computed averaging over 1000 (black line) and 10000 (red line) lines, corresponding to an acquisition time of 0.21 and 2.13 min, respectively. Scale bar in (A) is 5 μm. Scale bar in (B-D,F-H) is 1 μm.

To this aim, we performed the experiments in regions at the nucleolus/nucleoplasm interface, easily recognizable by the gradient in concentration of the probe in the two compartments (***Figure 36 A,B***). The laser power was set at 25 μW entering the objective so that the brightness of GFP was about 24 kHz. The pixel size was set to δx=20nm and the L-RICS mask size was set to m=25 pixels so to obtain a spatial resolution of 500nm. The diffusion maps obtained with 25 and 100 frames are shown in ***Figure 36 C*** and ***D*** respectively. Since with the used acquisition parameters (τ=50 μs, 256×256 pixels) the time needed to acquire a single frame was t_{frame}=3.27 s, ***Figure 36 D*** shows that an acquisition time t_{acq}=100 × 3.27s=5.46 min is sufficient to get an intranuclear diffusion map over an area of 5.12×5.12 μm^2 and a signal-to-noise ratio sufficient to distinguish the different diffusion behavior of GFP in the nucleoplasm and the nucleolus. The observed values of diffusion coefficient in the two compartments are in keeping with previous reports (12). Moreover, the values of diffusion coefficients in the L-RICS map are comparable with the values of D obtained by performing single-point FCS measurements at various locations on the very same area and extracted by fitting the data to a model of a single diffusion component. In contrast, conventional RICS analysis performed on the whole image area does not retrieve the correct values of diffusion coefficients for the two compartments (***Figure 37-D***) and RICS analysis performed on a small region results in an overestimation of the diffusion coefficient (***Figure 36 E-H***).

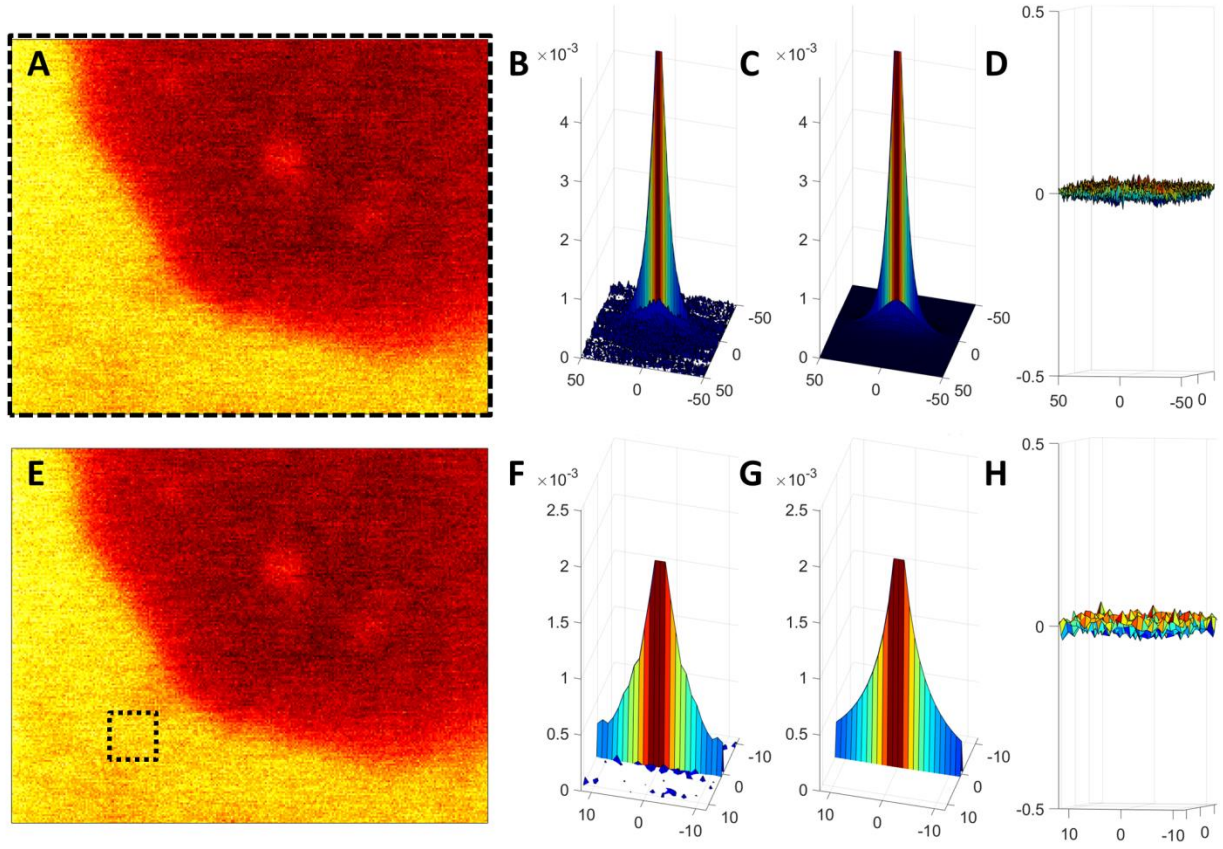

Figure 37: Example of one frame of a 100 frames acquisition of EGFP diffusing at the nucleolus-nucleoplasm interface (A,E). Global ACF (B), two components fitting (C) and residuals (D) from the entire region, fitting yields $D_1 = 21.13\ \mu m^2/s$ *and* $D_2 = 1.48\ \mu m^2/s$*. Local ACF (F) computed form the highlighted region in E, one component fitting (G) and residuals (H), the fitting yields* $D = 39.50\ \mu m^2/s$*.*

It is worth noting that the total acquisition time t_{acq} is dependent mainly on the pixel dwell time τ and total number of acquired pixels. For N frames of $X \times Y$ pixels the acquisition time is $t_{acq} \sim XYN\tau$ (***Figure 36 E***), assuming that line and frame retracing times are negligible. Therefore, by keeping the product XYN constant, it is possible to further reduce the noise on the map (increasing N) at the cost of decreasing the area of acquisition, without increasing the total acquisition time.

For instance, if we decrease the size of the ROI to a 64×256 pixels region (***Figure 36 F***) we need just a fourth of the time for acquiring a diffusion map with comparable noise level and, in the same 5.46 minutes, we can obtain a 400 frames diffusion map in which we can more clearly distinguish the nuclear and nucleolar diffusion and have a grasp of

the sub-nucleolar heterogeneity. Pushing this methodology to its limit, we acquired single lines inside the nucleolus itself (***Figure 36 G,H***) with very high statistics in a short acquisition time, namely 0.21 and 2.13 minutes for acquiring 1000 and 10000 lines, respectively. These line maps have better signal-to-noise ratio and can be used, in principle, to investigate the heterogeneity of diffusion within the nucleolar environment with high spatial resolution.

Results: Diffusion mapping in the nucleolus

We performed L-RICS of line scans across nucleoli of HeLa cells co-expressing GFP and Fibrillarin-BFP2 in order to reveal small differences in the diffusion coefficient of GFP that could be associated to the inner structure of the nucleolus. Based on electron microscopy studies (57), the nucleolus can be subdivided in three regions: the granular component (GC), which occupies the majority of the nucleolus, and the fibrillar centers (FC) surrounded by the dense fibrillar component (DFC). Fibrillarin is a protein present in the DFC and can be used as a marker to distinguish the GC from the FC/DFC regions. However, given that the FC/DFC regions below 200 nm in size, it is not possible to resolve their inner structure, at least in confocal microscopy.

Representative examples of these measurements are reported on ***Figure 38***. As we can see (***Figure 38 A,B***), within the nucleolus there may be present regions in which the structure is less compacted (red arrows), resulting in a higher diffusion coefficient.

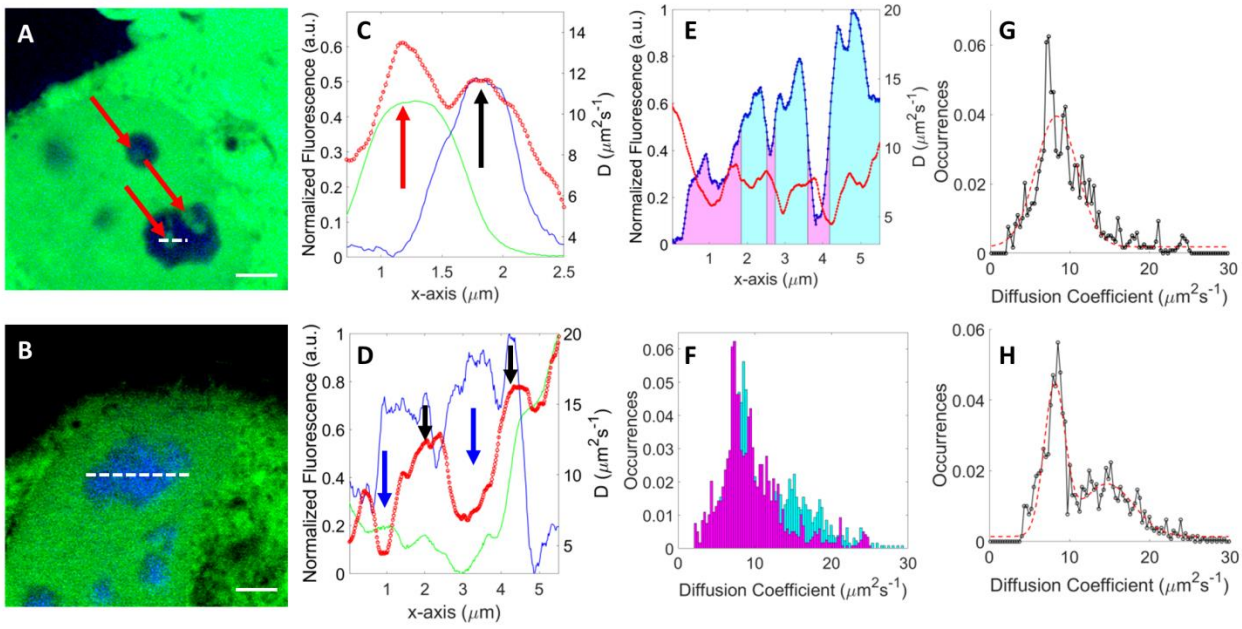

Figure 38: Diffusion maps in the nucleolus. Representative two colors images (A,B) of HeLa cells expressing untagged GFP (green) and Fibrillarin-BFP2 (blue). Red arrows indicate nucleolar vacuoles. The dashed white lines indicate the regions within the nucleolus in which line scanning was performed. Line maps (C,D) obtained from the acquisition indicated in (A,B). The plots show the normalized intensity profiles of GFP (green) and Fibrillarin (blue) together with the diffusion profile computed with L-RICS (red circles). Black arrows indicate regions with high intensity of Fibrillarin corresponding to a high diffusion coefficient of GFP. Blue arrows indicate regions with high intensity of Fibrillarin corresponding to a low diffusion coefficient of GFP. (E) Segmentation of data in a L-RICS line map (red circles), based on the level of normalized intensity I_{FIBR} in the Fibrillarin channel (blue dots). Magenta and cyan areas correspond to $I_{FIBR}<0.5$ and $I_{FIBR}>0.5$, respectively. (F) Cumulative histograms (n=15 cells) of the diffusion coefficient relative to the pixels with $I_{FIBR}<0.5$ (magenta) and $I_{FIBR}>0.5$ (cyan). Fitting of the histograms relative to $I_{FIBR}<0.5$ (G) and $I_{FIBR}>0.5$ (H) with a single (G) and double (H) Gaussian distribution, respectively. Shown are the experimental data (black circles) and the fit (red dashed line). Data were obtained from measurements on n=15 different cells. Scale bar in (A) is 2.5 μm.

These regions are characterized by a GFP signal comparable to that in the nucleoplasm and do not co-localize with the FC/DFC regions and may be associated with nucleolar vacuoles (58, 59). Interestingly, the FC/DFC regions show a very diverse behavior when we consider their diffusion profile; for instance, we notice that they exhibit diffusion coefficients spanning over a relatively wide range, namely from less than 5 $\mu m^2 s^{-1}$ (***Figure 38 D,F***, blue arrows) up to more than 16 $\mu m^2 s^{-1}$ (***Figure 38 B,D*** and ***F***, black arrows).

In order to evaluate the spatial heterogeneity observed in the Fibrillarin signal, we segmented the diffusion maps into two groups, one containing the pixels with a high normalized Fibrillarin signal (I_{FIBR}>0.5) and one containing the pixels with a low normalized Fibrillarin signal (I_{FIBR}<0.5), as shown in ***Figure 38 E***. From the analysis of a total of *n*=15 cells, we computed the histograms corresponding to the two groups that show clearly a different distribution of diffusion coefficients (***Figure 38 F-H***). In particular, we find that the pixels co-localized with the Fibrillarin signal are better described by two distinct populations of diffusion coefficient values, namely one at $D_1 = 8 \pm 1$ μm^2 s^{-1} and one at $D_2 = 15 \pm 3$ μm^2 s^{-}1. The FC/DFC regions have been linked to specific functions of the nucleolar machinery, specifically they are known to generate and accumulate transcripts within the nucleolus before their migration to the GC (57); therefore, this difference may be due to different degrees of structural compaction that can be related to an enhanced or reduced activity for these processes, although further studies are needed to test this hypothesis.

Results: Scanning speed inhomogeneities detection and correction

Pixel dwell time is a key parameter for the correct fitting of the ACF using RICS and, in the commonly used state-of-the-art formulation, it is required to be constant within the region RICS is applied. This may not be true in the case of non-linear scanning systems, i.e. setups in which the scanning speed varies during the acquisition. For this reason, in the commercial systems relying on non-linear scanning, the applicability of RICS has been partly limited.

Notably, L-RICS is a local approach and only requires the scanning speed to be approximately constant over regions as small as the mask used for the analysis. Thus the method is not limited to linear scanning systems and can be used to characterize the changes of the pixel dwell time, exploiting them for correcting the diffusion map.

In order to test the method on data acquired using non-linear scanning, we performed experiments on a Leica SP5 microscope using 100 Hz of line-sampling frequency and we acquired 300 frames with 80% laser power (White Light Laser at 488 nm, corresponding to about 20 μW entering the objective) and δx=20 nm. We imaged a

Alexa488-labeled antibody diffusing in solution (***Figure 39 A***) and computed the phase map (***Figure 39 B***) from which we can clearly observe a gradient of scanning speed.

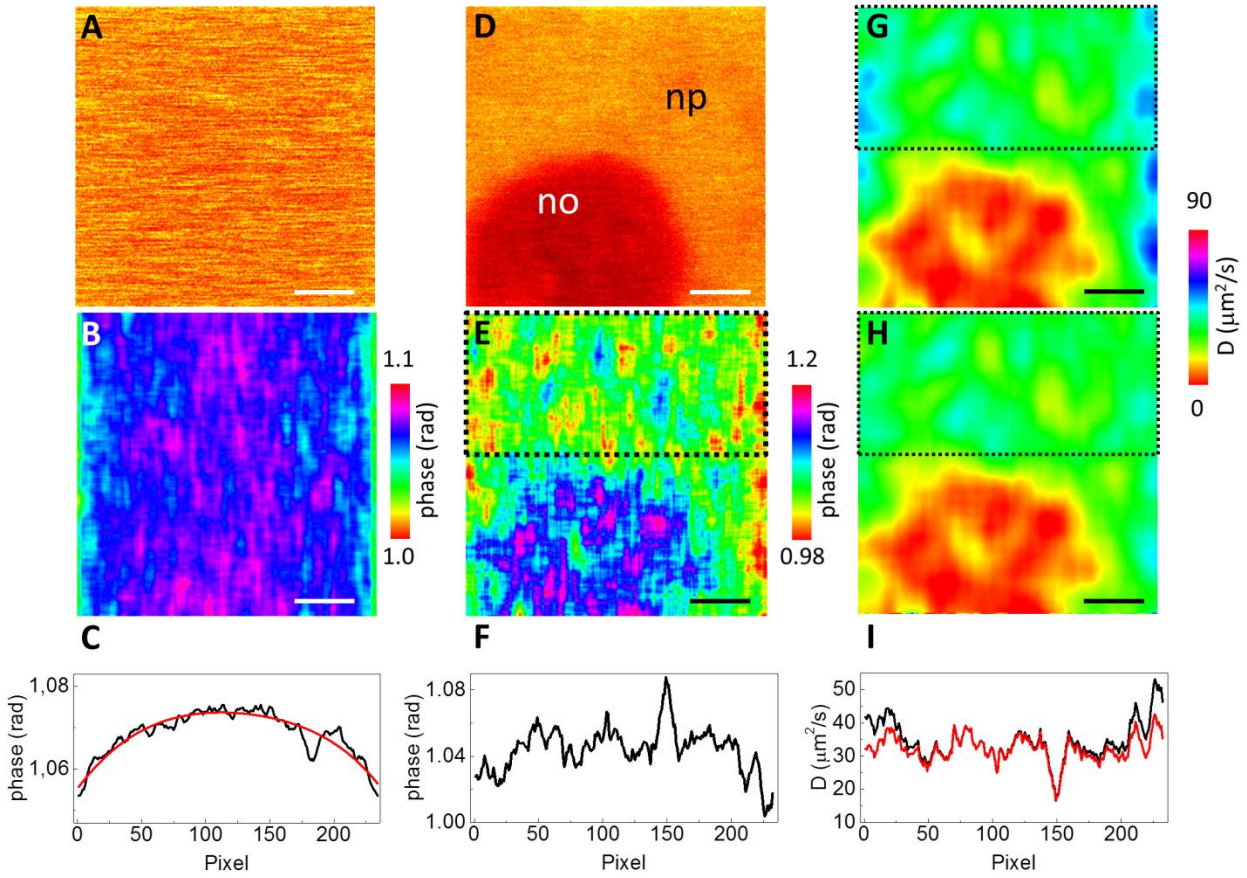

Figure 39: L-RICS on a non-linear scanning setup. a,b Single intensity frame (a) and phase map (b) of a solution of Alexa488-labeled antibody acquired on a non-linear scanning setup. c Line profile obtained averaging the phase map along the y-axis. The red line is a polynomial interpolation of the data. d,e Single frame (d) and phase map (e) of GFP diffusing at the nucleoplasm/nucleolus interface of a HeLa cell. f Line profile obtained averaging the phase map of a nucleoplasm region (black dotted box in e) along the y-axis. g Uncorrected diffusion map. h Diffusion map corrected for the non-linearity of the scanner. i Line profiles obtained averaging the uncorrected (black line) and corrected (red line) diffusion map of a nucleoplasm region (black dotted box in g and h). Scale bar in (a) is 1 μm.

Since the heterogeneity is present only along the x direction, we averaged the map along y in order to obtain a more statistically robust profile, and interpolated it with a polynomial function (***Figure 39 C***). By scaling this profile to our calibration function (***Figure 39 F***), we could retrieve a distribution of the K_t parameter along the x-axis that, in turn, can be scaled to a distribution of dwell times by knowing the diffusion coefficient

of the probe (D=30.6 μm^2 s^{-1}). We found that, with those acquisition parameters, the dwell time along the x-scanning direction varied from 12 to 18 μs. For the sake of clarity, it's worth noting that the 'dwell-time' τ that we are measuring here by L-RICS is the time lag between two consecutive pixels of a line, i.e. $\tau=\delta x/v$ where v is the speed of the scanner, and not the time spent to integrate the signal at each pixel. In fact, the intensity image is not affected by the dwell-time variations (***Figure 39 A***).

After characterization of the inhomogeneity of the scanning system, we tested if the method was able to produce, after proper correction, diffusion maps similar to those obtained on a linear scanning setup. To this aim, we performed acquisitions at the nucleolus/nucleoplasm interface of HeLa cells expressing GFP (***Figure 39*** D) and computed the phase map obtained by L-RICS analysis on 300 frames (***Figure 39*** E). This phase map encodes variations of the local correlation functions due not only to the value of the diffusion coefficient (for instance between nucleoplasm and nucleolus) but also to the value of pixel dwell time. Indeed, the phase map is deformed toward lower values at the borders of the image due to the slower scanning speed, as visible from the phase profile averaged over a nucleoplasm region (***Figure 39 E,F***). As a result, the diffusion map computed using a constant pixel dwell time (***Figure 39 G***) is biased at the borders toward higher values of diffusion coefficients (+10 to +15 μm^2 s^{-1}). Conversely, when we compute the diffusion map using the dwell time gradient obtained from previous calibration (***Figure 39 C***), we get a corrected map that shows no bias at the borders (***Figure 39 H,I***).

CHAPTER 5 Coupling super-resolution and correlation techniques

Diffusion in the cellular environment is not cannot always be described by free diffusion. Indeed, probes or proteins can exhibit a variety of diffusion modalities, for instance binding, diffusion in and out of micro-domains, diffusion in a meshwork-like environment, direct flow and super-diffusion. It is not easy to discriminate between this plethora of modalities with ICS and FCS alone without heavy assumptions on the nature of the environment, which is usually unknown. Advanced correlation techniques take advantage of non-conventional acquisition modes as well as more general theoretical frameworks in order to overcome these limitation and quantify non-Brownian diffusion.

Furthermore, these diffusion modalities can be confined to sub-diffraction volumes, therefore a super-resolution approach is needed in order to reduce the spatial heterogeneity of the system. As a result, many techniques were developed in recent years by coupling super-resolution techniques (typically STED) to correlation techniques like FCS and RICS (56, 60-67).

In the following chapter, we will present advanced correlation methods for the assessment and quantitation of non-Brownian dynamics and their coupling with super-resolution techniques.

5.1 Advanced spatio-temporal correlation techniques

From the general correlation equation, many other correlation techniques have been developed in order to measure different biophysical properties of interest. In the following, we will briefly present some of them.

Spot variation FCS and the diffusion Law

Spot variation FCS consists in acquiring a series of FCS curves acquired with a different PSF waist by in order to probe the dynamics of the environment at different scales; PSF size can be as small as the diffraction limit and increased by varying the size of the laser beam at the back-aperture of the objective. This allows for the construction of a curve of apparent diffusion time as a function of a confinement parameter ($X_c^2 =$

$Area\ of\ the\ focal\ spot/Area\ of\ the\ domain$), that can be analyzed in order to discriminate between several diffusion modalities such as free diffusion, diffusion in a meshwork and diffusion in micro-domains (also referred to as dynamic partition), as shown in ***Figure 40*****Error! Reference source not found.**. For instance, let's assume we're analyzing the system with an area of the focal spot ten times bigger than the area of the domain (or the meshwork cell), yielding a confinement parameter of $X_c^2 = 10$, we will obtain a linear function of $\tau_d^{app}(X_c^2)$. If we extrapolate the curve to its value in $X_c^2 = 0$, we can distinguish the diffusion modality from the value of $\tau_d^{app}(0)$, which will be $\tau_d^{app}(0) = 0$ for free diffusion, $\tau_d^{app}(0) > 0$ for dynamic partition and $\tau_d^{app}(0) < 0$ for diffusion in a meshwork.

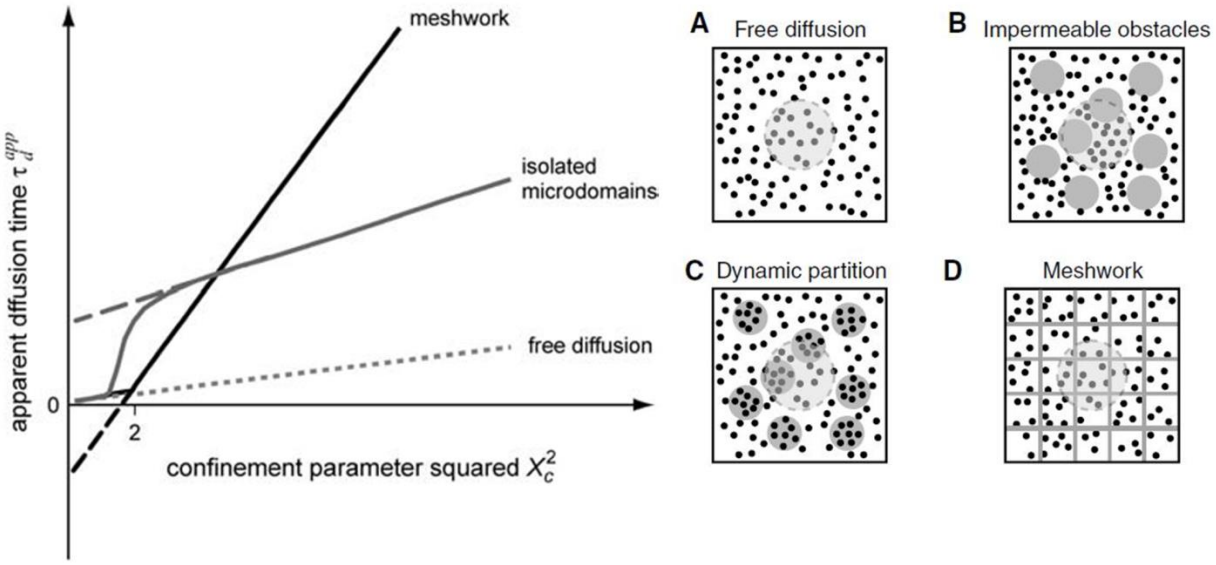

Figure 40: Apparent diffusion time with respect to X_c^2 for different geometries of diffusion, schematized in A-D. Reproduced from (68)

image-derived mean square displacement (iMSD)

image-derived mean square displacement (iMSD) relies on a principle similar to spot-variation FCS, but with a temporal approach. The spatiotemporal cross-correlation function at different time lags is fitted to a Gaussian model, of which the variance as a function of the time lag is considered. The curve obtained is conceptually an average of several MSD curves obtained by single particle tracking techniques, therefore allowing

for the same kind of analysis of the diffusion modality without the need of tracking single particles. An example of iMSD analysis is shown in ***Figure 41***.

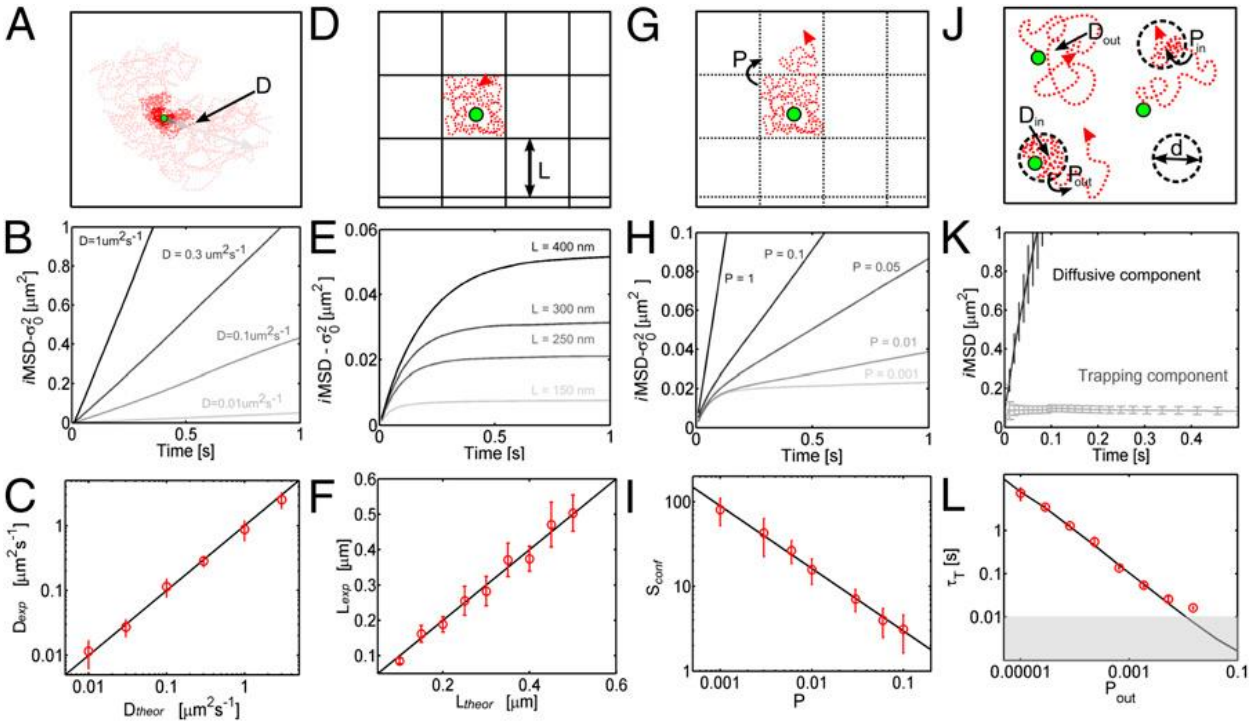

Figure 41: iMSD analysis on simulated 2D diffusion.(A) Simulated condition: 2D isotropic diffusion, with diffusivity D. (B) iMSD is linear, with a higher slope for increasing D values. (C) Accordance between the theoretical D value and that recovered from the analysis. (D) Simulated condition: 2D isotropic diffusion in a meshwork of impenetrable barriers (probability P = 0 to overcome the barrier). (E) iMSD plot starts linear and then reaches a plateau that identifies the confinement area and the corresponding linear size L. (F) Accordance between the theoretical L value and that recovered from the analysis. (G) Simulated condition: 2D isotropic diffusion in a meshwork of penetrable barriers. Particles have probability P > 0 to overcome the barrier, thus generating a hop diffusion component. (H) iMSD plot starts linear (with a slope dependent on D_{micro}) and then deviates toward a lower slope which depends on P. (I) Calculated S_{conf} as a function of the imposed P. (J) Simulated condition: dynamic partitioning. Particles diffuse freely outside and inside the domain with diffusivity D_{out} and D_{in}, respectively, and have probability P_{in} and P_{out} to enter or exit the domain, respectively. (K) Two characteristic iMSD traces in dynamic partitioning: diffusion (black) and trapping (gray). Diffusion shows linear iMSD, whereas trapping yields a constant iMSD. (L) Calculated τ_T as a function of the imposed P_{out} (red dots) with respect to the trapping time directly calculated from molecular trajectories. Reproduced from (69).

iMSD formula can be fitted to a theoretical framework that links the evolution of the variance as a function of the delay time $\sigma^2(\tau)$ to a specific diffusion modality:

$$\sigma^2(\tau) = \sigma_0^2 + 4D_{macro}\tau + \frac{L^2}{3}\left(1 - exp(-\frac{\tau}{\tau_c})\right) \quad \textit{Eq. 44}$$

Here, σ_0^2 is the intercept at τ=0 due to, for instance, the size of the diffusing probe and the PSF, D_{macro} is the macroscopic diffusion coefficient (free diffusion term), L and τ_c are the confinement length of the micro-domain and the confinement time inside the micro-domain, respectively. Furthermore, the directed flow is decoupled from these contribution and can be obtain by quantifying a systematic shift of the spatiotemporal correlation function.

Pair Correlation Function (pCF)

pair correlation function (pCF) relies on the computation of the cross-correlation of two temporally resolved signals recorded simultaneously in two or more spatially separated points in the sample (70). This allows for the determination of obstacles to the diffusion by analyzing the diffusion time, i.e. the average time it takes for the molecules to diffuse from one point to another, in different conditions. The correlation formula used for this technique is:

$$G_{ij}(\tau) = \frac{<\delta I_i(t)\delta I_j(t+\tau)>}{<I_i(t)>_t <I_j(t+\tau)>_{t+\tau}} \quad \textit{Eq. 45}$$

where i and j refer to signals recording in spatially separated regions of the sample. An example of the behavior of this correlation curve is shown in ***Figure 42***.

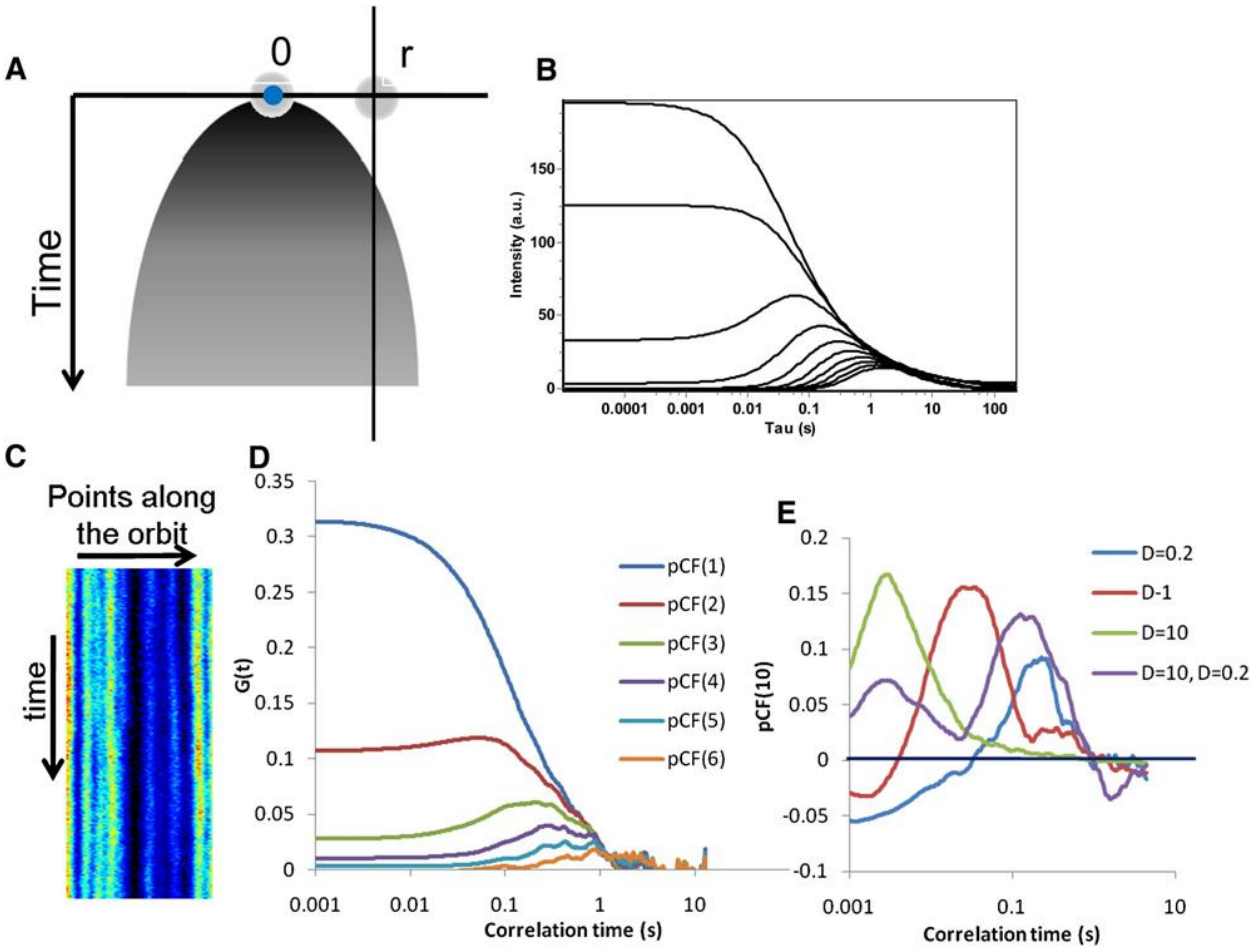

Figure 42: (A) Particle observed at time t= 0 at the origin can be found at a distance r with a probability (shown schematically by the shaded parabolic shape) proportional to the fluorescence intensity at a given distance. (B) The fluorescence intensity is calculated at different distances from 0 to 2 mm in steps of 0.2 mm from the origin along a vertical line with respect to the plot in part A. For this calculation, the waist of the PSF was 0.3 mm and the diffusion coefficient D=1.0 mm^2/s. (C) Intensity carpet for simulation of 500 particles diffusing on a plane with a diffusion coefficient of 0.1 mm^2/s shown in the color-coded image. The warmer colors correspond to higher intensities. (D) PCFs at different pixel distances from 1 to 6. The pCF at a distance of 6 pixels (0.9 mm) falls below zero. (E) pCF calculated at a distance of 10 pixels for different values of the diffusion coefficient. The maximum of the pCF function moves at longer times as the diffusion coefficient decreases. The amplitude of the correlation remains approximately constant. When two molecular species with different diffusion constants are present simultaneously, there are two maxima of the pCF due to the different time delays of the two species in reaching a given distance. At short correlation times, the pCF function can be negative, indicating spatial anti-bunching. Reproduced from (70)

The pCF has been used for the analysis of molecular transport across nuclear pores (71), GFP diffusion related to chromatin compaction (72, 73) and the investigation of nanoparticle transport effects (74). Its theoretical description is discussed in a similar

implementation called dual foci FCS (75), although it fails to show the spatial anti-bunching effect (anti-correlation at short correlation time) shown in ***Figure 42 E***.

2D pCF and the connectivity map

pCF analysis has been coupled to camera detection in order to analyze local anisotropy and connectivity. Camera system can achieve frame times down to fractions of millisecond, generally exhibiting a higher quantum yield with respect to single point detectors. This allows for the efficient, fast and parallel acquisition of several pixels (typically 256x256 up to 2048x2048, depending on the camera and, eventually the pixel binning), the time signal of which can be exploited for computing the pCF of every pixel with, ideally, every other one. For instance, considering a single pixel, we can define a certain distance r_1 and define a certain number N_1 of pixel lying at that distance, radially distributed. For every of the N_1 pixels we can compute an angle-specific pCF curve in order to construct 2D pCF curves (***Figure 43 C,D and F,G***) from which a preferential direction of diffusion can be evaluated, if any.

2D pCF analysis therefore allows for the quantitation (at a specific spatial lag defined by the chosen distance r_1) of the anisotropy in the diffusion of the probe and, by iterating the procedure for all the pixels of the image, the determination of diffusion paths that are followed by the molecules in order to construct the so called *connectivity map*.

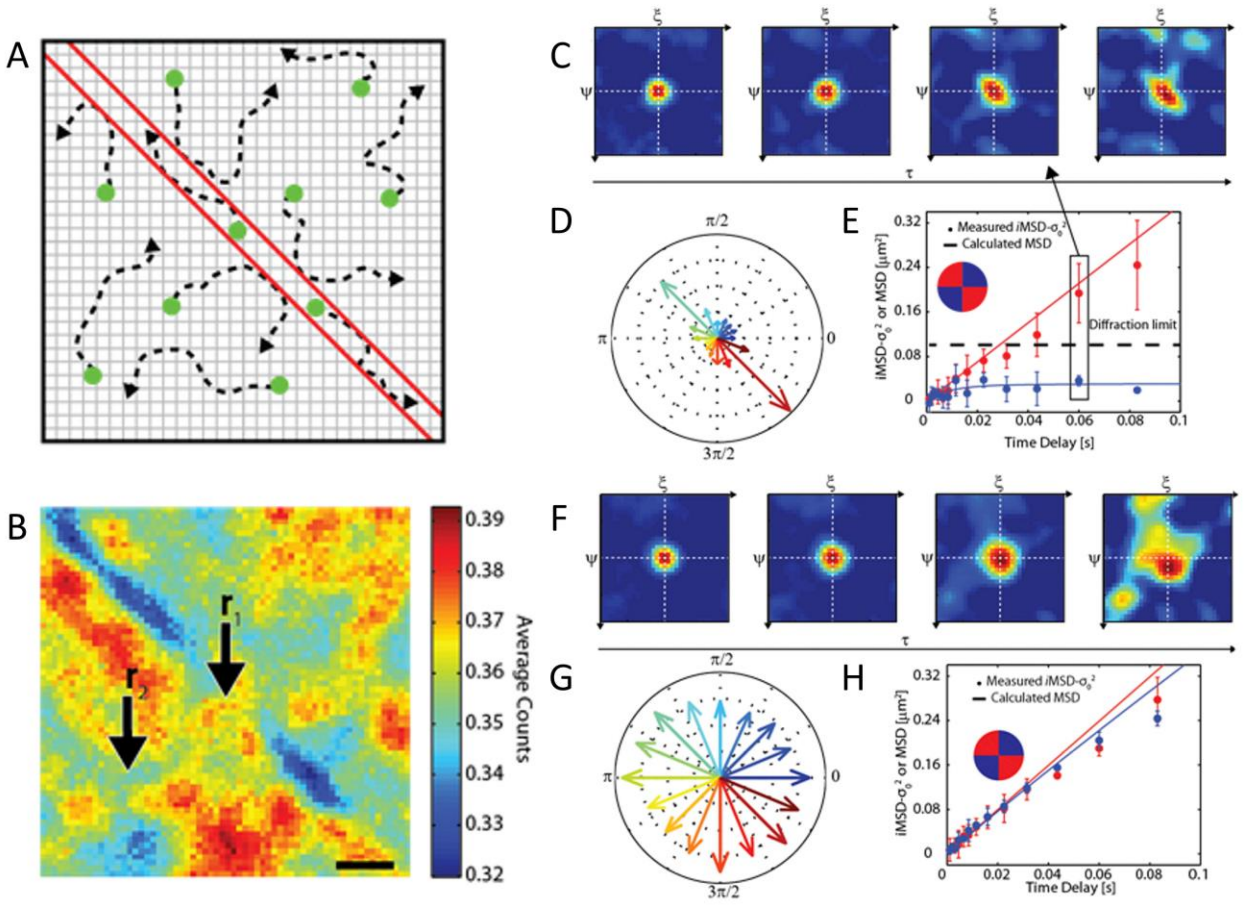

Figure 43: The iMSD tensor reveals the local anisotropy of molecular diffusion. (A) Scheme of the simulated system: molecules can freely diffuse without crossing the two barriers (red lines) that form a channel. (B) Average fluorescence intensity obtained for the simulated experiment. The color scale represents the average counts per pixel per frame. Two representative points, r_1 and r_2, are chosen, the former at the center of the channel and the latter far from the barriers. (C) Time evolution of the 2D pCF associated with r_1: plots shown correspond to τ= 1, 12, 60, and 160 ms. The 2D pCF evolves into a markedly anisotropic shape (i.e., polarized in the direction of the channel). (D) Diffusion-tensor-measured values in the sampled directions. (E) The iMSD(r_1;r,t) at selected t values (solid circles) is compared with its theoretical behavior as calculated from the simulated trajectories (solid lines). Two directions are considered, parallel (red) and perpendicular (blue) to the channel. Below 10 ms, the dynamics in the two directions is similar; above this timescale, the effect of the barriers clearly appears, and the MSD in the direction perpendicular to the barriers saturates. Please note that for two dimensions, the actual MSD coincides with iMSD – σ_0^2. (F) Time evolution of the 2D pCF associated with r_2. The plots shown correspond to τ= 1, 12, 60, and 160 ms. The 2D pCF shows a round-shaped correlation that expands in time, indicating free diffusion. (G) Diffusion tensor values in the sampled directions. (H) iMSD(r_2;r,t) traces in the directions parallel and perpendicular to the barriers are superimposable. Reproduced from (76)

In ***Figure 43*** are shown two examples of directed (***Figure 43 C-E***) and isotropic (***Figure 43 F-H***) diffusion from a simulated sample. By drawing the direction of the motion as a

segment, it is possible to construct a map of the pathways, called *connectivity map*, that the molecules follow when diffusing in the cellular environment.

5.2 Super-resolution Correlation Techniques

In the following, we will consider the coupling of super-resolution methods with the correlation techniques mentioned above.

Spot-variation FCS with SPLIT microscopy

SPLIT (Separation of Photons by LIfetime Tuning) is a STED-based super-resolution technique which exploits the nanosecond fluorescence dynamics in order to selectively decrease the acquisition volume, as shown schematically in ***Figure 44***.

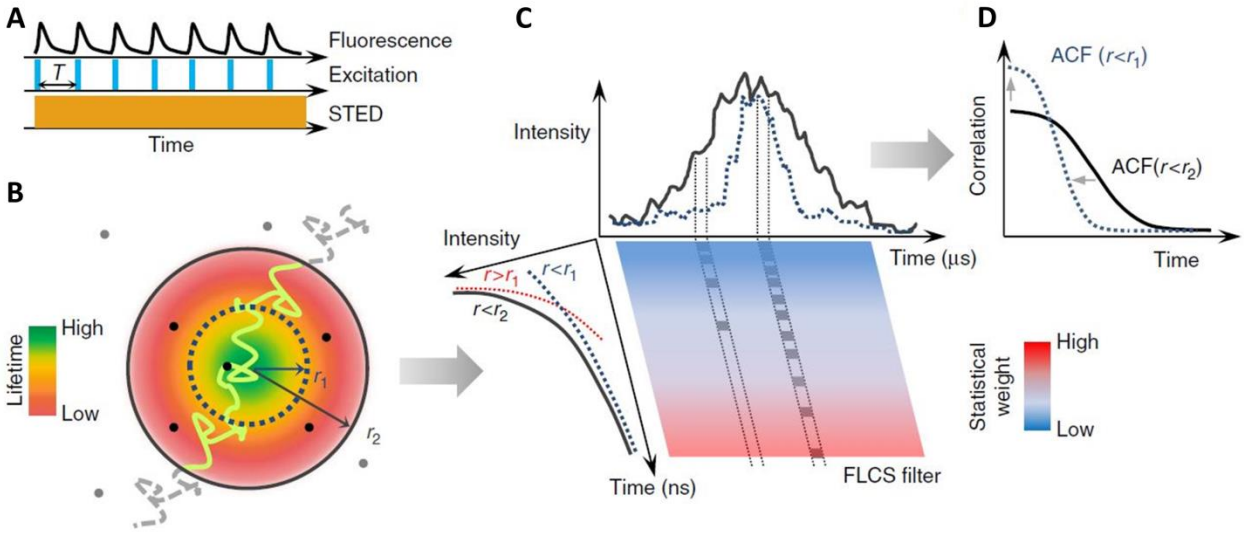

Figure 44: Schematic principle of the SPLIT-FLCS method. A pulsed laser excitation source (A) is coupled with a CW-STED beam to exploit the variations in the fluorescence dynamics observed in the nanosecond time scale (t < T). (B) The spatial variations of fluorescence lifetime within the effective observation volume of the microscope can be modeled as a gradient in the radial direction, with the lifetime value being the highest at the center and decreasing towards the periphery. A molecule transiting within the observation volume will emit photons with different fluorescence lifetime according to the radial position. (C) The temporal fingerprints associated to different spatial positions can be used to weight the photons based on their time of arrival in the nanosecond time scale. For instance, the decay associated to the region defined by radial position $r < r_1$ can be used to generate a statistical filter that, by over-weighting the late-arriving photons, sort out only the intensity emitted from a smaller effective observation volume. (D) Correlation of the weighted photons on the time scale relevant for molecular diffusion ($t > 1\ \mu s >> T$) results in a filtered ACF associated to fluctuations on a smaller effective observation volume, namely an ACF which is narrower and has larger amplitude. Adapted from (56)

Application of the STED beam results in a intensity-dependent reduction of the lifetime of the fluorophores due to the stimulated emission process. Consequently, the center of the STED doughnut will induce less stimulated emission compared to the periphery, allowing us to separate, through a FLCS approach (37), the photons decaying with a longer lifetime (coming from the center) from the ones with a shorter lifetime (coming from the periphery), ultimately decreasing the volume where we collect the photons. A more exhaustive description of the technique can be found in (34, 56). Since this method is based on a photon rejection principle that is applied post-processing, we can obtain multiple acquisition volumes, ranging from about 90 to about 150 nm for intracellular measurements, from the same measurement and implement a spot-variation FCS method using super-resolution volumes instead of sub-diffraction ones from the same dataset, without the need of multiple acquisitions, allowing for the construction of a super-resolved diffusion law. In ***Figure 45 A*** it is possible to appreciate the increase in G(0), when using more and more super-resolved volumes, due to the reduction of the acquisition volume and therefore the reduction of the average number of molecules. These curves are used for the determination of number, diffusion time and diffusion coefficient of EGFP diffusing in the cytoplasm, by fitting to a free diffusion model, that can be shown as a function of the spot area (***Figure 45 B-D***) in order to

construct a spot-variation FCS diffusion law.

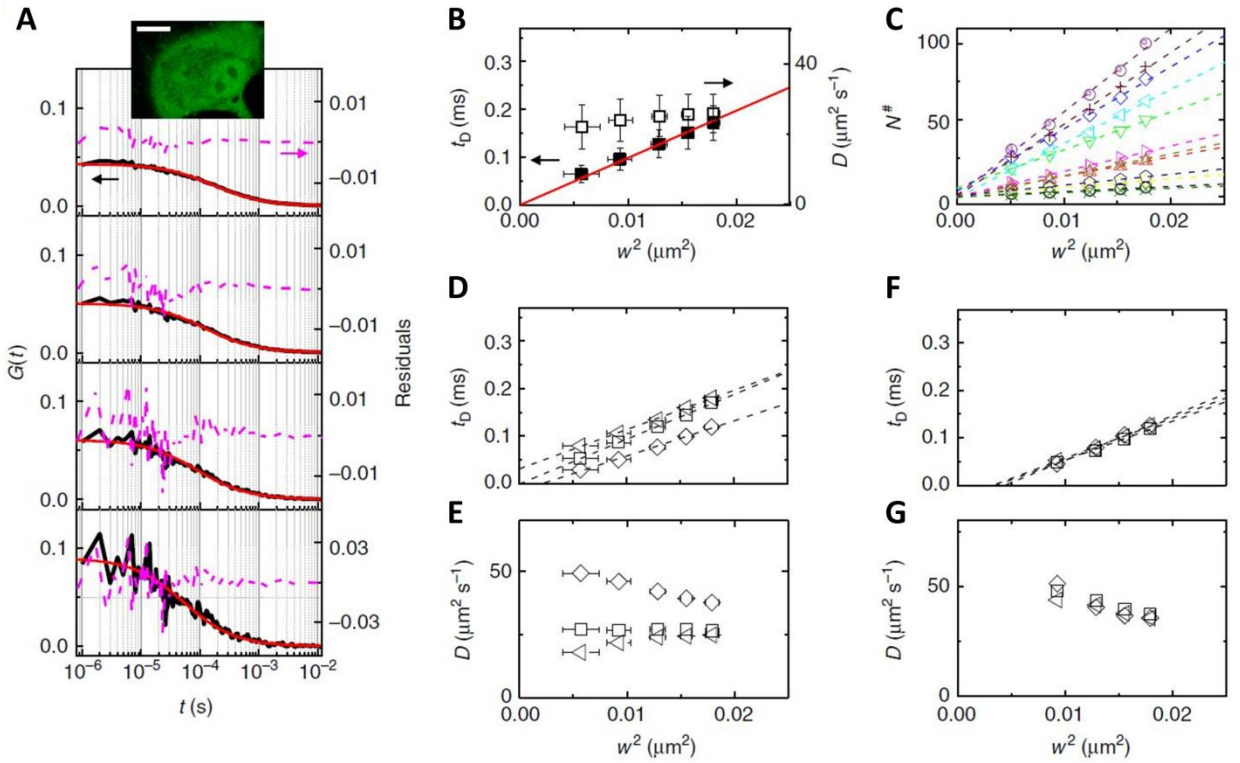

Figure 45: SPLIT-FLCS of EGFP in the cytoplasm of live cells. (A) Representative filtered ACFs of EGFP in the cytoplasm of a HeLa cell at a STED power of 50mW for different values of the parameter r_1. Solid lines are a fit of the data to a free diffusion model. Residuals are shown on the right axis. The image of a cell is shown in the inset (scale bar 10 μm). (B) Transit time t_D (solid squares) and apparent diffusion coefficient D (open squares) for different spatial scales, obtained as the average of single-point measurements in the cytoplasm of n = 12 different HeLa cells (mean ± s.d.). The solid line a linear fit yielding D = 25 $\mu m^2 s^{-1}$. (C) Corrected value of the number of molecules $N^{\#}$ vs. w^2, for all the measured cells, $N^{\#}$ is the average number of molecule corrected with the appropriate shape factor, obtained from the calibration, more details in (56). The dashed lines are linear fits to the data. The slope varies from cell to cell according to differences in EGFP expression level. (D) Transit time t_D and (E) apparent diffusion coefficient D at different spatial scales for three different cells. (F) Transit time t_D and (G) apparent diffusion coefficient D as measured on the very same spot by three short (t_{acq} = 20 s) consecutive acquisitions. Adapted from (56)

AiryScan Comprehensive Correlation Analysis

We coupled super-resolution and correlation techniques through a novel approach by exploiting a micro-camera, namely the Zeiss AiryScan detector array. AiryScan is composed by 32 GaAs detectors arranged in a hexagonal pattern, as shown later on, allowing for a fast acquisition speed (in the order of the micro-seconds) and a camera-

like architecture that allows for the implementation of both camera-based correlation techniques, for instance pCF and connectivity map, and single point techniques, for instance FCS and spot-variation. The latter is implemented in a super-resolved strategy by using variable sub-diffraction volume. Indeed, the PSF is projected on the detector so that the acquisition area corresponds to 1.2 Airy units (corresponding to approximately 1.5 times the resolution limit), consequently the signal coming from every detector corresponds to a 0.2 Airy units linear spatial extension, corresponding to a closed pinhole which, in confocal microscopy, allows for the achievement of super-resolution up to a factor of $\sqrt{2}$ (77).

So far, we tested the AiryScan in single-spot detection without moving the beam, and we implemented several techniques, as shown in ***Figure 46***, where we analyzed a sample of 20 nm beads diffusing in solution.

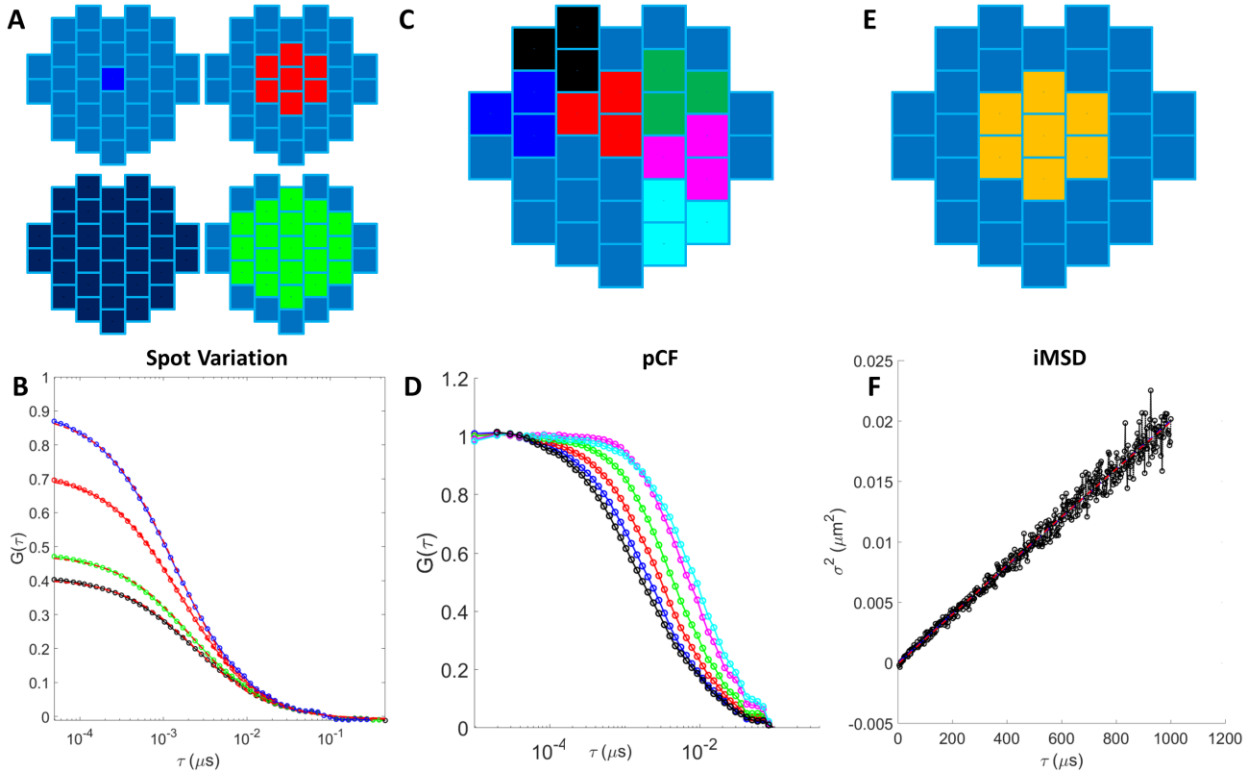

Figure 46: Scheme (A) of the detectors used for constructing the FCS curves in (B), the signals of the colored detectors is summed and then auto-correlated in order to obtain the FCS curve in B of the corresponding color, fitting with a free diffusion model is shown as a red solid line. Scheme (C) of the detectors used for implementing pCF, the signal from detectors of the same color is summed and cross-correlated with the signal coming from the black detectors, obtaining

the pCF curves (D) of the corresponding color. Detectors (E) used for the construction of the iMSD curve in F.

By summing the signal coming from the colored detectors in ***Figure 46 A*** we obtain four FCS curves corresponding to different pinhole sizes ranging from completely close (blue) to completely open (black) and, consequently, to different acquisition volumes, the results of which can be used for constructing a spot-variation FCS curve. pCF implementation was achieved by coupling groups of three detectors (named “volumes” in the following) and cross-correlating their time signal with each other. Their spatial separation allows for the construction of pCF curves (***Figure 46 D***) relative to different distances between the volumes, from which a connectivity map can successively be obtained. Since the computation of the iMSD curve requires the PSF associated to every pixel to have the same shape, iMSD is computed by using only the seven central detectors of the array, since the PSF shape changes when moving away from the optical axis (77). From these pixels we construct a spatiotemporal correlation curve and fit this curve to a Gaussian. Plotting the fitted variance as a function of the temporal lag we obtain the iMSD curve shown in ***Figure 46 F*** by.

After testing and validating the above mentioned techniques with the beads sample, we applied the technique to the study of EGFP diffusion in NIH-3T3 cells. In ***Figure 47*** we show a comparison with a sample of beads diffusing in solution and one acquisition of EGFP in the nucleus.

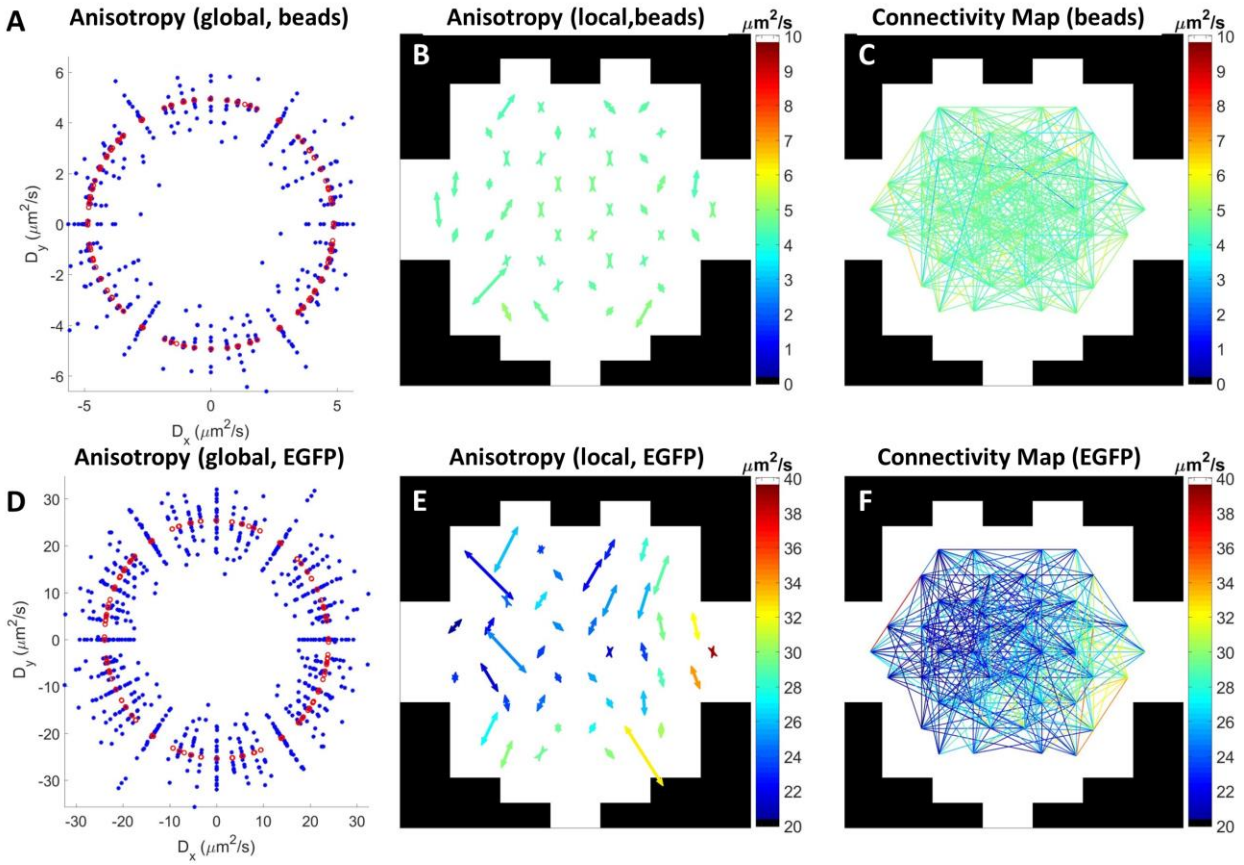

Figure 47: Anisoptropy and connectivity analysis for 20 nm beads (A-C) and EGFP in the nucleus (D-F). Anisotropy (A,D) is displayed as the diffusion coefficient obtained by the pCF curves (blue), along with fitting to an ellipsoid (red), yielding and eccentricity of 1.016 (A) and 1.056 (B). Anisotropy maps (B,E) showing the direction (arrows), the color indicates the average diffusion coefficient computed by pCF fitting in that group of detectors while the length is proportional to the eccentricity. Connectivity maps (C,F), every segment is color-coded with the diffusion coefficient obtained from the fitting of the corresponding pCF function.

The plots in ***Figure 47 A,D*** are created by considering the pCF of each couple of volumes and fitting the pCF to a dual focus FCS model in order to extract a diffusion coefficient relative to every pair of volumes. Every pair of volumes will be oriented at a certain angle, so we computed the x and y projections of the diffusion coefficient that resulted in a single blue circle in the ***Figure 47 A,D*** plot. All the points are used for the fitting of an ellipse (red circles), of which the angle of orientation and the eccentricity are computed for assessing the anisotropy of the system. In ***Figure 47 B,E***, instead, the same analysis is performed considering only one volume against all the other, resulting in a local anisotropy map which is represented as an arrow oriented along the anisotropy direction, with the length proportional to the eccentricity and color-coded as

the average pCF diffusion coefficient of the considered volume. The connectivity maps ***Figure 47 C,F*** simply show the connection as a segment linking two volumes color-coded with the diffusion coefficient obtained from the fitting of the single pCF.

We can appreciate, in contrast with the beads sample (***Figure 47 A-C***) that shows isotropic diffusion and constant connectivity, the presence of anisotropy (***Figure 47 D,E***) and the presence of an area of slower diffusion as showed in the connectivity map (***Figure 47 F***). The analysis of the spot-variation FCS curves and the iMSD curves ***Figure 48*** is consistent and shows that the probe is behaving, at this spatial scale, like a freely diffusing particle. However, the positive intercept in the spot-variation FCS curve suggests that it may be diffusing in micro-domains, possibly corresponding to inaccessible chromatin domains, although further investigation is needed in order to test this hypothesis.

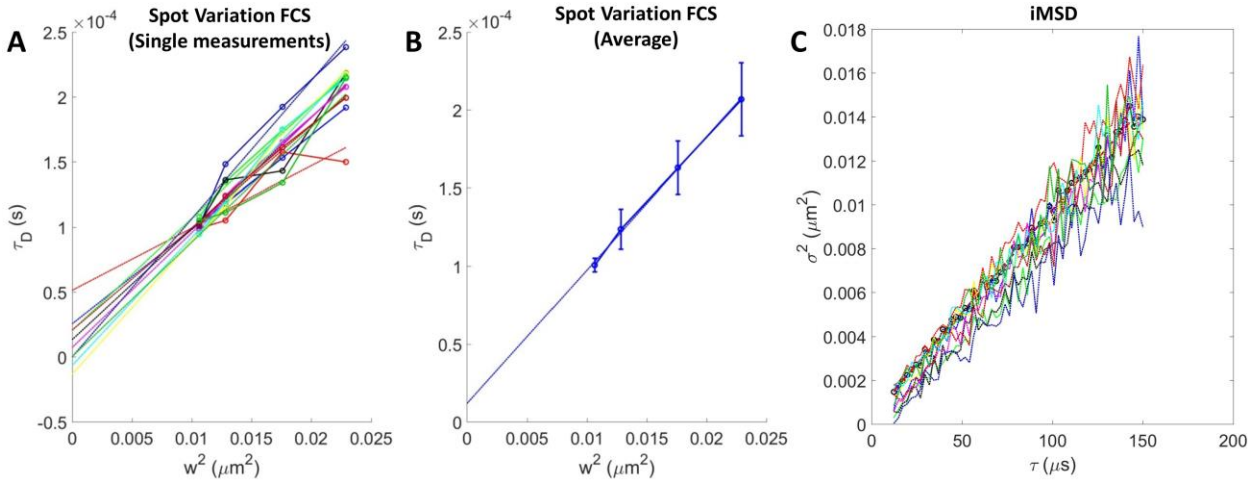

Figure 48: Spot-variation FCS curves (A) of ten different acquisition of EGFP diffusing in the nucleus of NIH-3T3 cells and their average (B, blue solid line, error bars denote the standard deviation) and fitting (B, blue dotted line). iMSD curves of the same ten acquisition (colored dotted lines) and average (black line).

The technique is still being developed but, once completed, it will be able to provide information about diffusion, concentration, environment structure and accessibility, spatiotemporal confinement from a single analysis of a few seconds.

CHAPTER 6 Conclusions and perspectives

The aim of this thesis work was the development of local correlation methods for the analysis of structural and dynamic properties in heterogeneous biological systems.

In this work we introduced the novel concept of PLICS for extending image correlation techniques to heterogeneous systems, a concept based on the generation of local correlation functions and on their analysis by a fast and fit-free approach. Several other techniques stemming from the same PLICS concept were presented and establish an improvement with respect to existing methods. In particular, by extending the PLICS concept to image cross-correlation and RICS, we demonstrated the mapping of local distances between particles (PLICCS) and the mapping of diffusion coefficient (L-RICS), respectively.

All these methods (PLICS, PLICCS, L-RICS) provide an assessment of the spatial heterogeneity in the system. We found that PLICS and PLICCS perform well on images of isolated particles and, despite comparable results could be obtained also by SPT algorithms, these techniques represent a different approach that could be extended (as shown for PLICS) to continuous or higher density samples, to which SPT algorithms could no longer be applied. Notably, there is no such a limitation for the L-RICS, that works also with high densities of particles. The L-RICS method provides a characterization of the spatial heterogeneity of the diffusion properties but, on the other hand, does not provide hints on the diffusion modality and its applicability requires the hypothesis of Brownian diffusion. In this respect, I dedicated the final part of my work to the coupling of super-resolution microscopy techniques (e.g. SPLIT, ISM) with correlation spectroscopy methods. This combination provides access to the diffusion properties at multiple spatiotemporal scales and is suitable for the characterization of diffusion modalities.

Each of the above mentioned techniques can be applied to specific relevant biophysical problems, as summarized in the following.

PLICS represents our first effort to provide a fast analysis of local correlation functions. An improvement with respect to ICS consists in its iterative local approach, which allows

for the detection and segmentation of spatial heterogeneities in size for both isolated and dense samples. Because of its generality, PLICS can in principle be applied to other ICS-based techniques, providing fast local analysis of several biophysical properties. It has been applied to the characterization of endocytic vesicles size in live cells. Following the dynamics of the endocytosis process, we were able to map the size of the vesicles in single cells and to distinguish different maturation states. .

PLICCS is the two colors extension of PLICS and can retrieve and map distances between differently labeled structures. PLICCS provides distance maps and can be implemented in parallel with PLICS for a more extensive analysis of sample properties. Furthermore, its coupling with RDD, our technique for point pattern analysis, makes it possible to evaluate if the relative distribution between the structures of interest is random or structured. We applied this algorithm to quantify the relative distribution of transcription and replication foci in intact nuclei of MCF10A cells. In another application, PLICCS has been used as a localization algorithm, showing high precision and computational speed. Further developments of this technique will include the extension to dense samples.

L-RICS is the application of PLICS to RICS datasets. It represents an improvement with respect to RICS since the latter is limited in the minimum size of the region of analysis, limit that, in L-RICS, has been overcome by the use of the PLICS approach. L-RICS is therefore capable of constructing high-resolution diffusion maps of translational diffusion coefficient even for fast diffusing molecules (e.g. small proteins) by using confocal microscopes equipped with either linear and non-linear scanning systems. We applied L-RICS to the mapping of EGFP diffusion in the nuclear space, specifically at the nucleoplasm-nucleolus interface and in the intra-nucleolar space. Further developments of this technique will include its coupling with super-resolution methods, for instance STED- or ISM-based techniques, in order to provide better insights about complex diffusion behaviors. Such a method would provide high resolution mapping of diffusion modalities and could be applied to the study of GFP diffusion in the nucleus, for instance for probing and mapping chromatin compaction.

SPLIT-FLCS is our first implementation coupling super resolution (provided by the SPLIT technique) with correlation methods. SPLIT-FLCS allows for the determination, from a single dataset, of a diffusion law that can probe the environment the molecules are diffusing in and discriminate between different diffusion modalities. This technique can be further developed by implementing multi-point acquisition, for instance the fast scanning of a line.

Finally, during my period of training abroad, I worked on the development of correlation techniques on a ISM-based super-resolution microscope, the Zeiss AiryScan. In this setup we developed the parallel implementation of several advanced correlation techniques (AiryScan Comprehensive Correlation Analysis)that allow for the simultaneous determination of many biophysical parameters of interest at super-resolution. This analysis is currently being validated and tested on biological samples.

Comparing the above mentioned super-resolution correlation techniques, SPLIT-FLCS is the one that provides the highest resolution (<80 nm of PSF waist using GFP in living cells), while the AiryScan implementation provides similar results at a higher spatial scale (>110 nm of PSF waist in living cells) but is less invasive since it doesn’t require a high intensity depletion laser.

Overall, each of these techniques represents our effort to provide precise, unbiased and fast detection of heterogeneity in complex systems such as, for instance, the cell interior, and we believe to have provided valuable tools to be employed in biological research.

List of publications

- Scipioni L, Gratton E, Diaspro A, Lanzanò L. - ***Phasor Analysis of Local ICS Detects Heterogeneity in Size and Number of Intracellular Vesicles.*** *Biophys J. 2016 Aug 9;111(3):619-29.*

- *Lanzanò L., Scipioni L., Castello M., Bianchini P., Vicidomini G., Diaspro A* ***Role of the Pico-Nano-Second Temporal Dimension in STED Microscopy*** *- Perspectives on Fluorescence Volume 17 of the series Springer Series on Fluorescence pp 311-329: (2016)*

- *Lanzanò L, Scipioni L, Di Bona M, Bianchini P, Bizzarri R, Cardarelli F, Diaspro A and Vicidomini G -* ***Measurement of nanoscale three-dimensional diffusion in the interior of living cells by STED-FCS.*** *Nature Communications 8, Article number:65 (2017)*

- *G. Sancataldo, L. Scipioni, T. Ravasenga, L. Lanzanò, A. Diaspro, A. Barberis, M. Duocastella. -* ***Three-dimensional multiple-particle tracking with nanometric precision over tunable axial ranges.*** *Optica 4 (3), 367-373 (2017)*

- *(in press) L. Scipioni, M. Di Bona, G. Vicidomini, A. Diaspro, L. Lanzanò -* ***Local raster image correlation spectroscopy generates high-resolution intracellular diffusion maps.*** *Communications Biology (2018)*

- *(in preparation) L. Scipioni, et al* ***Spatial organization of nuclear foci in cellular models of cancer by dual color super-resolution microscopy***

Bibliography

1. Moran, U., R. Phillips, and R. Milo. 2010. SnapShot: Key Numbers in Biology. Cell 141:1262-1262.e1261.
2. Shamir, M., Y. Bar-On, R. Phillips, and R. Milo. 2016. SnapShot: Timescales in Cell Biology. Cell 164:1302-1302.e1301.
3. Valeur, B., and M. N. Berberan-Santos. 2012. Front Matter. In Molecular Fluorescence. Wiley-VCH Verlag GmbH & Co. KGaA. I-XXI.
4. Hell, S. W., and J. Wichmann. 1994. Breaking the diffraction resolution limit by stimulated emission: stimulated-emission-depletion fluorescence microscopy. Opt Lett 19:780-782.
5. Vicidomini, G., I. C. Hernandez, M. d'Amora, F. C. Zanacchi, P. Bianchini, and A. Diaspro. 2014. Gated CW-STED microscopy: a versatile tool for biological nanometer scale investigation. Methods 66:124-130.
6. Vicidomini, G., G. Moneron, K. Y. Han, V. Westphal, H. Ta, M. Reuss, J. Engelhardt, C. Eggeling, and S. W. Hell. 2011. Sharper low-power STED nanoscopy by time gating. Nat Methods 8:571-573.
7. Coto Hernández, I., M. Castello, L. Lanzanò, M. D'Amora, P. Bianchini, A. Diaspro, and G. Vicidomini. 2016. Two-Photon Excitation STED Microscopy with Time-Gated Detection. Scientific Reports 6.
8. Sprague, B. L., R. L. Pego, D. A. Stavreva, and J. G. McNally. 2004. Analysis of binding reactions by fluorescence recovery after photobleaching. Biophys J 86:3473-3495.
9. Mueller, F., D. Mazza, T. J. Stasevich, and J. G. McNally. 2010. FRAP and kinetic modeling in the analysis of nuclear protein dynamics: what do we really know? Curr Opin Cell Biol 22:403-411.
10. Rayan, G., J.-E. Guet, N. Taulier, F. Pincet, and W. Urbach. 2010. Recent Applications of Fluorescence Recovery after Photobleaching (FRAP) to Membrane Bio-Macromolecules. Sensors (Basel, Switzerland) 10:5927-5948.
11. Pack, C., K. Saito, M. Tamura, and M. Kinjo. 2006. Microenvironment and effect of energy depletion in the nucleus analyzed by mobility of multiple oligomeric EGFPs. Biophys J 91:3921-3936.
12. Park, H., S. S. Han, Y. Sako, and C. G. Pack. 2015. Dynamic and unique nucleolar microenvironment revealed by fluorescence correlation spectroscopy. FASEB J 29:837-848.
13. Digman, M. A., and E. Gratton. 2011. Lessons in fluctuation correlation spectroscopy. Annu Rev Phys Chem 62:645-668.
14. Elson, Elliot L. 2011. Fluorescence Correlation Spectroscopy: Past, Present, Future. Biophysical Journal 101:2855-2870.
15. Olivier Seksek, J. B., and A.S. Verkman. 1997. Translational Diffusion of Macromolecule-sized Solutes in Cytoplasm

and Nucleus. The Journal of Cell Biology 138.

16. Wachsmuth, M., T. A. Knoch, and K. Rippe. 2016. Dynamic properties of independent chromatin domains measured by correlation spectroscopy in living cells. Epigenetics Chromatin 9:57.
17. Wiseman, P. W. 2015. Image correlation spectroscopy: principles and applications. Cold Spring Harb Protoc 2015:336-348.
18. Petersen, N. O., P. L. Hoddelius, P. W. Wiseman, O. Seger, and K. E. Magnusson. 1993. Quantitation of membrane receptor distributions by image correlation spectroscopy: concept and application. Biophys J 65:1135-1146.
19. Wiseman, P. W., P. Hoddelius, N. O. Petersen, and K. E. Magnusson. 1997. Aggregation of PDGF-beta receptors in human skin fibroblasts: characterization by image correlation spectroscopy (ICS). FEBS Lett 401:43-48.
20. Wiseman, P. W., F. Capani, J. A. Squier, and M. E. Martone. 2002. Counting dendritic spines in brain tissue slices by image correlation spectroscopy analysis. J Microsc 205:177-186.
21. Raub, C. B., J. Unruh, V. Suresh, T. Krasieva, T. Lindmo, E. Gratton, B. J. Tromberg, and S. C. George. 2008. Image correlation spectroscopy of multiphoton images correlates with collagen mechanical properties. Biophys J 94:2361-2373.
22. Robertson, C., K. Ikemura, T. B. Krasieva, and S. C. George. 2013. Multiscale analysis of collagen microstructure with generalized image correlation spectroscopy and the detection of tissue prestress. Biomaterials 34:6127-6132.
23. Tanner, K., D. R. Ferris, L. Lanzano, B. Mandefro, W. W. Mantulin, D. M. Gardiner, E. L. Rugg, and E. Gratton. 2009. Coherent movement of cell layers during wound healing by image correlation spectroscopy. Biophys J 97:2098-2106.
24. Digman, M. A., V. R. Caiolfa, M. Zamai, and E. Gratton. 2008. The phasor approach to fluorescence lifetime imaging analysis. Biophys J 94:L14-16.
25. Barreiro, O., M. Zamai, M. Yanez-Mo, E. Tejera, P. Lopez-Romero, P. N. Monk, E. Gratton, V. R. Caiolfa, and F. Sanchez-Madrid. 2008. Endothelial adhesion receptors are recruited to adherent leukocytes by inclusion in preformed tetraspanin nanoplatforms. J Cell Biol 183:527-542.
26. Dobrinskikh, E., L. Lanzano, J. Rachelson, D. Cranston, R. Moldovan, T. Lei, E. Gratton, and R. B. Doctor. 2013. Shank2 contributes to the apical retention and intracellular redistribution of NaPiIIa in OK cells. Am J Physiol Cell Physiol 304:C561-573.
27. Giral, H., D. Cranston, L. Lanzano, Y. Caldas, E. Sutherland, J. Rachelson, E. Dobrinskikh, E. J. Weinman, R. B. Doctor, E. Gratton, and M. Levi. 2012. NHE3 regulatory factor 1 (NHERF1) modulates intestinal sodium-dependent phosphate transporter (NaPi-2b) expression in apical microvilli. J Biol Chem 287:35047-35056.
28. Giral, H., L. Lanzano, Y. Caldas, J. Blaine, J. W. Verlander, T. Lei, E. Gratton, and M. Levi. 2011. Role of PDZK1 protein in apical membrane expression of renal sodium-coupled phosphate transporters. J Biol Chem 286:15032-15042.
29. Hinde, E., M. A. Digman, C. Welch, K. M. Hahn, and E. Gratton. 2012. Biosensor Forster resonance energy transfer detection by the phasor approach to fluorescence lifetime imaging microscopy. Microsc Res Tech 75:271-281.

30. Cutrale, F., A. Salih, and E. Gratton. 2013. Spectral Phasor approach for fingerprinting of photo-activatable fluorescent proteins Dronpa, Kaede and KikGR. Methods Appl Fluoresc 1:35001.
31. Fereidouni, F., A. N. Bader, and H. C. Gerritsen. 2012. Spectral phasor analysis allows rapid and reliable unmixing of fluorescence microscopy spectral images. Opt Express 20:12729-12741.
32. Fu, D., and X. S. Xie. 2014. Reliable cell segmentation based on spectral phasor analysis of hyperspectral stimulated Raman scattering imaging data. Anal Chem 86:4115-4119.
33. Ranjit, S., L. Lanzano, and E. Gratton. 2014. Mapping diffusion in a living cell via the phasor approach. Biophys J 107:2775-2785.
34. Lanzano, L., I. Coto Hernandez, M. Castello, E. Gratton, A. Diaspro, and G. Vicidomini. 2015. Encoding and decoding spatio-temporal information for super-resolution microscopy. Nat Commun 6:6701.
35. Ma, N., M. A. Digman, L. Malacrida, and E. Gratton. 2016. Measurements of absolute concentrations of NADH in cells using the phasor FLIM method. Biomed Opt Express 7:2441-2452.
36. Digman, M. A., C. M. Brown, P. Sengupta, P. W. Wiseman, A. R. Horwitz, and E. Gratton. 2005. Measuring fast dynamics in solutions and cells with a laser scanning microscope. Biophys J 89:1317-1327.
37. Kapusta, P., M. Wahl, A. Benda, M. Hof, and J. Enderlein. 2007. Fluorescence lifetime correlation spectroscopy. J Fluoresc 17:43-48.
38. Costantino, S., J. W. Comeau, D. L. Kolin, and P. W. Wiseman. 2005. Accuracy and dynamic range of spatial image correlation and cross-correlation spectroscopy. Biophys J 89:1251-1260.
39. Comeau, J. W., S. Costantino, and P. W. Wiseman. 2006. A guide to accurate fluorescence microscopy colocalization measurements. Biophys J 91:4611-4622.
40. Comeau, J. W., D. L. Kolin, and P. W. Wiseman. 2008. Accurate measurements of protein interactions in cells via improved spatial image cross-correlation spectroscopy. Mol Biosyst 4:672-685.
41. Dunn, K. W., M. M. Kamocka, and J. H. McDonald. 2011. A practical guide to evaluating colocalization in biological microscopy. American Journal of Physiology - Cell Physiology 300:C723-C742.
42. Andrey, P., K. Kiêu, C. Kress, G. Lehmann, L. Tirichine, Z. Liu, E. Biot, P.-G. Adenot, C. Hue-Beauvais, N. Houba-Hérin, V. Duranthon, E. Devinoy, N. Beaujean, V. Gaudin, Y. Maurin, and P. Debey. 2010. Statistical Analysis of 3D Images Detects Regular Spatial Distributions of Centromeres and Chromocenters in Animal and Plant Nuclei. PLOS Computational Biology 6:e1000853.
43. Helmrich, A., M. Ballarino, E. Nudler, and L. Tora. 2013. Transcription-replication encounters, consequences and genomic instability. Nat Struct Mol Biol 20:412-418.
44. Dellino, G. I., and P. G. Pelicci. 2014. Next-generation sequencing and DNA replication in human cells: the future has arrived. Future Oncology 10:683-693.

45. Cheezum, M. K., W. F. Walker, and W. H. Guilford. 2001. Quantitative comparison of algorithms for tracking single fluorescent particles. Biophysical Journal 81:2378-2388.
46. Thompson, R. E., D. R. Larson, and W. W. Webb. 2002. Precise Nanometer Localization Analysis for Individual Fluorescent Probes. Biophysical Journal 82:2775-2783.
47. Liu, S., and H. Hua. 2011. Extended depth-of-field microscopic imaging with a variable focus microscope objective. Opt. Express 19:353-362.
48. Sancataldo, G., L. Scipioni, T. Ravasenga, L. Lanzanò, A. Diaspro, A. Barberis, and M. Duocastella. 2017. Three-dimensional multiple-particle tracking with nanometric precision over tunable axial ranges. Optica 4:367.
49. Michalet, X. 2010. Mean Square Displacement Analysis of Single-Particle Trajectories with Localization Error: Brownian Motion in Isotropic Medium. Physical review. E, Statistical, nonlinear, and soft matter physics 82:041914-041914.
50. Dzakpasu, R., and D. Axelrod. Dynamic Light Scattering Microscopy. A Novel Optical Technique to Image Submicroscopic Motions. II: Experimental Applications. Biophysical Journal 87:1288-1297.
51. Brown, C. M., R. B. Dalal, B. Hebert, M. A. Digman, A. R. Horwitz, and E. Gratton. 2008. Raster image correlation spectroscopy (RICS) for measuring fast protein dynamics and concentrations with a commercial laser scanning confocal microscope. Journal of Microscopy 229:78-91.
52. Scipioni, L., E. Gratton, A. Diaspro, and L. Lanzano. 2016. Phasor Analysis of Local ICS Detects Heterogeneity in Size and Number of Intracellular Vesicles. Biophys J 111:619-629.
53. Saffarian, S., and E. L. Elson. 2003. Statistical Analysis of Fluorescence Correlation Spectroscopy: The Standard Deviation and Bias. Biophysical Journal 84:2030-2042.
54. Wohland, T., R. Rigler, and H. Vogel. The Standard Deviation in Fluorescence Correlation Spectroscopy. Biophysical Journal 80:2987-2999.
55. Curcio, A., R. Marotta, A. Riedinger, D. Palumberi, A. Falqui, and T. Pellegrino. 2012. Magnetic pH-responsive nanogels as multifunctional delivery tools for small interfering RNA (siRNA) molecules and iron oxide nanoparticles (IONPs). Chemical Communications 48:2400-2402.
56. Lanzano, L., L. Scipioni, M. Di Bona, P. Bianchini, R. Bizzarri, F. Cardarelli, A. Diaspro, and G. Vicidomini. 2017. Measurement of nanoscale three-dimensional diffusion in the interior of living cells by STED-FCS. Nat Commun 8:65.
57. Sirri, V., S. Urcuqui-Inchima, P. Roussel, and D. Hernandez-Verdun. 2008. Nucleolus: the fascinating nuclear body. Histochem Cell Biol 129:13-31.
58. Johnson, J. M. 1969. A STUDY OF NUCLEOLAR VACUOLES IN CULTURED TOBACCO CELLS USING RADIOAUTOGRAPHY, ACTINOMYCIN D, AND ELECTRON MICROSCOPY. The Journal of Cell Biology 43:197-206.
59. Schmidt, H. B., and R. Rohatgi. 2016. In Vivo Formation of Vacuolated Multi-phase Compartments Lacking Membranes. Cell Rep 16:1228-1236.
60. Eggeling, C., C. Ringemann, R. Medda, G. Schwarzmann, K. Sandhoff, S. Polyakova, V. N. Belov, B. Hein, C. von Middendorff, A. Schonle, and S. W. Hell.

2009. Direct observation of the nanoscale dynamics of membrane lipids in a living cell. Nature 457:1159-1162.
61. Lanzanò, L., I. Coto Hernández, M. Castello, E. Gratton, A. Diaspro, and G. Vicidomini. 2015. Encoding and decoding spatio-temporal information for super-resolution microscopy. Nature Communications 6.
62. Bianchini, P., F. Cardarelli, M. Di Luca, A. Diaspro, and R. Bizzarri. 2014. Nanoscale protein diffusion by STED-based pair correlation analysis. PLoS One 9:e99619.
63. Honigmann, A., V. Mueller, H. Ta, A. Schoenle, E. Sezgin, S. W. Hell, and C. Eggeling. 2014. Scanning STED-FCS reveals spatiotemporal heterogeneity of lipid interaction in the plasma membrane of living cells. Nat Commun 5:5412.
64. Benda, A., Y. Ma, and K. Gaus. 2015. Self-calibrated line-scan STED-FCS to quantify lipid dynamics in model and cell membranes. Biophys J 108:596-609.
65. Vicidomini, G., H. Ta, A. Honigmann, V. Mueller, M. P. Clausen, D. Waithe, S. Galiani, E. Sezgin, A. Diaspro, S. W. Hell, and C. Eggeling. 2015. STED-FLCS: An Advanced Tool to Reveal Spatiotemporal Heterogeneity of Molecular Membrane Dynamics. Nano Lett 15:5912-5918.
66. Hedde, P. N., R. M. Dorlich, R. Blomley, D. Gradl, E. Oppong, A. C. Cato, and G. U. Nienhaus. 2013. Stimulated emission depletion-based raster image correlation spectroscopy reveals biomolecular dynamics in live cells. Nat Commun 4:2093.
67. Clausen, M. P., E. Sezgin, J. Bernardino de la Serna, D. Waithe, B. C. Lagerholm, and C. Eggeling. 2015. A straightforward approach for gated STED-FCS to investigate lipid membrane dynamics. Methods 88:67-75.
68. Wawrezinieck, L., H. Rigneault, D. Marguet, and P. F. Lenne. 2005. Fluorescence correlation spectroscopy diffusion laws to probe the submicron cell membrane organization. Biophys J 89:4029-4042.
69. Di Rienzo, C., E. Gratton, F. Beltram, and F. Cardarelli. 2013. Fast spatiotemporal correlation spectroscopy to determine protein lateral diffusion laws in live cell membranes. Proc Natl Acad Sci U S A 110:12307-12312.
70. Digman, M. A., and E. Gratton. 2009. Imaging barriers to diffusion by pair correlation functions. Biophys J 97:665-673.
71. Cardarelli, F., L. Lanzano, and E. Gratton. 2012. Capturing directed molecular motion in the nuclear pore complex of live cells. Proc Natl Acad Sci U S A 109:9863-9868.
72. Cardarelli, E. H. F. 2011. Measuring the flow of molecules in cells. Biophys Rev 3:119–129.
73. Hinde, E., F. Cardarelli, M. A. Digman, and E. Gratton. 2010. In vivo pair correlation analysis of EGFP intranuclear diffusion reveals DNA-dependent molecular flow. Proceedings of the National Academy of Sciences 107:16560-16565.
74. Hinde, E., K. Thammasiraphop, H. T. Duong, J. Yeow, B. Karagoz, C. Boyer, J. J. Gooding, and K. Gaus. 2017. Pair correlation microscopy reveals the role of nanoparticle shape in intracellular transport and site of drug release. Nat Nanotechnol 12:81-89.

75. Müller, C. B., T. Eckert, A. Loman, J. Enderlein, and W. Richtering. 2009. Dual-focus fluorescence correlation spectroscopy: a robust tool for studying molecular crowding. Soft Matter 5:1358.
76. Di Rienzo, C., F. Cardarelli, M. Di Luca, F. Beltram, and E. Gratton. 2016. Diffusion Tensor Analysis by Two-Dimensional Pair Correlation of Fluorescence Fluctuations in Cells. Biophys J 111:841-851.
77. Sheppard, C. J., S. B. Mehta, and R. Heintzmann. 2013. Superresolution by image scanning microscopy using pixel reassignment. Opt Lett 38:2889-2892.